No d'ordre: 2279

THÈSE

PRÉSENTÉE À

L'UNIVERSITÉ BORDEAUX 1

ÉCOLE DOCTORALE DES SCIENCES PHYSIQUES ET DE L'INGÉNIEUR

Par **Arnaud BERNARD**

Pour obtenir le grade de

DOCTEUR

SPECIALITÉ : MÉCANIQUE

Ondes de plaques guidées : approche temporelle et spatiale

Soutenue le : 13 octobre 2000

Après avis de:

MM.	R.	Chalis, Professeur, Nottingham University (UK),.....	Rapporteurs
	P.P.	Delsanto, Politecnico di Torino (Italie)	

Devant la commission d'examen formée de :

MM.	S.	Baste, Professeur, Université Bordeaux I	Président
	G.	Maze, Professeur, Université Le Havre	Rapporteur
	M.	Lowe, Lecturer, Imperial College University (UK).....	Examinateurs
	M.	Deschamps, Chargé de Recherche CNRS, Université Bordeaux I	
	R.	Chalis, Professeur, Nottingham University (UK)	
	P.P.	Delsanto, Politecnico di Torino (Italie)	

— 2000 —

Ce travail est le résultat d'une collaboration entre le Laboratoire de Mécanique Physique (Université Bordeaux I) et le Laboratoire de Contrôle Non Destructif de Londres (Imperial College of Science, Technology and Medicine).

Je tiens tout particulièrement à remercier Marc Deschamps et Mike Lowe qui se sont démenés afin de mettre cette collaboration en place. En effet, au delà de tout ce que peut apporter une thèse traditionnelle au niveau personnel, ils m'ont permis de découvrir deux cultures complètement différentes, car soyons francs, les "rosbifs" ne travaillent pas comme les "froggies". Je pense sincèrement que c'est une expérience sans précédents pour moi que d'avoir pu en profiter. Sans parler de l'apprentissage de l'anglais qui de nos jours est indispensable et au travers des multiples conférences nationales et internationales, cette thèse m'a aussi permis de trouver un travail sans difficultés et pour cela je les en remercie encore plus.

J'adresse aussi tous mes remerciements au Professeur Peter Cawley que je n'aurais malheureusement jamais pu battre au squash et qui de plus m'a fait l'affront d'arriver une ou deux minutes avant moi au "5k fun run" lors de ma dernière conférence du QNDE en Iowa mais qui a toujours suivi mon travail avec intérêt.

Bien que déclassé sur la place publique de Troussencours par "mon capitaine, oh mon capitaine" lors d'une conférence organisée dans le cadre du GESPA, je tiens tout de même à remercier Monsieur Bernard Poirée tant pour les discussions que j'ai pu avoir avec lui que pour l'amitié qu'il m'a toujours témoigné.

J'adresse tout spécialement mes remerciements à Olivier Poncelet qui depuis ma deuxième année MATMÉCA a toujours été à mes côtés. Au delà de l'amitié qui s'est installée entre nous, je le remercie pour la disponibilité dont il a fait preuve (je comprends vite mais il faut m'expliquer longtemps...) et pour tout ce qu'il a pu m'apprendre tant en acoustique qu'en informatique.

Enfin, je termine par mes compagnons de route dissimulés ça et là entre la France et l'Angleterre. Keith, Paul, Marc, Thomas, Carola, Olivier, Guillaume, merci à vous mes amis qui avez fait le déplacement afin d'être présents pour ma soutenance. Brian, Rob, Dave, Roger, merci pour ces moments passés avec vous. Nicolas, tout en te rappellant que i++ incrémente i de un, je te souhaite bon courage pour la suite. Cependant, si tu n'es pas sûr de toi, peut être pourras-tu demander conseil à notre Lyonnais national que je salue par la même occasion pour ces bons moments passés ensemble.

Ah, j'oubliais, je tiens à préciser aux Coutrionnes (non non, ce n'est pas mal poli), que ce n'est pas parce que le TGV passe par leur village, eh pardon, par leur ville, que cela fait de cette dernière un joyau de la France à ne manquer sous aucun prétexte...

Contents

1 Introduction **9**

2 Transient heterogeneous plane waves **19**

2.1 Plane waves in an infinite viscoelastic medium 19
2.2 Hooke's law 20
2.3 Transient heterogeneous plane waves as a solution of the wave equation 21
2.4 Dispersion equation for a viscoelastic medium 23
2.5 Displacement field 24
2.6 Conclusion 24

3 Comparison between the dispersion curves calculated in complex frequency and the minima of the reflection coefficients for an embedded layer **26**

3.1 Introduction 26
3.2 Theory 28
3.2.1 Response problem 29
3.2.2 Modal problem 32
3.3 Results and discussion 33
3.3.1 Comparison between plane wave reflection coefficients and dispersion curves for real frequency and complex slowness ($\omega = \omega'$) 34
3.3.2 Comparison between plane wave reflection coefficients and dispersion curves for complex frequency and real slowness 37
3.3.3 Consideration of minima of the complex reflection coefficient, assuming complex frequency 38
3.4 Conclusions 41

4 From complex frequency to complex slowness **43**

4.1 Introduction 43
4.2 Fourier theory 45
4.3 Transient Lamb waves 47
4.4 Harmonic leaky guided waves 51
4.5 Transient bounded beam 53
4.6 Conclusion 59

5 Guided waves energy velocity in absorbing and non-absorbing plates **61**
5.1 Introduction 61
5.2 Guided wave problem 62
5.3 Non absorbing plate in vacuum 64
5.3.1 Group velocity 64
5.3.2 Energy velocity 65
5.4 Non absorbing plate in a fluid 67
5.4.1 Energy velocity vectors comparison 68
5.4.2 Energy velocity and group velocity comparison 72
5.5 Absorbing plate in vacuum 74
5.5.1 Theoretical curves 74
5.5.2 Energy velocity vectors comparison 74
5.6 Experiments 77
5.7 Conclusions 80

6 Lamb waves excitation with IDTs **81**
6.1 Plate in vacuum 83
6.2 Plate in water 86
6.3 Conclusion 91

7 Conclusion **93**

8 Bibliography **100**

List of Tables

6.1 Theoretical voltages for each pair of electrodes for both an exponential and a rectangular spatial input. 89
6.2 Maximum amplitudes (arbitrary units) within the Fourier transform spectrum of each received signal at 3.476 MHz. 89
6.3 Corrected voltages for both the rectangular and the exponential profiles in order to excite A_2. 90
6.4 Theoretical and corrected voltages for both the rectangular and the exponential profiles in order to excite S_1. 91

List of Figures

2.1 Complex wavenumber representation of a: a) homogeneous plane wave, b) homogeneous attenuated plane wave, c) evanescent plane wave and d) generalized heterogeneous plane wave at a fixed time. 22
2.2 Transient time signals: a) $\omega'' > 0$, b) $\omega'' < 0$. 23
2.3 Particle displacement field for: a) harmonic heterogeneous plane wave, b) transient heterogeneous plane wave 24

3.1 Comparison between the predicted reflection coefficient zeroes ($\circ$) and dispersion curves ($-$) calculated in real frequency and complex slowness for a 1mm thick Aluminum plate immersed in water. 27
3.2 Plate configuration: layer embedded in a solid medium, showing partial waves. 28
3.3 (a) Comparison between the dispersion curves ($-$) calculated in real frequency and complex slowness [44, 13], the minima ($\circ$) and the zeroes ($\square$) of the shear plane wave reflection coefficient and the minima of the longitudinal plane wave reflection coefficient ($\bullet$) for a 0.1-mm thick layer of Alpha Case embedded in titanium. (b) Attenuation (imaginary wavenumber) of these curves versus frequency. 35
3.4 (a) Comparison of the dispersion curves ($-$) calculated in complex frequency and real slowness, with the reflection coefficient results as shown in Fig.3.3. (b) Attenuation factor $\Omega = \omega''/\omega'$ versus the real part of the frequency for a 0.1-mm thick layer of alpha case embedded in titanium. 36
3.5 Example of poor minima in the titanium/0.1-mm alpha case/titanium structure for the shear plane-wave reflection coefficient at a phase velocity of 8.4km/s. 38
3.6 (a) Comparison between the shear plane-wave reflection coefficient($\cdots$) and the mode labeled *m2* in Fig. 3.4, both calculated in complex frequency and real slowness, (b) Attenuation factor ($\Omega = \omega''/\omega'$) of the zeroes of the reflection coefficient. 39
3.7 As Fig. 3.6 but for the mode *m1*. 40

4.1 Experimental configuration for the resolution in complex frequency and real slowness. 47
4.2 Dispersion curves calculated in complex frequency and real slowness (modes S_0 and A_0) for a 1-mm steel plate embedded in aluminium: (a) Phase velocity (b) Attenuation versus the real part of the frequency. 49

4.3 Predicted plate response to a long duration plane wave signal at a frequency of (a) 3.856 MHz, (b) 2.983 MHz. Part (c) and (d) show the logarithm of the envelopes of the response displayed in part (a) and (b). $\Omega_{simulation}$ refers to $slope/(2\pi * carrier frequency)$ whereas $\Omega_{theoretical}$ refers to the dispersion curves presented in Fig. 4.2. 50
4.4 Experimental configuration for the resolution in complex slowness and real frequency. 51
4.5 Top: dispersion curves calculated in complex slowness and real frequency for a 1-mm steel plate immersed in water. Bottom: response of the plate to a bounded incident beam whose frequency and angle of incidence (or phase velocity) are labelled with a black circle (•) in parts a) and b). 52
4.6 Experimental configuration showing the different positions at which the frequency spectrum is collected. 54
4.7 Dispersion curves-like images showing the modulus of the reflected field at different positions on the receiver plane. Plate is 1-mm thick immersed in water and the incident beam is bounded spatially. 56
4.8 Dispersion curves calculated in real frequency and complex slowness for a 1-mm thick steel plate immersed in water. Top is attenuation ($\omega S_x''$) and bottom is phase velocity ($1/S_x'$) both versus the frequency. To aid comparison, the lines are plotted with thicknesses which is inversely proportional to attenuation. 57
4.9 Dispersion curves calculated in real frequency and complex slowness (dashed lines) and in complex frequency and real slowness (solid lines) for a 1-mm thick anisotropic plate immersed in water. 58
4.10 Reflected field modulus at different positions along the receiver plane for a 1-mm thick highly anisotropic plate immersed in water. Part a) also shows the dispersion curves (solid and dashed lines). 59

5.1 Lamb wave displacement over a time period where y_0 describes the position over the thickness of the plate. 63
5.2 Dispersion curves comparison between a 1 mm thick aluminum plate in vacuum (- - -) and in water (—). Part a) Phase velocity (ω/k_x') and part b) attenuation (k_x'' for the leaky case) both versus the frequency. Black circles show the different positions for the calculation of the energy velocity vectors presented in Fig. 5.3 69
5.3 Local energy velocity vectors comparison between the aluminum plate in vacuum (left) and in water (right) calculated at different y-position for different frequencies labeled • in Fig.5.2. 71
5.4 Local energy velocity vectors for the mode S_1 corresponding to a negative group velocity and to a negative global energy velocity. 72
5.5 (a) Group velocity for S_1, (b) Modulus of the energy velocity flux $\tilde{\mathbf{V}}_\mathbf{e}$ for S_1. 73

5.6 Dispersion curves for a 12.7-mm thick HPPE plate in vacuum [14, 15]. Part a) shows the phase velocity and part b) shows the attenuation both versus the frequency. 75
5.7 Comparison between S_3 dispersion curve (solid line) in HPPE plate and dispersion curves for same plate without material damping (dotted lines). . 76
5.8 Energy velocity vectors comparison between HPPE plate without material damping (left) and with material damping (right) calculated at different **y**-positions. 78
5.9 Comparison between group velocity (solid line), global energy velocity (dotted line (- - -))and experimental measurements (•) for the mode S_3. The attenuation is represented with a dashed line(— - —). 79
5.10 Comparison between the phase velocity (—) and experimental measurements (•) for the mode S_3. 79

6.1 Schematic diagram showing a typical ITD bonded to plate. 83
6.2 Experimental setup for the aluminium plate in vacuum. 84
6.3 Dispersion curves for a 1.6-mm thick aluminium plate in vacuum. Part a) shows phase velocity and part b) shows group velocity, both plotted versus frequency. 84
6.4 Received signals after a propagation of 70 cm along the aluminium plate. Left and right hand side show signals for individual pair, bottom shows the superposition of all those signals as well as the signal obtained when all the fingers are connected. 85
6.5 Experimental setup for the aluminium plate in water. 86
6.6 Dispersion curves for a 1.6-mm thick aluminium plate immersed in water. Part a) shows phase velocity and part b) shows attenuation, both plotted versus frequency. 87
6.7 Comparison between the two dimensional FFT plots and the dispersion curves calculated for a 1.6-mm thick aluminium plate immersed in water. a) all finger pairs are connected, b) all but R, c) all but R and O, d) all but R, O and Y, e) all but R, O, Y and G, f) all but R, O, Y, G and P g) R, O, Y, G, P and B. All those letters being defined in Fig. 6.2 88
6.8 Setup for the measurement of loss in the adhesive. 89
6.9 Energy distribution when the source is rectangular or exponential. 90

Chapter 1

Introduction

Acoustics is a science which nowadays appears in a large number of domains. Really developed in town planning (for all audible noises), it also deals with domains which are much more disparate such as the biomedical domain (imaging processes), solid mechanics (characterisation of material properties), the sorting process on production lines, the military domain (sonar, radar), non destructive testing in general (which can cover a wide range of structures, from hull of a ship to a soldered spot on a printed circuit). It is however obvious that all those applications do not use the same working frequencies since one can go from the hertz (Hz) range in the building domain up to the tera-hertz (10^{12} Hz) range in electronics for example. The frequency range used in this thesis will vary from the Kilo-hertz up to the Mega-hertz.

In the domain presented here, nondestructive testing using ultrasonic methods is a key research area. The techniques are based on the use of acoustic waves that propagate in the material being tested. They normally rely on the analysis of short-duration signals and their interactions with interfaces within the material. The structures are not always accessible in an easy way and are not often transportable (boat hull, suspension bridge cables, aircraft wings) and this has encouraged researchers to study waves called guided waves. These waves can propagate over long distances in the guide (plates, tubes or cylinders in general) and their intrinsic properties allow pertinent controlling techniques. They also offer much faster inspection of large areas because there is no need for testing at every point on the surface of the material. For these reasons, they have been used for the detection of reflections from defects, for the characterization of material properties, to calculate the plane wave reflection coefficient zeroes (a correlation is sometimes assumed), ... They are described by dispersion curves (showing how their velocities vary with frequency) which may of course dramatically change depending on the studied geometry. For example, if a plate is immersed in a fluid, the guided waves can travel within the layer but also in the surrounding medium in the form of outgoing waves, which does not happen if the plate is in vacuum.

The conventional approach when modeling guided waves in an immersed or embedded plate is to assume a steady state condition with real frequency and complex slowness (inverse of the velocity) [42]. This is easy to understand physically. As the waves propagate along the layer, they can leak energy into the embedding material (liquid or solid) in the form of outgoing waves. The amplitudes of the plate waves must then decay as they travel and a complex parameter is needed to describe their spatial attenuation.

Thus the analysis has almost always been done in terms of real frequency and complex wavenumber, which is also equivalent to a real frequency and a complex slowness. The calculation of the dispersion curves for this problem then involves calculating the roots of a function F of the form: $F(\omega, {}^*S)$ where the prefix * denotes a complex quantity.

However, in general, we should also consider the possibility of a complex frequency, allowing, for the direct representation, waves that are transient in time. Thus the completely general form of the wave function should have complex parameters for both frequency and slowness, so that the characteristic equation is of the form $F({}^*\omega, {}^*S)$. This kind of transient approach has already been considered in seismology and identified as an attractive model for calculating the modal properties of the waves excited by an earthquake or explosion point source [72, 60]. In that context the interest was focused on temporal solutions rather than on the space. The complex frequency approach is different from the complex slowness approach and there is no reason to expect that the dispersion curves should be the same.

Very recently, results have been obtained and examined by Poncelet and Deschamps [69, 23, 24] for the propagation of transient heterogeneous waves in a fluid loaded plate using the concept of complex frequency. They showed that, since in practice the excitation signals are bounded both spatially (by the size of the transducers) and temporally (by the switching on and off of the electric source), the use of transient (time attenuation) heterogeneous plane waves (spatial attenuation) seems to allow a more realistic modeling; the complex slowness models the space effects and the complex frequency models the time effects. They argue that it is preferable to represent the spatial properties by the slowness rather than the wavenumber because the slowness is truly independent of the frequency whereas the wavenumber contains a dependence on frequency: ${}^*\mathbf{K} = {}^*\omega {}^*\mathbf{S}$. Their work in this topic has shown that waves which are characterized by amplitudes which decay in time are of key importance when Lamb waves are excited by transient signals in an immersed isotropic or anisotropic plate [69, 68, 23, 24]. One of the findings of their studies of fluid loaded plates is that there is a very good correlation between the dispersion curves calculated in complex frequency and the zeroes of the reflection coefficient which is not evident if the dispersion curves are calculated in real frequency and complex slowness. Their results are quite interesting since there has been much discussion [17, 18, 54, 55] on how the modal properties of a plate, calculated in real frequency and complex slowness, correspond to the reflections of obliquely incident plane waves. Although this correspondence, known as the coincidence angle principle [81], is not verified when the surrounding medium impedance is of the same order than that of the layer, Poncelet and Deschamps found that better

agreement can be found in complex frequency. Their results tend then to suggest that the coincidence angle principle, which postulates that the zeroes of the plane wave reflection coefficients should agree with the dispersion curves, is still valid for fluid loaded plates if the attenuation is described by complex frequency. The modal properties of the plate can then still be linked directly with the zeroes of the reflection coefficient.

Moreover, a fundamental feature of waves is their capability of carrying energy and information over long distances. The velocities which are of interest are the phase velocity, the group velocity and the energy velocity. The phase velocity is the velocity at which the wave fronts or crests travel, the group velocity is the derivative of the frequency wave-number dispersion relation, $V_g = \partial\omega/\partial k_x$ (where ω is the angular frequency, and k_x is the wave-number in the direction of propagation), and the energy velocity is the velocity at which the wave carries its potential and kinetic energy along the structure. Long range testing usually makes use of finite tone bursts or wave packets and optimally exploits waves at frequencies where there is little dispersion, thus the different frequency components within the wave packet propagate at the same velocity and so the wave packet retains its shape as it travels. Naturally we would expect the energy to be transported at the speed of travel of the wave packet, and typically in practice it is true to take this to be equal to the group velocity. This is in fact a most useful property to consider in the context of long range propagation because in such work the focus tends to be on the behaviour of the wave packet rather than the phase information within it, and the wave packet velocity is very readily measured simply by recording the arrival times of the packet.

It is interesting in such applications that the energy appears to propagate at a speed given so simply by the group velocity derivative. However such a relationship does not always hold, a clear example being attenuating waves. If an attenuating harmonic wave is described, as is conventional, by a complex wavenumber and real frequency, then the group velocity calculation yields non-physical solutions such as infinite velocities at some locations on the dispersion curves.

The aim of this work is then firstly to demonstrate that experimental results may agree with theory only if complexity of frequency and slowness, which are appropriate to the setup, are taken into account. The studied geometry being an embedded layer, the results generalize the case of an immersed plate studied by Poncelet in his thesis [68] and confirm the importance of the choice of the experimental setup related to the Lamb wave equation resolution: transient homogeneous plane waves excitation corresponds to one experiment whereas harmonic heterogeneous plane waves excitation corresponds to another. Secondly the Lamb waves energy velocity will be studied in order to compensate for the lack of accuracy of the group velocity definition in some circumstances.

The thesis is divided into the following parts:

Chapter 2 presents the global equations used in this work as well as the general structure of the transient heterogeneous plane waves in order to settle good bases for the next

chapters. The temporal as well as the spatial properties of those waves is clearly distinguished and the notion of the complex slowness bivector $^*\mathbf{S}$ is introduced in order to separate them.

Chapter 3 presents analytical solutions of Lamb wave functions for symmetric and antisymmetric elasto-dynamic modes propagating within a solid layer embedded in an infinite medium. Alternative theoretical analyses of such modes are performed, first in terms of the usual approach of harmonic heterogeneous plane waves (real frequency and complex slowness) and then in terms of transient homogeneous plane waves (complex frequency and real slowness). An example structure of a 0.1-mm thick "Alpha Case" (an oxygen-rich phase of Titanium that is relatively stiff) layer embedded in Titanium is used for the study. A large difference between the usual dispersion curves calculated in real frequency and complex slowness and those calculated in complex frequency and real slowness is shown. Thus the choice between a spatial and a temporal parameter to describe the imaginary part of the guided waves is shown to be significant. The minima and the zeroes of the longitudinal and shear plane wave reflection coefficients are calculated and are compared with the dispersion curves. It is found that they do not match with the dispersion curves for complex slowness, but they do agree quite well with the dispersion curves for complex frequency. This implies that the complex frequency approach is better suited for the comparison of the modal properties with near-field reflection measurements.

The two extreme approaches (harmonic heterogeneous plane waves and transient homogeneous plane waves) having been presented in Chapter 3, Chapter 4 presents the calculation of the response of an isotropic plate, immersed in water or embedded in another solid, to an incident beam which is bounded both spatially and temporally. For several angles of incidence, at a fixed spatial position of the receiver, the frequency spectrum is studied and dispersion curve-like images are built-up. It is shown that depending on whether the receiver is positioned in the specular reflected field or not, the sets of images correspond to the dispersion curves calculated in complex frequency and real slowness or to the dispersion curves calculated in real frequency and complex slowness.

Chapter 5 presents calculations of the energy velocity for lossless Lamb waves, leaky Lamb waves in a plate which is immersed in a fluid, and damped Lamb waves in an absorbing plate in vacuum, using integrals of the energy velocity vector. Analytical studies show that in the case of the lossless waves the velocity calculated in this way agrees exactly with the group velocity. Then numerical studies using the same integral expression show significant differences between the group velocity and the energy velocity in both of the attenuating wave cases. An experimental study of an attenuative mode demonstrates good agreement between the predicted energy velocity and measurements of the velocity of a wave packet at locations on the dispersion curve where the group velocity differs substantially. The energy velocity vectors are also shown in the various model studies, and some interesting phenomena relating to their directions are discussed.

Finally, experimental results using interdigital transducers (finger transducers) which are bonded to a plate are presented in Chapter 6 for an aluminum plate immersed in water. All the fingers being independent (disconnected from the others), the same Lamb mode is excited in two different ways. First, all the fingers receive the same intensity: the source is rectangular in space. Second, the fingers receive an intensity repartition corresponding to the predicted spatial exponential decrease of the mode. It is then shown that the amplitude of the excited mode is greater when the source takes into account the imaginary part of the mode rather than it does not.

L'acoustique est une science qui intervient aujourd'hui dans un très grand nombre de domaines. Très développée en urbanisme (pour tout ce qui concerne les bruits audibles), elle touche aussi des milieux beaucoup plus hétéroclites tels que le milieu biomédical (imagerie en général), la mécanique des solides (caractérisation des propriétés des matériaux), le tri sur des chaînes de production, le domaine militaire (sonar, radar), le contrôle non destructif en général (qui peut aller, en ce qui concerne la taille des structures, d'une coque de pétrolier par exemple jusqu'au point de soudure d'un circuit imprimé). Il est cependant évident que toutes ces applications n'utilisent pas les mêmes fréquences de travail puisque nous pouvons aller du hertz (Hz) dans le domaine du bâtiment jusqu'au tera-hertz (10^{12} Hz) en électronique par exemple. En ce qui concerne cette thèse nous nous placerons dans des bandes de fréquences allant du Kilo-Hertz jusqu'au Méga-Hertz.

Dans le domaine présenté ici, le contrôle non destructif par des méthodes ultrasonores est un des points clé de la recherche en acoustique. Les techniques sont basées sur l'utilisation d'ondes acoustiques qui se propagent dans le matériau en cours de test. Elles reposent en général sur l'analyse de signaux de courtes durées et sur leurs interactions avec les interfaces du matériau. Le fait que les structures ne soient pas toujours accessibles d'une manière évidente ou qu'elles ne soient tout simplement pas transportables (coques de bateaux, cables de suspension de ponts, ailes d'avions) a conduit les chercheurs à étudier des ondes dîtes guidées. Ces ondes pouvant se propager durant de longues distances dans le guide (plaques, tubes ou cylindres le plus souvent), offrent de part leurs propriétées intrinsèques des moyens de contrôle pertinents. Elles permettent de plus d'inspecter de larges surfaces beaucoup plus rapidement puisqu'il n'est pas nécessaire de faire un test sur une multitude d'endroits de la surface du matériau. Pour ces raisons, elles ont été utilisées pour détecter les réflexions sur des défauts, pour la caractérisation des propriétés des matériaux, pour calculer les zéros de coefficients de réflexion en ondes planes (une corrélation est de temps en temps suposée). Elles sont décrites par des courbes de dispersion (montrant comment leur vitesse de phase varie avec la fréquence) qui peuvent changer dramatiquement suivant la structure étudiée. Par exemple, si une plaque est immergée dans un fluide, les ondes guidées peuvent se propager dans la plaque mais aussi dans le milieu environnant sous forme d'ondes dîtes fuyantes, ce qui n'arrive pas si la plaque est dans le vide.

L'approche conventionelle pour la modélisation d'ondes guidées dans des structures immergées ou prises en sandwich dans une autre structure solide est de considérer un état entretenu ou la fréquence est réelle et la lenteur (inverse de la vitesse) est complexe [42]. Ceci est facile à comprendre physiquement. Alors que les ondes se propagent le long de la structure, elles réémettent de l'énergie dans le milieu environnant (liquide ou solide) sous forme d'ondes fuyantes. L'amplitude des ondes de plaques doit donc décroitre pendant la propagation et un paramêtre complexe est alors nécessaire pour décrire leur atténuation spatiale.

Ainsi, l'analyse a presque toujours été faite en termes de fréquence réelle et de nombre d'onde complexe, ce qui revient à considérer une fréquence réelle et une lenteur complexe.

Le calcul des courbes de dispersion pour ce problèmes implique alors le calcul des racines d'une fonction F de la forme : $F(\omega, {}^*S_x)$ où le préfixe * indique que la quantité est complexe.

Cependant, en général, nous devons aussi considérer la possibilité d'une fréquence complexe, permettant, pour la représentation directe, des ondes qui sont transitoires en temps. Ainsi, la forme la plus générale de la fonction d'onde doit avoir des paramètres complexes pour décrire la fréquence et la lenteur, et l'équation caractéristique est donc de la forme $F({}^*\omega, {}^*S_x)$. Ce type d'approche transitoire a déjà été considéré en séismologie et identifié comme un modèle attractif pour le calcul des propriétés des modes excités lors de tremblements de terre ou d'explosions [72, 60]. Dans ce contexte, l'intérêt était porté sur des solutions temporelles plutôt que sur des solutions spatiales. Ainsi l'approche en fréquence complexe est différente de l'approche en fréquence réelle et il n'y a aucune raison de penser que les courbes de dispersion doivent être identiques.

Trés récemment, des résultats ont été obtenus et examinés par Poncelet et Deschamps [69, 23, 24] pour la propagation d'ondes transitoires hétérogènes dans une plaque immergée en utilisant le concept de fréquence complexe. Ils ont montré que, puisque dans la pratique les excitations sont bornées à la fois en temps (par la mise hors ou sous tension de la source électrique) et en espace (par la taille des traducteurs), l'utilisation d'ondes planes transitoires (atténuation en temps) hétérogènes (attenuation en espace) semble permettre une modèlisation plus réaliste; la lenteur complexe modélise les effets spatiaux et la fréquence complexe modélise les effets temporels. Ils soutiennent qu'il est préférable de représenter les propriétés spatiales par la lenteur plutôt que par le nombre d'onde car la lenteur est clairement indépendante de la fréquence alors que le nombre d'onde contient une dépendance fréquentielle : ${}^*\mathbf{K} = {}^*\omega {}^*\mathbf{S}$. Leur travail sur ce sujet a montré que les ondes charactérisées par des amplitudes qui décroissent en temps sont trés importantes lorsque des ondes de Lamb se propageant dans des plaques isotropes ou anisotropes immergées sont excitées par des signaux transitoires [69, 68, 23, 24]. Une des découvertes de leurs études des plaques immergées est qu'il y a une trés bonne corrélation entre les zéros du coefficient de réflexion en ondes planes et les courbes de dispersion calculées en fréquence complexe et en lenteur réelle, ce qui n'est pas évident pour celles calculées en fréquence réelle et en lenteur complexe. Leurs résultats sont trés intéressants puisqu'il y a eu énormement de discussions [17, 18, 54, 55] sur la correspondance des propriétés des modes de plaques, calculées en fréquence réelle et lenteur complexe, et les zéros du coefficient de réflexion. Même si cette correspondance, connue comme étant le principe de coïncidence angulaire [81], n'est pas vérifiée quand l'impédance du milieu environnant est du même ordre que celle de la plaque, Poncelet et Deschamps ont trouvé une meilleure concordance en fréquence complexe. Leurs résultats tendent donc à prouver que le principe de coïncidence angulaire, qui postule que les zéros du coefficient de réflexion en ondes planes doit être en accord avec les courbes de dispersion reste valide si l'atténuation est décrite par une fréquence complexe. Les propriétés des modes de plaques peuvent alors toujours être directement liées avec les zéros du coefficient de réflexion.

De plus une caractéristique fondamentale des ondes est leur pouvoir de transporter de l'énergie ainsi que de l'information durant de longues distances. Les vitesses qui nous intéressent sont la vitesse de phase, la vitesse de groupe et la vitesse de l'énergie. La vitesse de phase est la vitesse à laquelle les fronts d'ondes ou les crêtes de propagent, la vitesse de groupe est la dérivée de la relation de dispersion liant la fréquence au nombre d'onde, $V_g = \partial\omega/\partial k_x$ *(où* ω *est la fréquence angulaire, et* k_x *est le nombre d'onde dans la direction de propagation), et la vitesse de l'énergie est la vitesse à laquelle l'onde transporte son énergie potentielle et cinétique le long de la structure. Les tests sur de grandes distances se font généralement en utilisant des paquets d'ondes et exploitent de manière optimale les ondes à des fréquences où il y a peu de dispersion, ainsi les differentes composantes fréquentielles à l'intérieur du paquet se propagent à la même vitesse et alors le paquet d'ondes garde sa forme durant la propagation. Naturellement, nous pourrions penser que l'énergie est transportée à la même vitesse que celle du paquet d'ondes, et typiquement d'un point de vue pratique cela est juste de la considérer comme égale à la vitesse de groupe. Ceci est en fait une des propriétés des plus utile dans un context de propagation sur de longues distances puisque, dans de tels travaux, l'intérêt est porté sur le comportement du paquet plutôt que sur l'information de la phase qui se trouve à l'intérieur de celui-ci, et la vitesse du paquet est trés rapidement et simplement mesurée en enregistrant son temps d'arrivée.*

Il est intéressant dans de telles applications que l'énergie semble se propager à une vitesse ayant une définition aussi simple que celle de la vitesse de groupe. Cependant, une telle relation n'est pas toujours vraie, un exemple clair étant celui des ondes amorties. Si une onde harmonique atténuée est décrite de manière conventionelle par un nombre d'onde complexe et une fréquence réelle, le calcul de la vitesse de groupe conduit alors à des solutions qui ne sont physiquement pas acceptables comme par exemple à des vitesses infinies sur certaines parties des courbes de dispersion.

Le but de ce travail est tout d'abord de démontrer que des résultats expérimentaux, concernant les modes propres de plaques, ne peuvent être en accord avec la théorie que si la fréquence et la lenteur sont considérées comme des quantités réelles ou complexes, ce choix dépendant bien évidemment de la configuration expérimentale. La géométrie étudiée étant un solide pris en sandwich dans un autre solide, les résultats généralisent le cas de la plaque immergée étudiée par Poncelet dans sa thèse [68] et confirment le choix de la configuration expérimentale par rapport à la résolution de l'équation de dispersion de Lamb : l'excitation d'ondes transitoires homogènes correspond à une configuration expérimentale alors que l'excitation d'ondes inhomogènes harmoniques correspond à une autre configuration. Enfin, la vitesse de l'énergie des ondes de Lamb sera étudiée afin de compenser le manque d'exactitude de la définition de la vitesse de groupe dans certaines circonstances.

La thèse est divisée de la manière suivante :

Le chapitre 2 présente les équations générales utilisées dans ce travail ainsi que la

structure des ondes planes hétérogènes transitoires afin de poser de bonnes bases pour les chapitres suivants. Les propriétés temporelles ainsi que spatiales de ces ondes sont clairement distinguées et la notion de bivecteur lenteur complexe $^*\mathbf{S}$ *est introduit afin de les séparer.*

Le chapitre 3 introduit les solutions analytiques des fonctions symétriques et anti-symétriques des ondes de Lamb se propageant dans un solide pris en sandwich dans un autre solide. Une analyse théorique de tels modes est faite en utilisant l'approche usuelle en considérant des ondes planes harmoniques inhomogènes (fréquence réelle et lenteur complexe) puis en considérant des ondes planes transitoires homogènes (fréquence complexe et lenteur réelle). Un exemple de plaque de 0.1-mm d'épaisseur d'"Alpha Case" (dérivé relativement rigide du Titanium dont la phase est riche en oxygène) pris en sandwich dans du Titanium est utilisé pour cette étude. Une grande différence entre les courbes de dispersion usuelles calculées en fréquence réelle et lenteur complexe et celles calculées en fréquence complexe et lenteur réelle est montrée. Ainsi le choix entre un paramètre spatial ou un paramètre temporel pour décrire la partie imaginaire des ondes guidées s'avère être significatif. Les minima et les zéros du coefficient de réflexion pour une onde plane incidente longitudinale ou transversale sont calculés et comparés avec les courbes de dispersion. Nous montrons alors qu'ils ne correspondent pas aux courbes de dispersion calculées en fréquence réelle et lenteur complexe mais qu'ils sont en très bon accord avec les courbes de dispersion en fréquence complexe. Ceci implique alors que l'approche en fréquence complexe est mieux adaptée pour faire une comparaison des propriétés des modes avec la mesure des coefficients de reflexion en champ proche.

Les deux cas extrèmes (ondes planes harmoniques inhomogènes et ondes planes transitoires homogènes) ayant été présentés au chapitre 3, le chapitre 4 présente le calcul de la réponse d'une plaque isotrope immergée dans de l'eau ou prise en sandwich dans un autre solide insonnée par un champ qui est borné à la fois en espace et en temps. Pour plusieurs angles d'incidence, et pour une position fixe du récepteur, le spectre fréquentiel est étudié et des images à l'allure de courbes de dispersion sont reconstruites. Nous montrons alors qu'en fonction de l'emplacement du récepteur, c'est à dire dans la réflexion spéculaire ou en champ lointain, les images correspondent ou bien aux courbes de dispersion calculées en fréquence complexe et lenteur réelle ou aux courbes de dispersion calculées en fréquence réelle et lenteur complexe.

Le chapitre 5 présente le calcul de la vitesse de l'énergie pour des ondes de Lamb non amorties, pour des ondes de Lamb fuyantes dans une plaque immergée dans l'eau, et pour des ondes de Lamb amorties dans une plaque viscoélastique dans le vide, en utilisant une formulation intégrale du vecteur vitesse de l'énergie. Des études analytiques montrent que, dans le cas où les ondes ne sont pas atténuées, la vitesse calculée de cette manière est exactement égale à la vitesse de groupe. Puis des études numériques utilisant la même formulation intégrale montrent des différences significatives entre la vitesse de groupe et la vitesse de l'énergie pour les deux cas où les ondes sont atténuées. Une étude expérimentale

d'un mode atténué démontre une bonne concordance entre la vitesse de l'énergie théorique et les mesures des vitesses des paquets d'ondes à des endroits sur les courbes de dispersion où la vitesse de groupe diffère substantiellement. Les vecteurs de l'énergie sont aussi étudiés dans les divers modèles et des phénomènes intéressants en ce qui concerne leurs orientations sont présentés.

Finalement, des résultats expérimentaux utilisant des traducteurs interdigitaux (traducteurs peignes) collés à une plaque sont présentés dans le chapitre 6 pour une plaque d'aluminium immergée dans de l'eau. Tous les doigts étant indépendants (déconnectés les uns des autres), le même mode de Lamb est excité de deux manières différentes. Tout d'abord, tous les doigts reçoivent, de la part du générateur, la même énergie : la source est rectangulaire en espace. Enfin, les doigts reçoivent une répartition d'énergie correspondant à la décroissance exponentielle spatiale théorique du mode. Nous montrons alors que l'amplitude du mode excité est plus grande lorsque la source prend en compte la partie imaginaire du mode.

Chapter 2

Transient heterogeneous plane waves

This chapter introduces the structure of the modes that may propagate along the plates studied in the following chapters because guided waves are a superposition of multiple transient heterogeneous plane waves [42]. The description is done for waves that propagate in a viscoelastic isotropic medium, and is also amenable to the simpler isotropic lossless case by setting to zero the viscoelastic constants of the material. The main equations of the linear acoustic theory are presented [29, 74, 1] and the particle displacement field, the polarizations and the dispersion equations of such waves are examined.

2.1 Plane waves in an infinite viscoelastic medium

This work takes place in the linear acoustic domain and the assumption of small perturbations around an equilibrium state is made. The propagation medium is supposed to be infinite in all horizontal directions, unconstrained and follows the classical laws of linear acoustics. By application of Newton's second law, equilibrium requires then:

$$\rho \frac{\partial^2 \mathbf{u}}{\partial t^2} = \nabla \cdot \overline{\overline{\sigma}}, \tag{2.1}$$

where $\mathbf{u} = u(t, \mathbf{M})$ is the displacement fields expressed in Euler variables (t is the time and $\mathbf{M}$ the observation point), ρ is the density of the material, and $\nabla \cdot \overline{\overline{\sigma}}$ is the divergence of the stress tensor of the second order. The strain tensor is defined by:

$$\overline{\overline{\varepsilon}} = \frac{1}{2}(\nabla \mathbf{u} + \nabla^T \mathbf{u}), \tag{2.2}$$

where $\nabla \mathbf{u}$ is the gradient of the displacement field and ∇^T the transposed gradient.

2.2 Hooke's law

If the medium is non viscoelastic, Hooke's law may be written:

$$\overline{\overline{\sigma}} = \lambda\theta\overline{\overline{I}} + 2\mu\overline{\overline{\varepsilon}}, \tag{2.3}$$

where $\theta = \varepsilon_{11} + \varepsilon_{22} + \varepsilon_{33}$ is the change of volume of the element, $\overline{\overline{I}}$ is the identity tensor of the second order and λ and μ are the Lamé elastic stiffness constants related to Young's modulus (E) and Poisson's ratio (ν) by the expressions:

$$\begin{array}{ll} \lambda = \frac{E\nu}{(1+\nu)(1-2\nu)} \; ; & E = \frac{\mu(3\lambda+2\mu)}{(\lambda+\mu)} \\ \mu = \frac{E}{2(1+\nu)} \; ; & \nu = \frac{\lambda}{2(\lambda+\mu)} \end{array} . \tag{2.4}$$

Acoustic vibrations in such media are completely undamped and may propagate without any decrease or attenuation of amplitude. Ideal materials of this kind do not exist in nature, although weakly damped materials are often approximated in this manner, and it is therefore necessary to look for a way of introducing damping into the elastic constitutive relation. Elastic damping may be considered in a number of ways [61] and is usually described by a viscous damping term which depends on the frequency. The chosen model in this work is a Kelvin Voigt viscoelastic description in which a velocity dependent damping force is added to the equation of motion. This model consists of a dashpot representing the damping in parallel with the spring representing the elastic stiffness. The Lamé constants are replaced by the operators:

$$\lambda \; becomes \; \lambda + \lambda'\partial_t \;\; and \;\; \mu \; becomes \; \mu + \mu'\partial_t, \tag{2.5}$$

where the constants λ' and μ' are the viscoelastic material constants, and ∂_t is the partial derivative versus time. The damped model clearly reduces to the elastic model if the viscoelastic constants are zero. It is to be noted that a more appropriated model to plastic structural materials would have been the *Zener*, or *standard linear solid* model, which consists of a (spring) in parallel with (a spring in series with a dashpot). This usually gives a low frequency modulus rising asymptotically to a high frequency modulus, and fits the behaviour of many materials well. However, the Kelvin Voigt model appeared to be enough for our purposes.

Substitution of Hooke's law (Eq. 2.3) and strain-displacement relationship (Eq. 2.2) into the equilibrium equation (Eq. 2.1) leads to the following equation of motion for viscoelastic materials:

$$\rho\frac{\partial^2\mathbf{u}}{\partial t^2} = (\lambda+\mu)\nabla(\nabla\cdot\mathbf{u}) + \mu\nabla^2\mathbf{u} + (\lambda'+\mu')\nabla(\nabla\cdot\frac{\partial\mathbf{u}}{\partial t}) + \mu'\nabla^2\frac{\partial\mathbf{u}}{\partial t} \tag{2.6}$$

where ∇^2 is the operator $(\frac{\partial^2}{\partial x^2}+\frac{\partial^2}{\partial y^2}+\frac{\partial^2}{\partial z^2})$

2.3 Transient heterogeneous plane waves as a solution of the wave equation

The solutions of the wave equation (Eq. 2.6) cannot be directly found and a form of solution must be assumed and checked for suitability. When the material is homogeneous and non viscoelastic (λ' and μ' are set to zero), the simplest solution of the wave equation may be defined as a progressive harmonic homogeneous plane wave. The wavefront is assumed to be an infinite plane normal to the direction of propagation and the amplitude of the wave remains constant over the whole space at any time. The frequency and the wavenumber are real. In those conditions, it is possible to show that this equation has two types of solution. The first describes bulk waves for which the particle displacement is entirely in the direction of propagation. These waves are known as compressional, irrotational, dilatational or longitudinal waves and satisfy:

$$\nabla\wedge\mathbf{u}_L = \mathbf{0}. \tag{2.7}$$

The second type describes bulk waves for which the displacement is normal to the propagation direction. Those waves are known as rotational, shear or transversal waves and satisfy:

$$\nabla\cdot\mathbf{u}_T = 0. \tag{2.8}$$

However, as explained in the introduction, harmonic homogeneous plane waves cannot be used in all problems since they are infinite and uniform in space and in time.

In our problem we expect waves to leak energy into the surrounding medium in the form of outgoing waves so they should attenuate in space (the wavenumber is complex) but they are supposed to attenuate in time as well (the frequency is complex). Those waves have the most general form of plane waves and are known as transient heterogeneous plane waves. They are also solution of Eq. 2.6 and their acoustic field is given by:

$$\mathbf{u}_{L,T} = Re\left\{{}^*\xi_{L,T}{}^*\mathbf{P}e^{i({}^*\omega t-{}^*\mathbf{K.M})}\right\}, \tag{2.9}$$

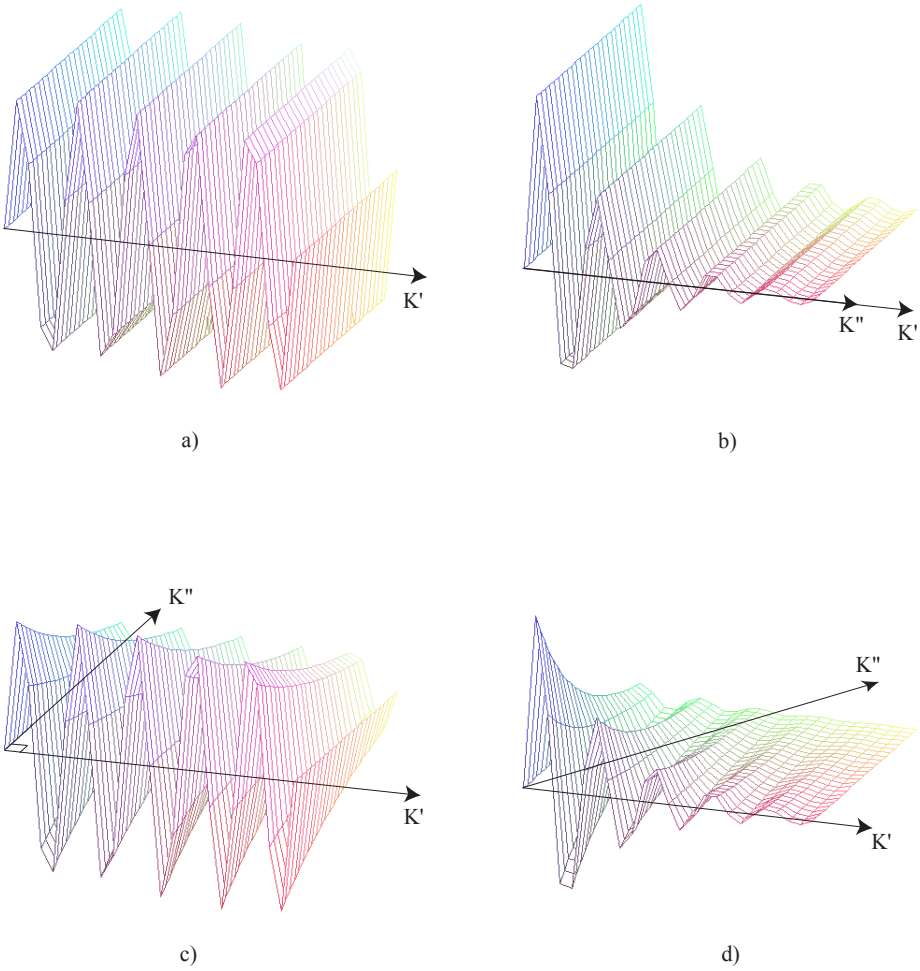

Figure 2.1: Complex wavenumber representation of a: a) homogeneous plane wave, b) homogeneous attenuated plane wave, c) evanescent plane wave and d) generalized heterogeneous plane wave at a fixed time.

where: ${}^*\xi$ is the complex amplitude and ${}^*\mathbf{P} = \mathbf{P}' - i\mathbf{P}''$ represents the unit length polarization vector (${}^*\mathbf{P}.{}^*\mathbf{P} = 1$), ${}^*\mathbf{K} = \mathbf{K}' - i\mathbf{K}''$ stands for the complex wavenumber, ${}^*\omega = \omega' + i\omega'' = 2\pi{}^*f$ is the complex angular frequency with ${}^*f = f' + if''$ the complex frequency, $\mathbf{M}$ is the position vector in space, the notation $Re\{\}$ denotes the real part and the subscript L, T indicates if the wave is longitudinal or transversal respectively.

The real part of the wavenumber $\mathbf{K}'$ is the propagation vector and the imaginary part $\mathbf{K}''$ is the attenuation vector. As shown in Fig. 2.1, if $\mathbf{K}'' = \mathbf{0}$, part a), the wave is purely homogeneous, if $\mathbf{K}''$ is collinear to $\mathbf{K}'$, part b), the wave is homogeneous and attenuated, if $\mathbf{K}''$ is orthogonal to $\mathbf{K}'$, part c), the wave is evanescent and finally part d) shows the generalized transient heterogeneous plane wave at a fixed time. However, as the frequency is considered as a complex quantity, and in order to separate the information due to the space from the information due to the time, as discussed earlier, a more convenient notation

to express the wavenumber is to split it into ${}^*\mathbf{K} = {}^*\omega {}^*\mathbf{S}$ where ${}^*\mathbf{S}$ is the slowness (inverse of the velocity) bivector. In those conditions the real part and the imaginary part of the wavenumber may be rewritten:

$$\begin{cases} \mathbf{K}' = \omega'\mathbf{S}' + \omega''\mathbf{S}'' \\ \mathbf{K}'' = \omega'\mathbf{S}'' - \omega''\mathbf{S}' \end{cases}, \tag{2.10}$$

and therefore, the displacement field defined in Eq. 2.9 becomes:

$$\mathbf{u}_{L,T} = Re\{{}^*\xi_{L,T}{}^*\mathbf{P}e^{i[\omega'(t-\mathbf{S}'.\mathbf{M})-\omega''\mathbf{S}''.\mathbf{M}]}\} \times e^{-\omega''(t-\mathbf{S}'.\mathbf{M})-\omega'\mathbf{S}''.\mathbf{M}}. \tag{2.11}$$

The real positive scalar ω' stands for the angular frequency. The parameter ω'' is the extinction coefficient ($\omega'' > 0$) or the switching-on coefficient ($\omega'' < 0$) of the source. This coefficient describes the time dependence in terms of an exponential transient and is illustrated in Fig. 2.2.

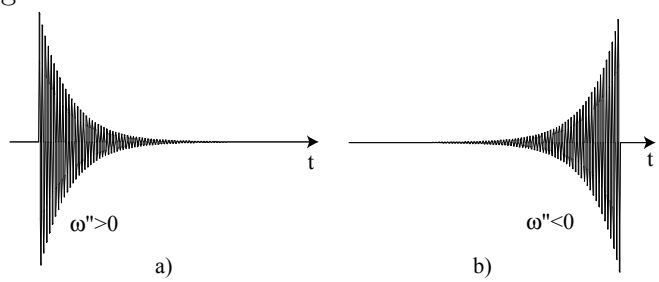

Figure 2.2: Transient time signals: a) $\omega'' > 0$, b) $\omega'' < 0$.

This other notation of course leads to another classification of transient heterogeneous plane waves, well described in Ref. [68], in terms of slowness bivectors and complex frequency instead of wavenumber bivectors and complex frequency where the spatial effects are completely separated from the time effects.

2.4 Dispersion equation for a viscoelastic medium

As explained in the previous section, the wave equation has two types of solutions: longitudinal transient heterogeneous plane waves and shear transient heterogeneous plane waves. The dispersion equations for a viscoelastic medium are obtained by introducing the displacement field of a plane wave (Eq. 2.9) into the wave equation (Eq. 2.6). They actually define a relation between the slowness bivector ${}^*\mathbf{S}$ and the frequency ${}^*\omega$ and may be written:

$${}^*\mathbf{S}_{L,T}.{}^*\mathbf{S}_{L,T} = {}^*\mathbf{S}^2_{L,T} = {}^*\mathbf{C}^{-2}_{L,T} = c^{-2}_{L,T}\left(1 + i\frac{\alpha_{L,T}}{2\pi}\right)^2, \tag{2.12}$$

where the subscript L, T indicates whether the waves are longitudinal or transversal, $c_{L,T}$ is the velocity of the waves and $\alpha_{L,T}$ is the attenuation of the waves expressed in Nepers per wavelength: a wave of unit amplitude will be reduced to $e^{-\alpha_{L,T}} = e^{-2\pi S''_{L,T}/S'_{L,T}}$ after travelling one wavelength.

2.5 Displacement field

The displacement field of transient heterogeneous plane waves described by Eq. 2.9 may be rewritten:

$$\mathbf{u} = \{\mathbf{P}' \sin(\omega' t - \mathbf{K}'.\mathbf{M}) + \mathbf{P}'' \cos(\omega' t - \mathbf{K}'.\mathbf{M})\}\, e^{-(\omega'' t + \mathbf{K}''.\mathbf{M})}. \tag{2.13}$$

If the frequency is real, the particle displacement field over a time period is characterized by an ellipse centered in $\mathbf{M}$ whose major semi-axis is $\mathbf{P}'$ and whose minor semi-axis is $\mathbf{P}''$ as shown in part a) of Fig. 2.3 [67]. However, when the frequency is complex, the particle displacement field is an elliptic spiral (part b) of Fig. 2.3. In the simple case of harmonic homogeneous plane wave ($\mathbf{P}'' = \mathbf{0}$) it would be rectilinear.

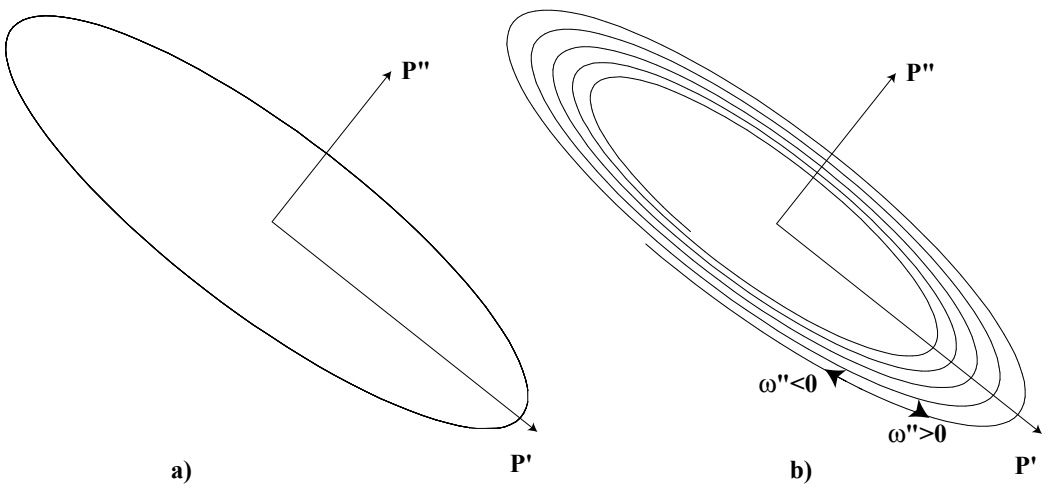

Figure 2.3: Particle displacement field for: a) harmonic heterogeneous plane wave, b) transient heterogeneous plane wave

2.6 Conclusion

Transient heterogeneous plane waves structure has been studied and the different main equations presented. The importance has been emphasized in differentiating the spatial

from the temporal aspects of such waves by using the complex slowness bivector ${}^*\mathbf{S}$ instead of the complex wavenumber bivector ${}^*\mathbf{K}$.

Guided wave properties, as a superposition of several transient heterogeneous plane waves, may be used to determine the modal properties of plates. For fluid loaded plates, the coincidence angle principle, which postulates that an accordance between the plane wave reflection coefficient zeroes and the dispersion curves calculated for harmonic heterogeneous plane waves $(\omega, {}^*\mathbf{S})$ should exist, is widely used in order to find the plate properties. However, this apparently does not hold true when the impedance mismatch between the materials is small. In the next chapter, we study the example of an embedded layer using the notion of complex frequency and the notion of complex slowness and check if better agreement is found with the zeroes of the plane wave reflection coefficients.

Chapter 3

Comparison between the dispersion curves calculated in complex frequency and the minima of the reflection coefficients for an embedded layer

3.1 Introduction

When ultrasonic waves are incident at oblique angles, then ultrasonic techniques can include the generation and detection of guided modes within a layered structure. Within this context, researchers have, for a number of years, studied the properties of guided waves in plates and particularly Lamb waves. The well-known free (lossless) wave propagation modes of an elastic plate in vacuum were first described by Rayleigh and Lamb [36]. Wave interactions and guided waves in the liquid/solid/liquid configuration have already been studied by many authors, for example Chimenti and Nayfeh [17], Chimenti and Rokhlin [18], Nafeh and Chimenti [55, 54], Plona, Behravesh et al. [64], Fiorito and Überall [27], Fiorito, Madigosky et al. [26, 47], Worlton [81], Lenoir, Duclos et al. [37], Izbicki, Maze et al. [33] and Junru and Zhemin [82]. The usual approach, relating the excitation of guided modes to obliquely incident waves, assumes that the zeroes of the plane wave reflection coefficient indicate directly the modal properties of the plate. Then the reflection coefficients for an immersed plate in water are measured using the coincidence angle hypothesis and it is concluded that each zero of the longitudinal plane wave reflection coefficient corresponds to the generation of a plate mode. The dispersion curves for the plate can thus be plotted from measured reflection coefficient minima over ranges of angle and frequency. For many configurations this approach is accurate, for example for most of the modes in an Aluminum plate immersed in water (Fig. 3.1).

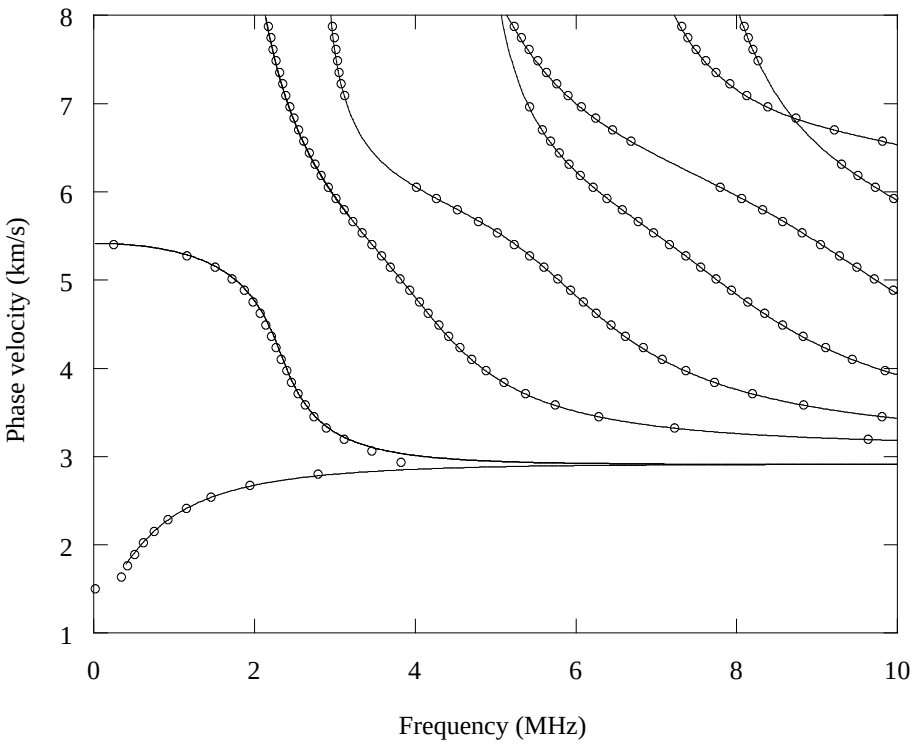

Figure 3.1: Comparison between the predicted reflection coefficient zeroes (∘) and dispersion curves (−) calculated in real frequency and complex slowness for a 1mm thick Aluminum plate immersed in water.

However, it has been shown that the modal properties and the zeroes of the longitudinal plane wave reflection coefficient for a fluid-coupled elastic layer are both modified under fluid loading [17, 18, 55, 54] or solid loading [44, 42, 46, 45, 13] and are not in general coincident. In fact the hypothesis that the minima of the plane wave reflection coefficients correspond to the modal properties of the plate appears to be accurate only when the impedance of the loading material is very much lower than that of the layer.

Multilayered plates such as adhesive joints and diffusion bonded joints are of great interest in nondestructive testing, and Lamb wave properties could potentially be used to detect defects including poor cohesion and poor adhesion, as considered by a number of authors and reviewed by Lowe and Cawley [13]. However, Lowe and Cawley studied such joints and showed that the zeroes of the reflection coefficient when an incident wave in the adherent material reflects from the bond layer do not match the dispersion curves (for the bond layer) calculated in the conventional real frequency and complex slowness [44, 46, 45, 13].

The purpose of this chapter is therefore to investigate a bonded joint example using the alternative complex frequency and real slowness to see whether better agreement is obtained with this choice of solution. The geometry of the structure is similar to that considered by Poncelet and Deschamps except that the plate, which is now the bond layer,

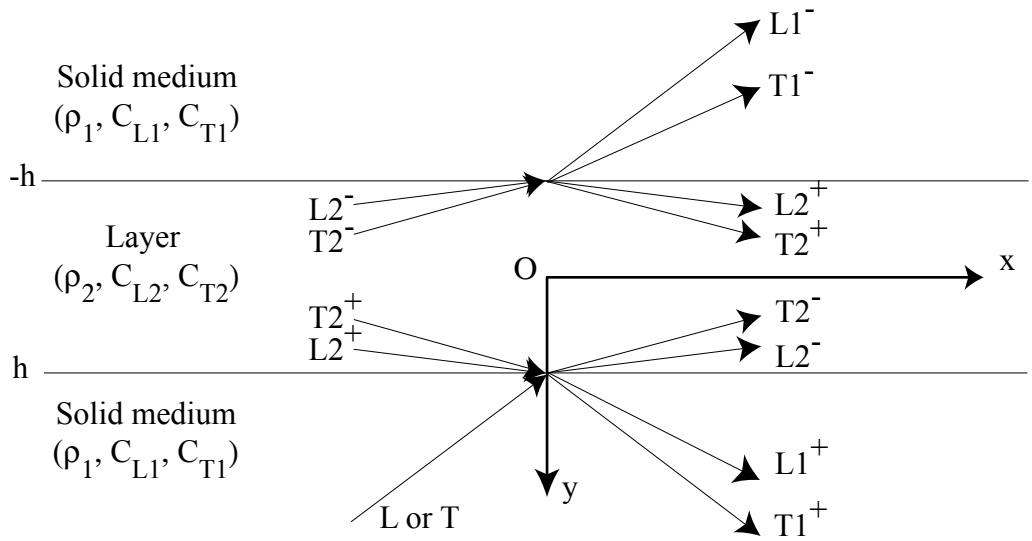

Figure 3.2: Plate configuration: layer embedded in a solid medium, showing partial waves.

is "immersed" in a solid (the adherent material) instead of a fluid. The calculation will be restricted to the two special cases in which the frequency is complex and the slowness is real (the attenuation of the wave is then described in time) and in which the frequency is real and the slowness is complex (the attenuation of the wave is then described in space). In order to simplify, the two materials are supposed to be lossless ($\alpha_{L,T} = 0$ defined in Eq. 2.12 for the two media).

3.2 Theory

The theory for elastic waves in multilayered plates is well established and was for example reviewed by Lowe [42]. Here we state the problem in summary and present specific forms of solution that we have derived for a single loaded layer and which are amenable to analytical study. We adopt the Cartesian coordinate system $\mathbf{X}$(O,x, y, z) and arbitrarily assign $\mathbf{x}$ to the direction of propagation of the guided waves along the plate, $\mathbf{y}$ to the normal to the plate surface and $\mathbf{z}$ to form an orthogonal set, and we consider an infinite plane parallel elastic isotropic plate of thickness 2h, density ρ_2, longitudinal bulk velocity c_{L2} and shear bulk velocity c_{T2}, embedded in an elastic isotropic solid of density ρ_1, longitudinal bulk velocity c_{L1} and shear bulk velocity c_{T1} (Fig. 3.2).

Because the connections between medium 1 and medium 2 are assumed to be ideal, the continuity of the displacements and of the stresses on the two boundaries must be satisfied. The resolution of these limit conditions leads to a system of eight equations with eight unknowns (represented by four partial waves in medium 2 and four outgoing waves in the embedding medium: two in the top half-space and two in the bottom half-space).

At this stage, two different problems can be examined: either the response problem which consists in determining the reflection and the transmission coefficients of waves when a wave is incident, or the modal problem which relates to the guided wave propagation properties of the system in the absence of an incident wave.

It is to be noted that in this chapter all the different quantities being complex, apart from the bulk velocities, the superscript * on the top left hand side will now be omitted for clarity.

3.2.1 Response problem

In this section, the longitudinal plane wave reflection coefficient for an incident longitudinal plane wave and the shear plane wave reflection coefficient for an incident shear plane wave are calculated, the incident wave characteristics being known. The following problem has to be solved:

$$[\mathcal{A}]\{\mathcal{X}\} = \left\{ \begin{array}{c} \mathbf{B}_{L,T} \\ \mathbf{0} \end{array} \right\}, \tag{3.1}$$

where

$$[\mathcal{A}] = \left[\begin{array}{cccccccc} L_1^+ & T_1^+ & -L_2^- & -T_2^- & 0 & 0 & -L_2^+ & -T_2^+ \\ 0 & 0 & -L_2^- & -T_2^- & L_1^- & T_1^- & -L_2^+ & -T_2^+ \end{array} \right], \tag{3.2}$$

$$\{\mathcal{X}\} = \{ \ \xi_{L1}^+ \quad \xi_{T1}^+ \quad \xi_{L2}^- \quad \xi_{T2}^- \quad \xi_{L1}^- \quad \xi_{T1}^- \quad \xi_{L2}^+ \quad \xi_{T2}^+ \ \}^T. \tag{3.3}$$

The first and the second line of Eq. (3.2) represent the boundary conditions on the top and on the bottom interfaces of the embedded layer respectively, the vector $\mathbf{B}_{L,T}$ stands for the longitudinal or shear incident wave and L and T describe the longitudinal and shear partial waves travelling within the embedded layer. The indices on the bottom right-hand side of L or T indicate the medium in which the waves propagate and the sign '+' or '-' on the top right-hand side shows whether the waves travel in the positive or in the negative **y**-direction.

In this kind of problem, the orientation of the shear plane wave polarization vectors is arbitrary. However, in order to simplify, we set the polarization vectors of the partial shear waves within the plate such that their projection on the **x**-axis is positive and on the contrary we fix the polarization vectors of the shear waves outside the plate such that their projection on the **x**-axis is negative. Hence Eq. 3.2 can be expressed in terms of two matrices of dimension 4×4:

$$[\mathcal{A}] = [\mathcal{M}] + [\mathcal{C}] = \begin{bmatrix} M & 0 \\ 0 & M \end{bmatrix} + \begin{bmatrix} 0 & C \\ C & 0 \end{bmatrix}, \tag{3.4}$$

where

$$M = \begin{pmatrix} -S_x\Phi_2 & S_{yT1}\Phi_4 & S_x\Phi_6 & S_{yT2}\Phi_8 \\ -S_{yL1}\Phi_2 & -S_x\Phi_4 & S_{yL2}\Phi_6 & -S_x\Phi_8 \\ \alpha_1\Phi_2 & \beta_1 S_{yT1}\Phi_4 & -\alpha_2\Phi_6 & \beta_2 S_{yT2}\Phi_8 \\ \beta_1 S_{yL1}\Phi_2 & -\alpha_1\Phi_4 & -\beta_2 S_{yL2}\Phi_6 & -\alpha_2\Phi_8 \end{pmatrix}, \tag{3.5}$$

and

$$C = \begin{pmatrix} 0 & 0 & S_x\Phi_5 & S_{yT2}\Phi_7 \\ 0 & 0 & -S_{yL2}\Phi_5 & S_x\Phi_7 \\ 0 & 0 & -\alpha_2\Phi_5 & \beta_2 S_{yT2}\Phi_7 \\ 0 & 0 & \beta_2 S_{yL2}\Phi_5 & \alpha_2\Phi_7 \end{pmatrix}. \tag{3.6}$$

The matrix M refers to each interface and the matrix C represents the coupling between the two interfaces. It is to be noted that without the sign convention concerning the shear polarization M and C would not have been symmetric. The incident wave components (longitudinal or shear) are respectively defined by:

$$\mathbf{B}_L = \Phi_1 \begin{pmatrix} S_x \\ -S_{yL1} \\ -\alpha_1 \\ \beta_1 S_{yL1} \end{pmatrix}, \quad \mathbf{B}_T = \Phi_3 \begin{pmatrix} -S_{yT1} \\ -S_x \\ -\beta_1 S_{yT1} \\ -\alpha_1 \end{pmatrix}, \tag{3.7}$$

and all the variables used in these equations by:

$$\begin{array}{llll} \Phi_1 = e^{imh} & \Phi_5 = e^{iph} & p = \omega S_{yL2} & \\ \Phi_2 = e^{-imh} & \Phi_6 = e^{-iph} & q = \omega S_{yT2} & \alpha_{1,2} = i\rho_{1,2}(1 - 2c_{T1,2}^2 S_x^2) \\ \Phi_3 = e^{inh} & \Phi_7 = e^{iqh} & m = \omega S_{yL1} & \beta_{1,2} = 2i\rho_{1,2}c_{T1,2}^2 S_x \\ \Phi_4 = e^{-inh} & \Phi_8 = e^{-iqh} & n = \omega S_{yT1} & \end{array}, \tag{3.8}$$

where: S_x represents the projection of the slowness bivector on the **x**-axis, S_{yL} and S_{yT} the projection of the longitudinal and shear slowness bivectors on the **y**-axis respectively according to Snell's laws, 1 and 2 indicate medium 1 and 2:

$$S_{yL1,2} = \pm\sqrt{\frac{1}{c_{L1,2}^2} - S_x^2} \; and \; S_{yT1,2} = \pm\sqrt{\frac{1}{c_{T1,2}^2} - S_x^2} \tag{3.9}$$

In the embedded medium, the sign $\pm$ is not really of importance since the waves are trapped between the two interfaces. However, in the embedding medium, it will be chosen in a such way that the wave amplitudes decrease as they travel away from the interfaces.

Because of the properties of the matrices $\mathcal{M}$ and $\mathcal{C}$, a matrix $\mathcal{R}$ is then introduced to simplify the reflection coefficients formulation as follow:

$$[\mathcal{A}] = [\mathcal{M}]([\mathcal{I}] - [\mathcal{R}]), \tag{3.10}$$

where

$$[\mathcal{R}] = -[\mathcal{M}]^{-1}[\mathcal{C}] = \begin{bmatrix} 0 & R \\ R & 0 \end{bmatrix} \quad with \quad R = -M^{-1}C. \tag{3.11}$$

Then, the problem reduces to:

$$\{\mathcal{X}\} = ([\mathcal{I}] - [\mathcal{R}])^{-1}\{\mathbf{S}\}, \tag{3.12}$$

with

$$\{\mathbf{S}\} = \begin{Bmatrix} S_1 \\ 0 \end{Bmatrix}, \quad S_1 = M^{-1}\mathbf{B}_{L,T}, \tag{3.13}$$

and

$$([\mathcal{I}] - [\mathcal{R}])^{-1} = \begin{bmatrix} (I - R^2)^{-1} & 0 \\ 0 & (I - R^2)^{-1} \end{bmatrix} \begin{bmatrix} I & R \\ R & I \end{bmatrix}. \tag{3.14}$$

Finally, using the following relation, the solution of the equation can be immediately obtained by:

$$\begin{pmatrix} \xi_{L1}^{+} \\ \xi_{T1}^{+} \\ \xi_{L2}^{-} \\ \xi_{T2}^{-} \end{pmatrix} = (I - R^2)^{-1}\mathbf{S_1}, \tag{3.15}$$

$$\begin{pmatrix} \xi_{L1}^{-} \\ \xi_{T1}^{-} \\ \xi_{L2}^{+} \\ \xi_{T2}^{+} \end{pmatrix} = (I - R^2)^{-1}R\mathbf{S_1}, \tag{3.16}$$

where I stands for the identity matrix, ξ_{L1}^{+} is the longitudinal plane wave reflection coefficient and ξ_{T1}^{+} the shear plane wave reflection coefficient, the incident wave having a unit amplitude. This method ultimately requires only a division of two determinants of dimension 4x4 and is therefore substantially faster than using a full expansion using Cramers method, which requires solution of two determinants of dimension 8x8.

3.2.2 Modal problem

The modal problem is defined by Fig. 3.2 without any incident wave. Because the geometry is completely symmetric about the **x**-axis in terms of waves and layers, the problem can then be reduced by half. The determinant of dimension 8x8 linked to the matrix $\mathcal{A}$ [Eq. (3.2)], can then be transformed into a multiplication of two determinants of dimension 4x4 by decomposition into symmetric and antisymmetric modes.

3.2.2.1 Equation for symmetric case

For the symmetric modes, the displacements in the plate are given by [1]:

$$\begin{cases} u_x = [-ik_x A_2 \cos(py) + qB_1 \cos(qy)]e^{i\omega(t-S_x x)} \\ u_y = [-pA_2 \sin(py) + ik_x B_1 \sin(qy)]e^{i\omega(t-S_x x)} \end{cases}, \tag{3.17}$$

where: A_2 stands for the amplitude of the longitudinal partial wave and B_1 defines the amplitude of the shear partial wave. The displacements in the bottom half space are given by:

$$\begin{cases} u_x = [k_x C e^{-imy} - nDe^{-iny}]e^{i\omega(t-S_x x)} \\ u_y = [mCe^{-imy} + k_x De^{-iny}]e^{i\omega(t-S_x x)} \end{cases}, \tag{3.18}$$

where: C and D denote the amplitudes of the longitudinal and the shear plane waves, respectively. The displacements in the top half space are the mirror image. Applying the limit conditions on the interface located at $y = h$, that is the continuity of the displacements and of the stresses, a system of 4 equations with 4 unknowns (amplitudes of the waves) is obtained. The trivial solution to this system is to set the amplitudes of the waves to zero: no waves propagate. The other solution is to find the couple $({}^*\omega, {}^*S)$ such that the determinant of the matrix is zero. Thus, after expansion of the determinant, the analytical solution for the symmetric Lamb function (Cs) propagating in a plate embedded in a solid is presented:

$$Cs = A\cot(ph) + B\cot(qh) + C\cot(ph)\cot(qh) + D = 0, \tag{3.19}$$

with

$$\begin{cases} A = 4S_x^6U^2 + S_{yL1}S_{yT1}U^2(\rho_2V + 2S_x^2)^2 + S_x^2(\rho_1 - \rho_2)U[(\rho_1 - \rho_2)V - 4S_x^2] \\ B = S_{yL2}S_{yT2}U^2\{4S_x^2S_{yL1}S_{yT1} + (\rho_1V - 2S_x^2)^2\} \\ C = -i\rho_1\rho_2S_{yT2}S_{yL1} \\ D = i\rho_1\rho_2S_{yL2}S_{yT1} \\ U = \rho_1c_{T1}^2 - \rho_2c_{T2}^2 \\ V = 1/U \end{cases} . \quad (3.20)$$

3.2.2.2 Equation for antisymmetric case

The antisymmetric Lamb function (Ca) propagating in a plate embedded in solid is easily found by changing the cotangents into tangents and by taking the conjugates of C and D. Therefore,

$$Ca = A\tan(ph) + B\tan(qh) - C\tan(ph)\tan(qh) - D = 0. \quad (3.21)$$

3.2.2.3 Solution

The dispersion curves are the loci of solutions ($^*\omega$, $^*S_x$) of the transcendental equation $Cs = 0$ or $Ca = 0$. Those curves theoretically link the variables $^*\omega$ and $^*S_x$ and then should be traced in a four dimensional space. However, as some quantities will be fixed the dispersion curves are represented by two coupled plots, the first showing the real part of the slowness versus the real part of the frequency and the second showing the imaginary part of one of the two variables versus the real part of the frequency. The dispersion curves in complex frequency and real slowness are calculated with a Newton-Raphson algorithm providing fast computation. The dispersion curves calculated using the conventional assumption of real frequency and complex slowness are calculated using a general purpose model developed by Lowe [42] and Pavlakovic, Lowe, *et al.* [59].

3.3 Results and discussion

The example that has been chosen for study relates to diffusion bonded Titanium. Previous work by Lowe and Cawley [44, 13] examined the reflection coefficient minima and the real frequency dispersion curves for an idealized defective bonded joint, and those results form a useful basis for comparison with the dispersion curves for complex frequency. The idealized defective joint consists of a uniform layer of Alpha Case (or Hard Alpha) at the bondline between the two Titanium adherents. The Alpha Case is brittle and may be

established if oxygen or nitrogen is present during bonding. It has been shown that the bulk velocities of the Alpha Case are about 5% to 10% faster than those of the Titanium but that its density is roughly the same [75, 43]. The properties of those materials have therefore been chosen to be, for Titanium, $c_{L1} = 6.06\ m/ms$, $c_{T1} = 3.23\ m/ms$, $\rho_1 = 4.46\ g/cm^3$ and for Alpha Case $c_{L2} = 6.66\ m/ms$, $c_{T2} = 3.553\ m/ms$, $\rho_2 = 4.46\ g/cm^3$. In this section, the dispersion curves calculated either in real frequency and complex slowness or in complex frequency and real slowness will be compared to the minima and the zeroes of the shear and longitudinal plane wave reflection coefficients.

3.3.1 Comparison between plane wave reflection coefficients and dispersion curves for real frequency and complex slowness ($\omega = \omega'$)

Predictions of the reflection coefficient results and the conventional complex slowness dispersion curves for the layer of Alpha Case embedded in Titanium are shown in Fig. 3.3. Part (a) of the figure shows the phase velocity ($1/S_x^{'}$) and part (b) presents the attenuation factor $K_x'' = \omega S_x''$ expressed in Nepers per millimeters (a wave of unit amplitude will be reduced to $e^{-K_x''} = e^{-\omega S_x''}$ after travelling one unit length), both versus the frequency [44, 46, 45, 13]. Two categories of reflection coefficient results are shown on part (a): "zeroes" (□) correspond to the identification of zero values of the reflection coefficient; "minima" (○) correspond to the identification of locations where there is a clear dip of the function but not to zero value. Empty symbols (□, ○) correspond to the shear plane wave reflection coefficient (shear incident, shear reflected), filled symbols (●) correspond to the longitudinal plane wave reflection coefficient. The horizontal dashed lines show the bulk velocities of the two materials. It should be noted that due to their very high attenuation leading to non-physical solutions some modes have not been traced or pursued.

It can be seen that there is no region, in this frequency range, where the minima or the zeroes of the reflection coefficients coincide with the dispersion curves, although they show some similar trends and the leaky shear modes and the zeroes seem to correlate reasonably well near the shear bulk velocity of the Titanium as the frequency increases. The convergence of the zeroes towards the modes at high frequency is also accompanied by a reduction in attenuation [Fig. 3.3(b)] and led Lowe and Cawley to suggest that the separation of zeroes and modes is related to the rate of leakage. It is clear therefore that the measurement of zeroes of the reflection coefficient do not reveal the (conventional) harmonic heterogeneous modal properties.

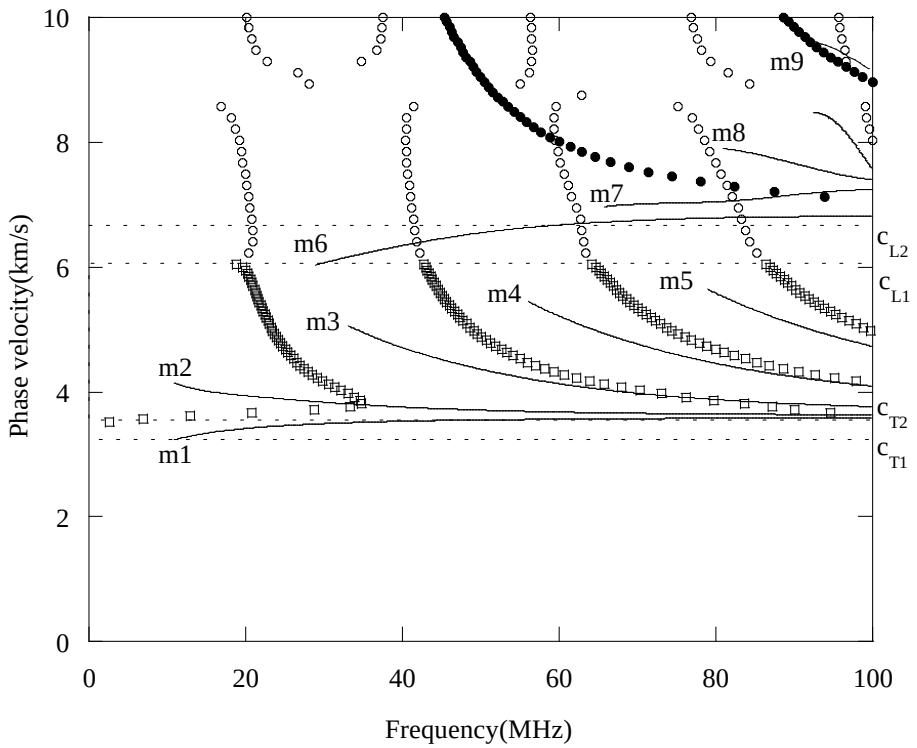

(a)

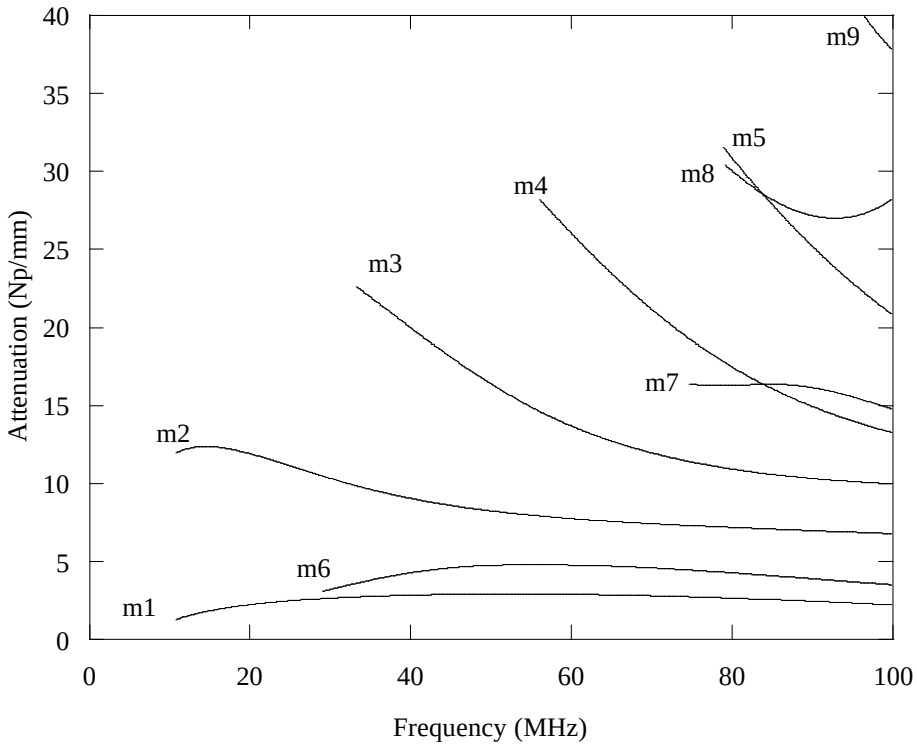

(b)

Figure 3.3: (a) Comparison between the dispersion curves (−) calculated in real frequency and complex slowness [44, 13], the minima (○) and the zeroes (□) of the shear plane wave reflection coefficient and the minima of the longitudinal plane wave reflection coefficient (●) for a 0.1-mm thick layer of Alpha Case embedded in titanium. (b) Attenuation (imaginary wavenumber) of these curves versus frequency.

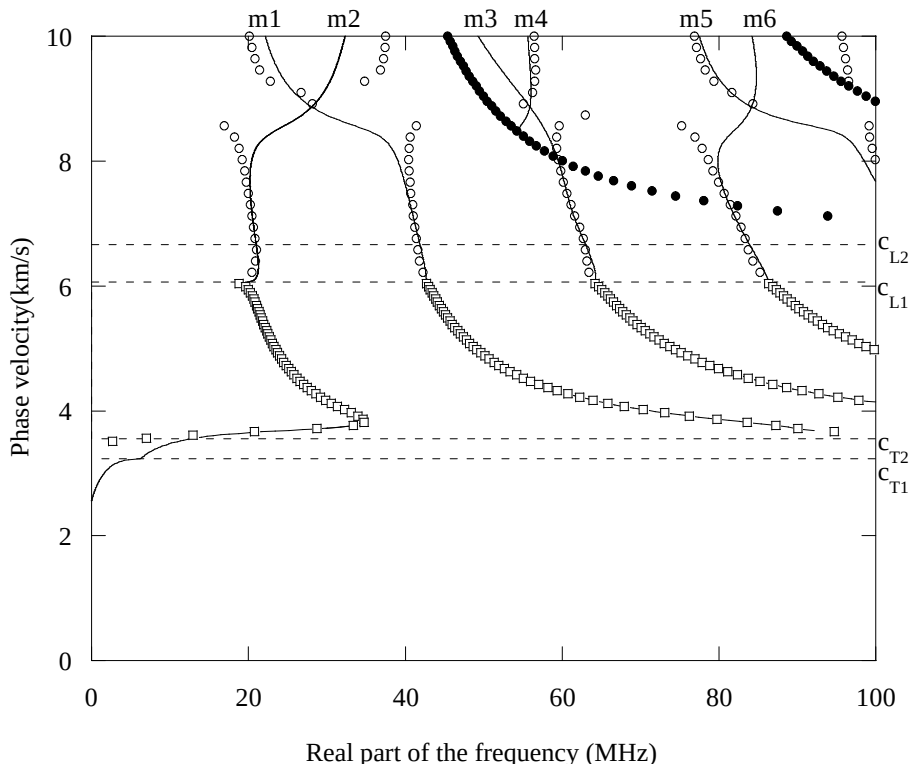

(a)

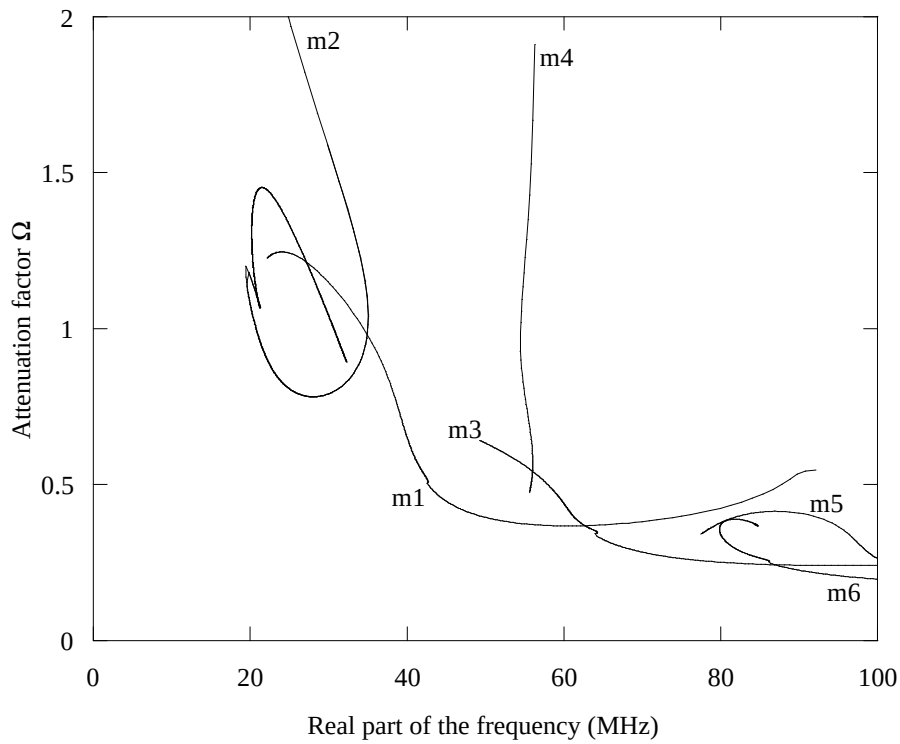

(b)

Figure 3.4: (a) Comparison of the dispersion curves (−) calculated in complex frequency and real slowness, with the reflection coefficient results as shown in Fig.3.3. (b) Attenuation factor $\Omega = \omega''/\omega'$ versus the real part of the frequency for a 0.1-mm thick layer of alpha case embedded in titanium.

3.3.2 Comparison between plane wave reflection coefficients and dispersion curves for complex frequency and real slowness

For the same configuration, let us now analyze the zeroes and the minima of both the shear and the longitudinal plane wave reflection coefficients and the dispersion curves calculated using the alternative approach of complex frequency and real slowness, shown in Fig. 3.4. Again, part (a) shows the phase velocity ($1/S_x'$) and part (b) presents the dimensionless attenuation factor $\Omega = \omega''/\omega'$. Both are plotted versus the real part of the frequency ($\omega'/2\pi$). The imaginary parts of the different modes have been plotted just to point out that Ω is always positive. Therefore, the transient parts of the signals will be characterized by exponential decreases in time. The labels m1 to m6 are arbitrary. It is interesting to observe that modes m2 and m4 exhibit a cut-off in frequency when Ω tends to infinity. This characteristic was already observed in the case studied by Poncelet and Deschamps [69]. From an experimental point of view, the hypothesis of real slowness is satisfied if very large transducers are used such that an incident wave can be considered to be a plane wave rather than a bounded beam. Also, the hypothesis of complex frequency is satisfied if the signal presents a discontinuity in time. As a result, it is interesting to note that if the slowness vector is real ($\mathbf{S}'' = \mathbf{0}$), and if a plane of constant phase is considered, then the attenuation factor in the amplitude term of Eq. 2.11 disappears which means that the waves do not leak.

Two different zones of the solution can be differentiated. Exactly below the longitudinal bulk velocity of the Titanium (c_{L1}), there only exists zeroes of the shear plane wave reflection coefficient (squares) and, contrary to Fig. 3.3, they agree very well with the dispersion curves. The existence of zeroes instead of minima could be because one wave, and one only, is reflected from the layer, the longitudinal plane wave being a surface wave beyond the critical angle associated with c_{L1}. This observation concerning the simultaneous existence of the zeroes and of a single reflected wave would be in accordance with the liquid / solid / liquid geometry discussed earlier. In that case, only longitudinal plane waves can be reflected, of course, and the zeroes exist for any incidence angle. The correlation between the zeroes and the dispersion curves for a resolution in complex frequency is then always observed, even when the immersed solid is anisotropic [69, 23, 24].

Returning to the present embedded solid case, above c_{L1} (second zone) the spectra of the plane wave reflection coefficients do not present any zeroes but only minima (circles). As an example, Fig. 3.5 illustrates the shear plane wave reflection coefficient versus the frequency at a phase velocity of 8.4 km/s, where clearly the values are described by minima instead of zeroes.

The agreement between the minima of both the shear and the longitudinal plane wave reflection coefficients and the dispersion curves degenerates progressively as the phase velocity increases, with the exception of just a few localized points. Above velocities of about 8 *km/s*, the minima and the dispersion curves are almost totally separated. The minima of

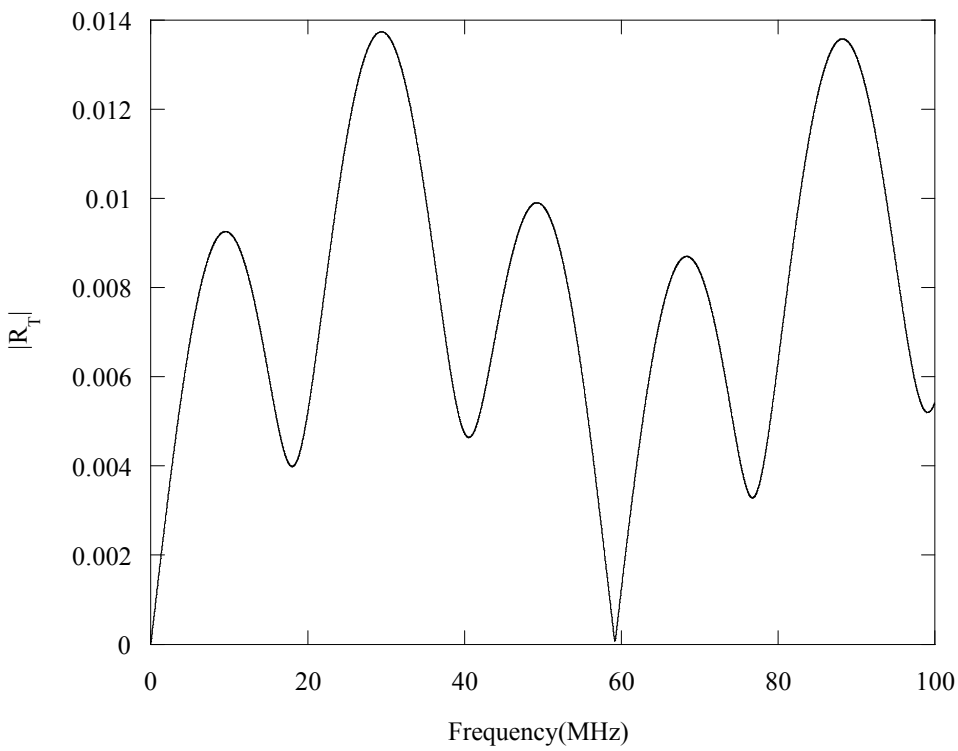

Figure 3.5: Example of poor minima in the titanium/0.1-mm alpha case/titanium structure for the shear plane-wave reflection coefficient at a phase velocity of 8.4km/s.

the longitudinal plane wave reflection coefficient (•), for example, do not correspond to any dispersion curves. The presence of minima instead of zeroes above c_{L1} may be explained by the fact that in general both shear and longitudinal plane waves are reflected when either a shear or a longitudinal plane wave is incident.

3.3.3 Consideration of minima of the complex reflection coefficient, assuming complex frequency

The minima and zeroes of the reflection coefficients were obtained assuming, conventionally, continuous plane waves (real frequency and real slowness). Let us now consider the possibility of reflection coefficients calculated with complex frequency and real slowness (transient incident waves). This will enable us to reduce the minima to zeroes by searching in the (now) complex solution space. We study for example the modes labeled m1 and m2 in Fig. 3.4.

We consider first the mode m2. Fig. 3.6(a) and 3.6(b) present the comparison between the real and the imaginary part (characterized by the dimensionless quantity $\Omega = \omega''/\omega'$) of the zeroes of the shear plane wave reflection coefficient (dashed line), and the dispersion curves (solid line) calculated in complex frequency and real slowness versus the real part

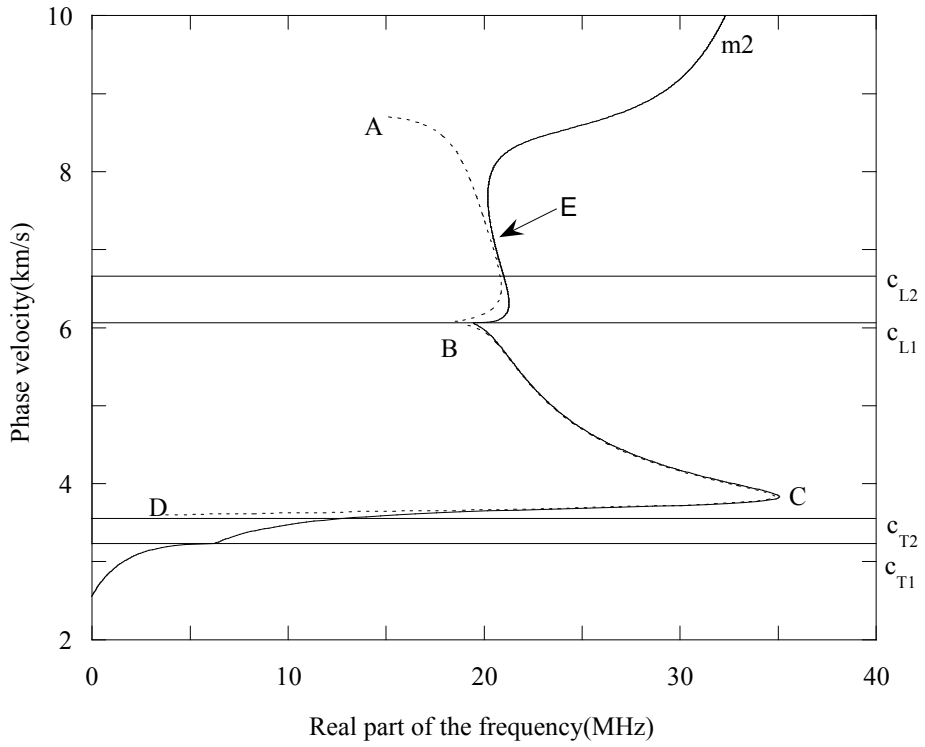

(a)

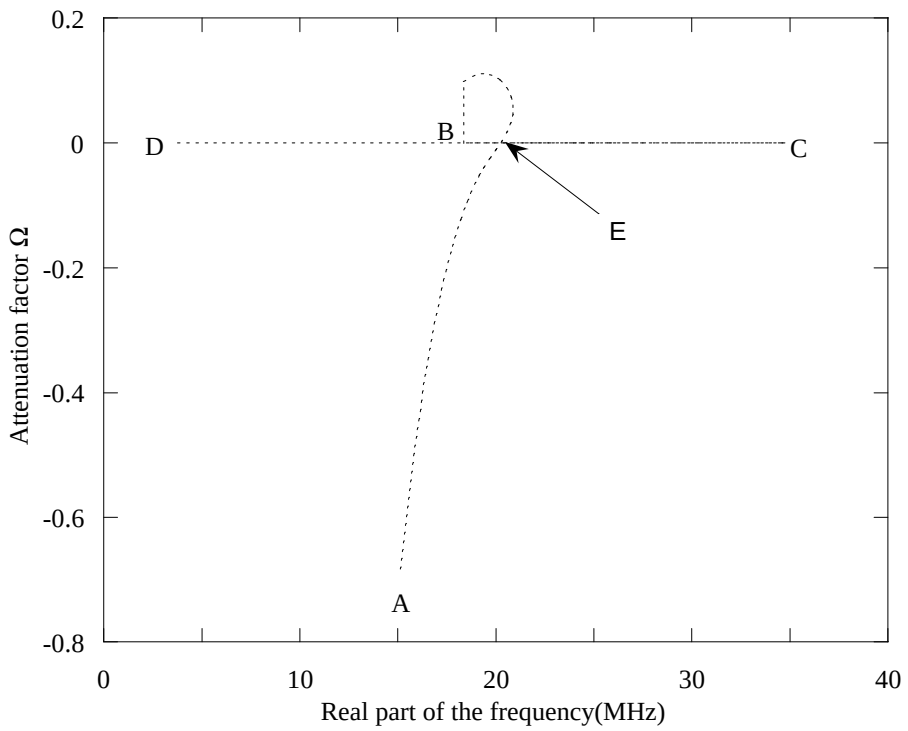

(b)

Figure 3.6: (a) Comparison between the shear plane-wave reflection coefficient(- - -) and the mode labeled *m2* in Fig. 3.4, both calculated in complex frequency and real slowness, (b) Attenuation factor ($\Omega = \omega''/\omega'$) of the zeroes of the reflection coefficient.

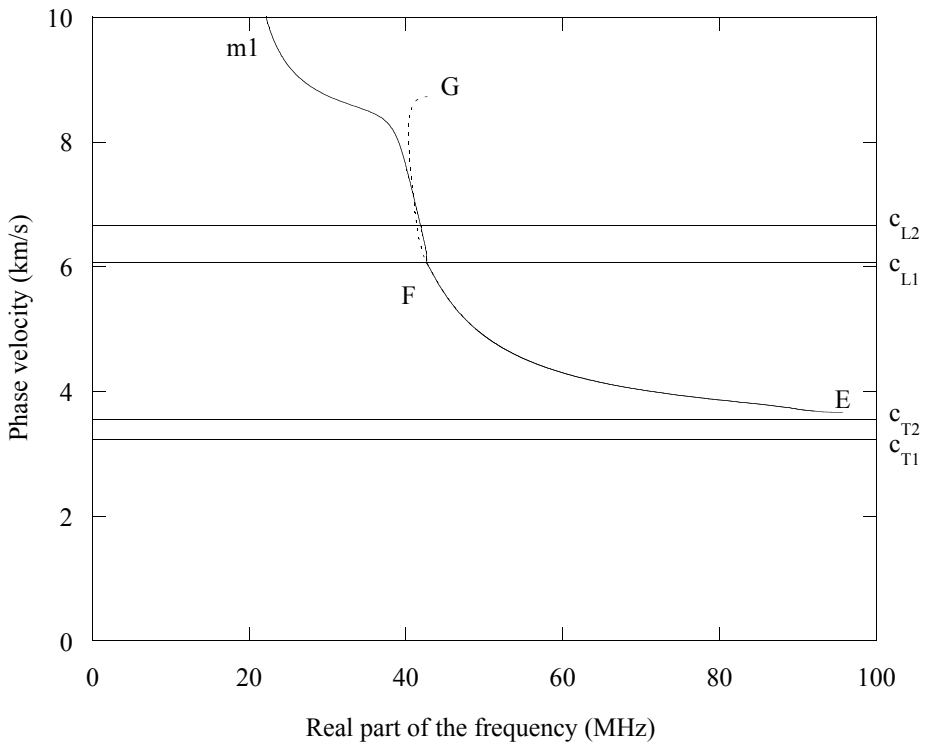

(a)

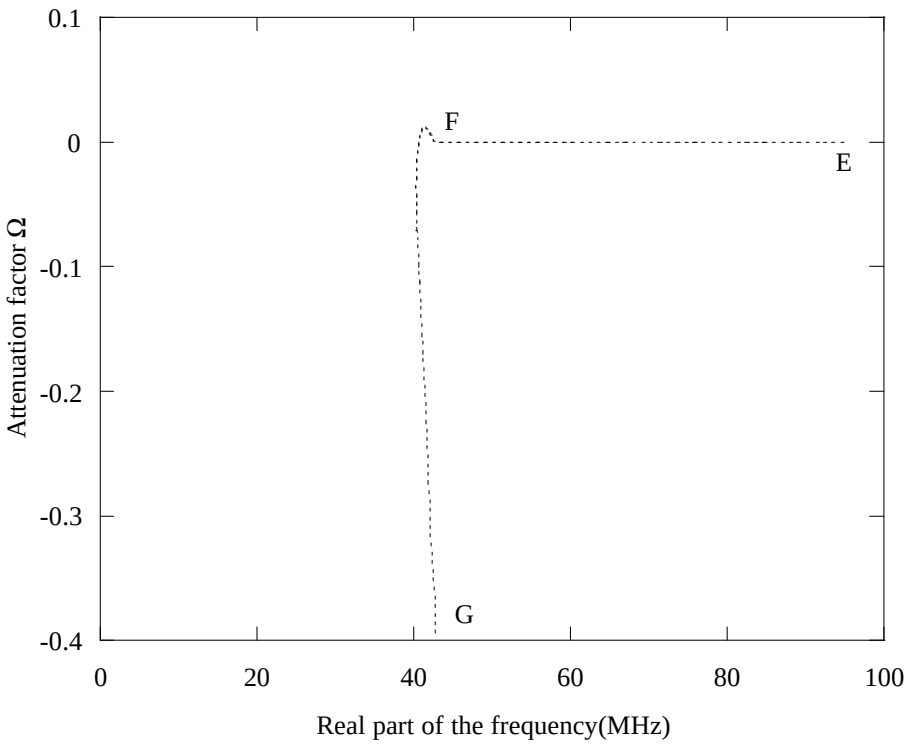

(b)

Figure 3.7: As Fig. 3.6 but for the mode *m1*.

of the frequency.

The two zones of solution identified earlier are clearly seen here since obviously the zeroes plotted earlier in Fig. 3.4 must appear here with zero imaginary part, whereas the minima must now appear with non-zero imaginary part. For example, in Fig. 3.6, the path between A and B, above the longitudinal bulk velocity of the Titanium c_{L1}, has a non-null Ω. The roots of the reflection coefficients are therefore complex and do not correlate with the dispersion curves. However, the path between B and D, below the longitudinal bulk velocity of the Titanium c_{L1}, has null imaginary parts. We can also observe that despite now being able to identify loci of reflection coefficient zeroes (rather than minima) throughout this solution space, we are still left with a divergence between the dispersion curves and the zeroes when the velocity is greater than c_{L1}. The difference is therefore clearly a fundamental characteristic, and cannot simply be a result of poor identification of minima. In addition, the larger the imaginary part of the roots, the greater the divergence between the minima and the dispersion curves. Moreover, it can be observed that above c_{L1}, the point (E) which has a null Ω, that is when the sign of Ω is changing from positive to negative values, is exactly on the dispersion curve even though both longitudinal and shear plane waves are being reflected.

The same analysis can be drawn for the other mode, m1, shown in Fig. 3.7. Again, as soon as the imaginary part of the root of the shear plane wave reflection coefficient becomes non-null (path between F and G), the zeroes (dashed line) move away from the dispersion curves (solid line). The two sets of curves have then only one point of agreement after this separation, exactly when the imaginary part crosses the **x**-axis to go from positive to negative values. The same phenomenon has been observed to occur for all the other modes.

3.4 Conclusions

Computational solutions of symmetric and antisymmetric Lamb functions and reflection coefficients have been presented for a plate embedded in a solid. A comparison between the dispersion curves obtained either in complex slowness and real frequency or in real slowness and complex frequency with the minima of the shear and longitudinal reflection coefficient has been achieved. A better correlation with the resolution in complex frequency has been shown although some regions still exhibit some disagreements. Those differences occur where the minima are poorly defined. At such locations clearly defined zeroes of the shear and longitudinal plane wave reflection coefficients may still be found by using a calculation with real slowness and complex frequency. However, these solutions still exhibit poor correlation with the dispersion curves in these regions. Regarding the implication on experimental work, it seems that the coincidence angle principle may be used reliably to measure the modal properties if the modes are calculated using complex frequency and real

slowness and if measurements are restricted to velocities lower than c_L in the embedding medium.

As a consequence, Chapter 4 presents the calculation of the response for both a fluid loaded plate and an embedded layer to an incident field which is bounded in time and in space. The plate response is then studied at different positions along the plate, modelling a receiver which would be either in or away from the specular reflected field. This has value as a clear demonstration of the temporally transient and spatially transient behaviours, and how each depends on the nature of the experimental setup.

Chapter 4

From complex frequency to complex slowness

4.1 Introduction

As explained in chapter 3, solving a guided wave problem can become very delicate since this actually depends on the variable (frequency or slowness) one chooses to fix. Harmonic leaky guided waves with real frequency and complex slowness as well as transient homogeneous guided waves with complex frequency and real slowness correspond to different sets of dispersion curves but are solutions of the same transcendental equation. For these reasons, one should be able to differentiate them during an experiment since their structure is different and they represent different physical behaviours. All the precautions must be taken at this point. As a matter of fact, the hypothesis made in both cases must be verified! This is why researchers started to think of modeling properly what they were experimentally obtaining, therefore including bounded beam effects in their model since the transducers are size-limited.

Starting from the coincidence angle principle which postulates that both zeroes and poles of the plane wave reflection coefficient of a fluid loaded plate exist at the same time for certain angles of incidence, Brekhovskikh [11] developed a detailed theory for the reflection of a bounded beam at a liquid-solid interface and showed for example that the profile of the reflected beam was different from the profile of the incident beam, which corresponds to an "energy redistribution". The profile used to model the incident beam was rectangular. In 1973, Neubauer [56] experimentally demonstrated by means of Schlieren visualization that the reflected field is composed of both specular reflection and Rayleigh wave radiation at and near the Rayleigh angle. The same year, Bertoni and Tamir [5] were the first to analytically approximate by contour integration the plane wave reflected field for an incident Gaussian beam of a liquid-solid geometry near the Rayleigh angle of incidence. In their paper, they analytically explained the nowadays well known shift of the

reflected beam from the position predicted by the geometrical acoustics and theoretically described the null or the minimum intensity in the reflected field as well as the weaker field which accompanies the reflected beam and extends for a considerable distance downstream of it. They also showed that at/or near the Rayleigh incident angle the incident beam in fact produces a geometrical-acoustics field as well as a leaky Rayleigh wave which, both superposed, create the distorted reflected field described earlier. In 1974, Breazeale *et al.* [10] did the same study using an error function to express the reflected field and did a comparison with experiments (Schlieren photographs) confirming again the distortion in the collected field. It was in 1975, that Plona *et al.* [65] studied the case of immersed plates. They experimentally showed that the results previously reported for the liquid-solid geometry was also occurring for the liquid-solid-liquid geometry in the reflected field but also in the transmitted field and that non specular effects depended on the imaginary part of the pole: if S''_x is very small the shape of the reflected field remains the same. After showing the theoretical similarities of Rayleigh and Lamb modes of vibration [62, 9], Pitts *et al.* [63] used the poles and the zeroes of the infinite plane wave reflection coefficient to derive a theoretical prediction of the non specular reflection effects observed for an ultrasonic beam incident on an isotropic plate in a liquid. Ng *et al.* [57] also studied the liquid/solid-plate/liquid configuration and solved the problem under consideration, with an integration of an approximated transmission coefficient, from both single-pole and multiple-pole formulations. Claeys and Leroy [19], however, built up the incident profile with a superposition of inhomogeneous waves, all propagating in the same direction but with different exponential decays. They showed that it is possible to obtain analytical expressions for reflected and transmitted beams at any angle of incidence, whatever the form of the incident profile. Nayfeh and Chimenti [53] presented calculations and measurements on the reflection of finite acoustic beams from a fluid-solid interface either loaded or stiffened by layers in welded contact with the solid. Some more work concerning bounded beam effects and material characterisation with zeroes of the reflection coefficient can be found in the following references [35, 73, 58, 34, 6, 16, 21, 76, 77].

All the previous studies showed how guided waves could be detected and/or excited by a bounded incident beam: if the reflected field does not correspond to the geometrically reflected incident field then a guided wave should be interacting with the plane wave reflection coefficient. However, guided waves can also be studied with another method called the Method of Isolation and Identification of Resonances (M. I. I. R). It consists of sending a long sinusoidal train in order to establish a steady state in the studied object which can then stock energy. Off a resonance, the reflected signal remains unchanged (its shape is the same than the incident signal), but near a resonance, the structure of the temporal signal exhibits the three following characteristics: the first part is an increasing or a decreasing transient, the second shows the permanent regime and the third presents a second transient regime exactly arising at the end of the forced regime and corresponding to a free re-emission of the accumulated energy. The amplitude of this re-emission increases or decreases exponentially with time like the first transient part. First used for the study of cylinders [51, 70, 71, 49, 32], Izbicki *et al.* [33] and Delestre *et al.* [20] used it to study

the resonances of an immersed plate, guided waves existence being considered as plate resonances [47, 26, 27, 28]. In 1986, Maze *et al.* [50] explained that the distortion of the shape of the wave train and the shape of the simultaneously appearing tail of the wave train which represents the ringing of nearby plate resonances, are the result of the interference of a directly reflected pulse with a series of multiply internally reflected pulses.

Although it is clear now that guided waves represent plate resonances, they can be studied both in time and in space. The resonances in time are characterized by exponential transients whereas they are characterized by minima accompanied with a field which becomes weaker and weaker away from the reflected field in space. As leaky guided waves are excited by spatially bounded beams, transient guided waves are generated when the emission of the source is finite in time. The aim of this chapter is then to present these two different approaches in order to finally look at the effects of an incident beam which would be bounded both in time and in space. After a quick recall of the Fourier theory, the next sections will present the three following situations:

1. the frequency is complex and the slowness is real (transient Lamb waves)
2. the frequency is real and the slowness is complex (harmonic leaky Lamb waves)
3. transition between the two different situations

4.2 Fourier theory

The aim of this section is to briefly describe the field reflected by a plate immersed in water or embedded in a solid. The studied geometry is the same as in chapter 3 shown in Fig. 3.2. The incident field is supposed to be infinite in the **z**-direction. The plane of incidence is defined by the axis (**x**,**y**), the central axis of the incident beam making an angle θ with the normal to the plate. Using Fourier transforms, if the displacement field is known on a given plane ($y = y_0$), the potential field in an observation point (x, y) and at a time t can be expressed by the bi-dimensional Fourier integral:

$$\varphi(x, y, t) = \frac{1}{4\pi^2} \int_{-\infty}^{+\infty} \int_{-\infty}^{+\infty} \Theta(\omega, k_x, y = y_0) H(\omega, k_x, y) e^{i(\omega t - k_x x)} dk_x d\omega \tag{4.1}$$

where k_x is the wavenumber projection on the interface, $\Theta(\omega, k_x, y = y_0)$ is the transfer function of the emitter and $H(\omega, k_x, y)$ is the transfer function of the plate. In this study:

$$H(\omega, k_x, y) = e^{-ik_y l} R(\omega, k_x) \tag{4.2}$$

where $R(\omega, k_x)$ is the plane wave reflection coefficient of the plate defined in Eq. 3.15 ($\xi^+_{L1,T1}$), $k_y = \omega S_{yT1,L1}$ (T if the incident wave is shear, L otherwise), $S_{yT1,L1}$ being defined in Eq. 3.9. The exponential factor represents the propagation in the surrounding medium from the emitter to the plate and from the plate to the receiver, the distance travelled corresponding to l.

Although time and space are indissociable during an experiment, in order to simplify the calculation, we make the assumption that the initial acoustic field in the emitter plane is the product of a Fourier transform of a time function by a Fourier transform of a space function:

$$\Theta(\omega, k_x, y = y_0) = A(k_x)E(\omega) \tag{4.3}$$

where $A(k_x)$ and $E(\omega)$ respectively correspond to the spatial and to the temporal spectral densities of the transducer. The incident acoustic field will be spatially assimilated to a Gaussian function and temporally assimilated to a square function. The square function has the benefit of containing both steady state and transient portions. It is to be noted that the choice of other symmetrical spatial profiles will not appreciably affect the results provided the other beams possess large effective cross-sections inside which the field intensity is very strong compared to the exterior fields [5] (the Gaussian repartition is used to model most transducers). Therefore, the spatial field is defined by:

$$a(x) = Ae^{-\sigma^2(x-x_0)} \tag{4.4}$$

where A is an arbitrary amplitude, σ is the width of the spatial field for a half amplitude and x_0 the initial position of the emitter. Its Fourier transform can easily be deduced:

$$A(k_x) = A\sqrt{\frac{\pi}{\sigma^2}}e^{\frac{-\pi^2 k_x^2}{\sigma^2}}e^{ik_x\pi x_0} \tag{4.5}$$

The time function used to simulate a square signal is defined by:

$$e(t) = [H(t - t_0) - H(t - t_0 - T)]e^{i\omega_0(t-t_0)} \tag{4.6}$$

where $H(t)$ is the Heaviside function, t_0 a time delay and T the duration of the signal. The Fourier transform of the signal e(t) is then given by:

$$E(\omega) = \frac{i}{\omega - \omega_0}\left[e^{i(\omega-\omega_0)T} - 1\right]e^{-i\omega t_0} \tag{4.7}$$

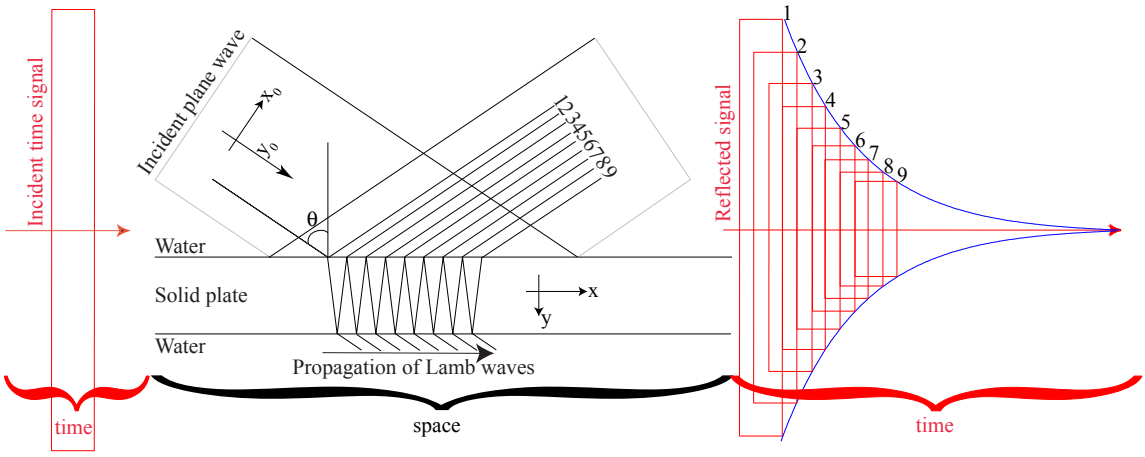

Figure 4.1: Experimental configuration for the resolution in complex frequency and real slowness.

4.3 Transient Lamb waves

As explained in the introduction it is of key importance to make sure that all hypotheses made in a problem are satisfied. In this section, we want to study transient guided waves which are waves whose amplitudes decay only in time but not in space ($^*\omega, S_x$). Moreover, we know that bounded beam profiles generate leaky guided waves. As a consequence the hypothesis of real slowness is satisfied only if no spatial discontinuities arise. Hence, experimentally speaking, the emitter should be very large in order to simulate an incident plane wave which is infinite in space and the receiver should be placed in the specular reflected field as shown in Fig. 4.1. In this model, the spatial acoustic field is then considered as a unit function $a(x) = 1,\ \forall\ x$ and therefore the potential defined in Eq. 4.1 is reduced to a single integral over the frequency domain:

$$\varphi(t) = \frac{1}{2\pi}\int_{-\infty}^{+\infty} R(\omega, \frac{\sin\theta_{L,T}}{c_{L,T}})E(\omega)e^{i\omega t}d\omega \tag{4.8}$$

From an experimental point of view such behaviour is achievable. Poncelet and Deschamps [24, 68] obtained very good results with a rectangular plane wave emitter whose dimensions are 80x40 mm and whose center frequency is about 3 MHz (this corresponds to about 70 wavelengths at 2 MHz in the water). At 30 cm from the emitter they showed that the wave front collected by a 3/4″ typical broad-band transducer of 2.25 MHz is a plane with a constant amplitude in an area of about 50 mm in width. Hence, at the center frequency of the beam, the assumption of plane waves can be well justified and the spatial bounded beam effects can be limited considerably.

As the response of a plate can be associated with the poles of the plane wave reflection

coefficients in the frequency domain, we decided to numerically study the case of a 1-mm thick steel plate embedded in aluminium to see if zeroes of the shear plane wave reflection coefficient effectively coincide with the modal properties of the structure. This situation, although similar to the previous studies for immersed plates, includes the presence of a shear plane wave also reflected by the plate into the surrounding medium. Among the large number of existing modes we only focus our attention on the modes S_0 and A_0. Those two modes have been chosen because, as in the case studied by Poncelet and Deschamps for a fluid loaded plate, a cut-off in frequency exists for the two modes and A_0 has a negative attenuation (the temporal exponential should be an increasing transient instead of a decreasing transient). This is an interesting case to develop understanding but unfortunately unsuitable for experimentation. As a matter of fact, also the thickness of the adhesive, in order to bond the different solids, were very small compared to the wavelength used in our experiments and compared to the plate thicknesses, the results were unworkable and completely different from the solid/solid/solid model.

The properties of the media are the following: $c_{L1} = 6.37\ m/ms$, $c_{T1} = 3.1\ m/ms$, $\rho_1 = 2.8\ g/cm^3$ for the embedding medium and $c_{L2} = 5.96\ m/ms$, $c_{T2} = 3.26\ m/ms$, $\rho_2 = 7.932\ g/cm^3$ for the embedded layer. The phase velocity dispersion curves of the two modes are shown in part a) of Fig. 4.2 while the attenuation factor Ω is illustrated in part b).

Two numerical simulations have then been carried out at different angles of incidence. The angle to excite A_0 is 87.48° and corresponds to a phase velocity of 3.103 m/ms whereas the angle to excite S_0 is 65.27° which corresponds to 3.413 m/ms. In those conditions, even if both a longitudinal and a transversal plane wave are reflected by the interface, the longitudinal reflected wave remains an interface wave (we are above the critical angle). Then as explained in Chapter 3 the plane wave reflection coefficient should only have zeroes but no minima and the agreement with the complex frequency dispersion curves should be ideal. The frequencies of the carrier wave, in order to excite A_0 and S_0, have been chosen in such a way that they correspond to the frequencies labelled in Fig. 4.2(b). The incident signal has 100 cycles and is 20 μs long for A_0 but 15 μs long for S_0. In fact, the length of the signal depends on the imaginary part of the frequency of the mode we want to excite: the lower Ω the longer is the signal. The numerical results are presented in Fig. 4.3. Part a) and b) show the temporal responses of A_0 and S_0 respectively, while part c) and part d) show the logarithm of their envelopes. It is to be noted that although a large number of cycles is necessary in order to visualize the two transients at the beginning and at the end of the steady state (we do not want any overlapping), they also contribute in the reduction of the frequency spectrum bandwidth and then in the accuracy of the model (the angle of incidence is fixed and the working frequency is almost unique).

As expected, the response of the plate for the two modes exhibits the two characteristic behaviours: a transient part at the beginning and at the end of the steady state and a null amplitude during the steady state (the infinite plane wave reflection coefficient is null for

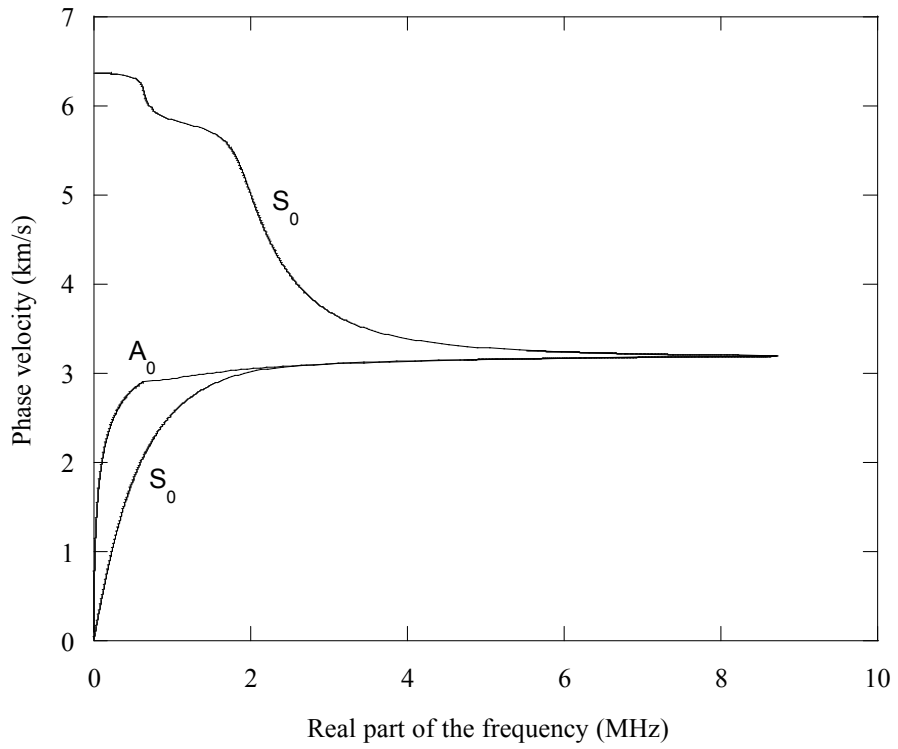

(a)

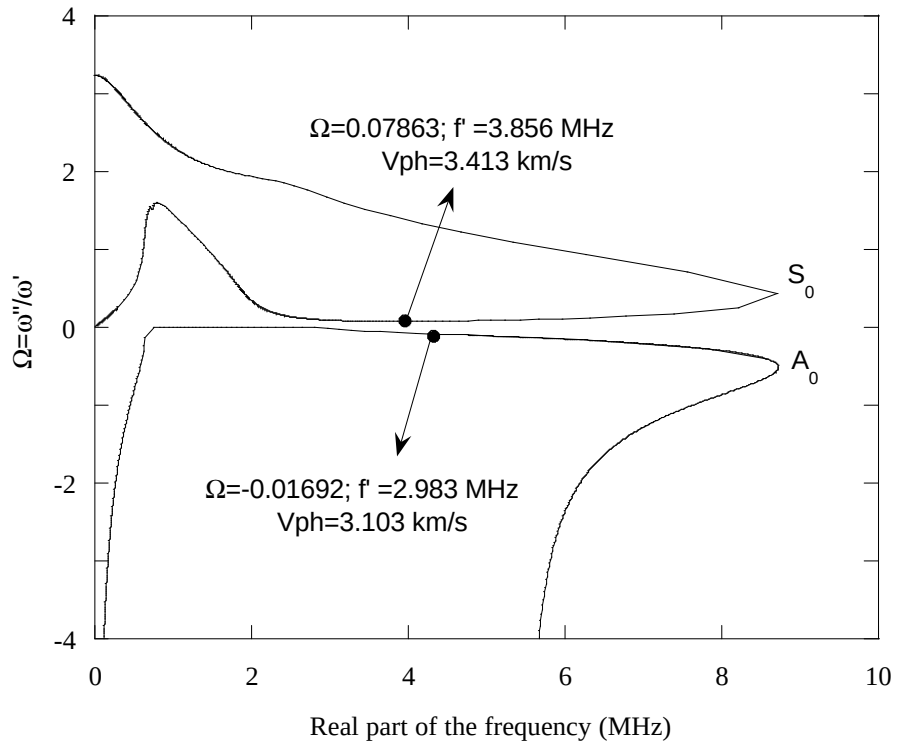

(b)

Figure 4.2: Dispersion curves calculated in complex frequency and real slowness (modes S_0 and A_0) for a 1-mm steel plate embedded in aluminium: (a) Phase velocity (b) Attenuation versus the real part of the frequency.

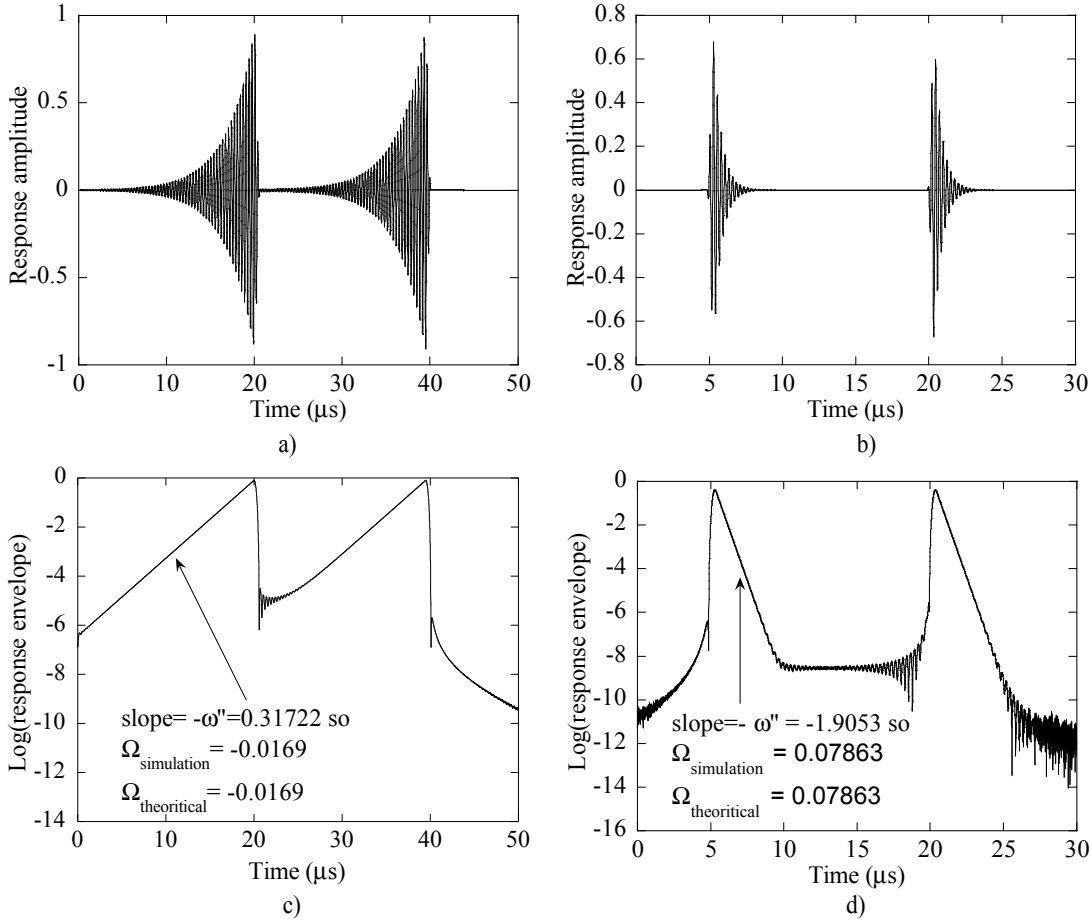

Figure 4.3: Predicted plate response to a long duration plane wave signal at a frequency of (a) 3.856 MHz, (b) 2.983 MHz. Part (c) and (d) show the logarithm of the envelopes of the response displayed in part (a) and (b). $\Omega_{simulation}$ refers to $slope/(2\pi * carrier frequency)$ whereas $\Omega_{theoretical}$ refers to the dispersion curves presented in Fig. 4.2.

these angles of incidence and for these frequencies).

As a matter of fact, the incident signal is a square signal which is null everywhere except between a time t_0 and a time $t_0 + T$. In this zone, there only exists one frequency ω_0 and the signal is then harmonic. As the reflection coefficient is null for those particular values of (ω, θ) the result is zero between t_0 and $t_0 + T$. The only information which appears are the transient parts of the signal at t_0 and $t_0 + T$ whose lengths depend on the value of ω''. The formation of the transient parts is schematically illustrated on the right hand side of Fig. 4.1 for the nine first reflected waves and is the result of destructive interference between all those multiple internal reflections. A full description can be found in Ref. [50]. The transient parts are increasing exponentially for A_0 but decreasing exponentially for S_0: in Fig. 4.2, Ω is positive for S_0 but negative for A_0. Moreover, the logarithm of the envelopes of the two different responses have been calculated and are shown in Fig. 4.3(c,d). As expected, the two straight lines confirm the fact that the two plate responses are exponential functions. Moreover, the slopes of the two straight lines, which correspond to the parameter ω'' for a wave which is attenuated in time, have been calculated. They

are respectively equal to $\simeq -0.317\ MHz$ for ω''_{S_0} and to $\simeq 1.9\ MHz$ for ω''_{A_0} and are also labelled on Fig. 4.3. They are rigorously equal to the predicted attenuation of the modes calculated by the resolution of the modal problem (see Section 3.2.2). As a consequence, the transient parts of the reflected signal contain information about the modal properties of the plate. Finally, as explained in chapter 3 we can also observe that the modal properties correspond to a zero of the reflection coefficient.

4.4 Harmonic leaky guided waves

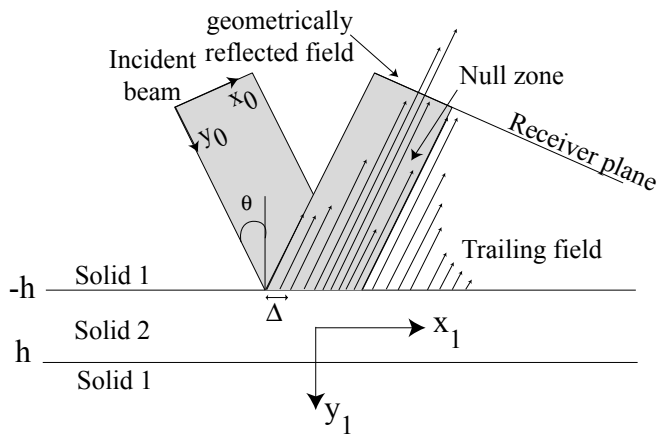

Figure 4.4: Experimental configuration for the resolution in complex slowness and real frequency.

For this kind of experiments the aim is to look at Lamb waves which are leaking energy in the surrounding media as they are travelling along the plate. Contrary to the previous section, the attenuation is no longer in time but now in space. The frequency is real, the signal is supposed to be a unit function: $e(t) = 1,\ \forall\ t$ but the beam is now bounded. In those conditions, the double integral defined in Eq. 4.1 reduces to a single integral and the potential field can be rewritten:

$$\varphi(x, y) = \frac{1}{2\pi} \int_{-\infty}^{+\infty} R(\omega, k_x) A(k_x) e^{-i(k_x x + k_y l)} dk_x \tag{4.9}$$

As explained in chapter 3, as the dispersion curves in complex slowness and real frequency do not fit at all the zeroes of the plane wave reflection coefficient when the plate is embedded, this section only presents the case of a steel plate immersed in water in order to illustrate the phenomena induced by a bounded beam. Although this recalls the well known results already presented by many authors and referenced in the introduction, this section will later be useful in order to understand the behaviour of the reflected field when both time and space are bounded. The experimental setup is shown in Fig. 4.4. Without

loss of generality we can assume that the propagation length in the surrounding medium is null ($l = 0$) since this only spreads the results but does not change the properties of the spatial exponential decreases. The overlapping is then avoided and this assumption will remain valid until the end of this chapter.

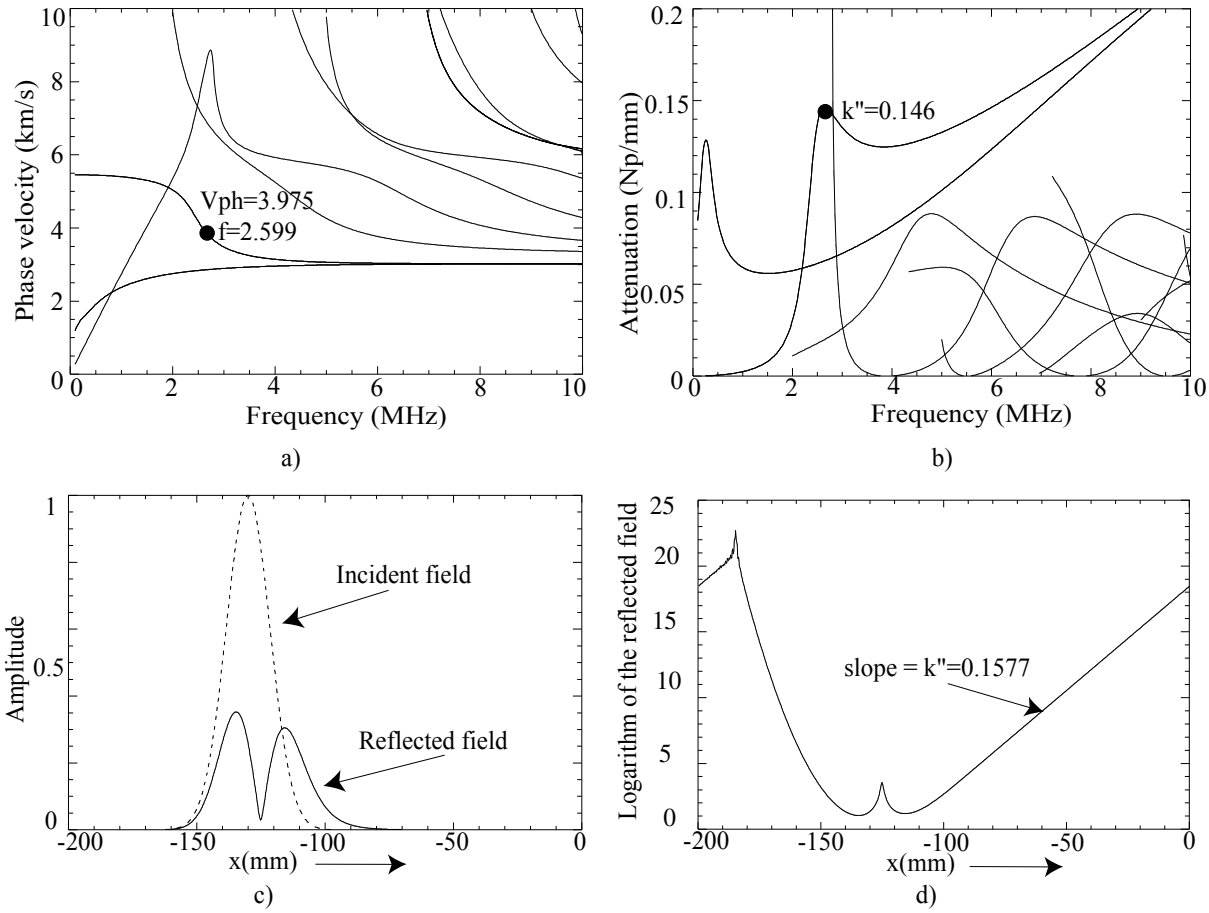

Figure 4.5: Top: dispersion curves calculated in complex slowness and real frequency for a 1-mm steel plate immersed in water. Bottom: response of the plate to a bounded incident beam whose frequency and angle of incidence (or phase velocity) are labelled with a black circle (•) in parts a) and b).

The incident bounded beam is modelled by a superposition of planes waves corresponding to a Fourier integral. The shape of the incident wave form being a Gaussian function, its Fourier transform is a Gaussian function as well. The numerical results are obtained after the following steps: for a given displacement field in the surrounding medium $a(x)$ centered in x_0, we calculate the Fourier transform and get $A(k_x)$ with reference to the coordinate system of the transducer $R_0(x_0, y_0)$ making an angle θ with the reference to the coordinate system of the plate $R_1(x_1, y_1)$. Then, for each k_x in the surrounding medium, the other component of the wavenumber is calculated with the dispersion relation:

$$k_{z|R_0} = \pm\sqrt{\frac{\omega^2}{c_{L1}^2} - k_x^2}, \tag{4.10}$$

the sign of $k_{z|R_0}$ being chosen in such a way that the amplitude of the wave decreases as its distance from the plate interface increases. The projection of the wavenumber on the interface is easily deduced by a simple rotation over θ:

$$k_{x|R_1} = k_{x|R_0} \cos(\theta) + k_{z|R_0} \sin(\theta) \tag{4.11}$$

Hence, for each $k_{x|R_1}$ in the plane of the plate, the integral defined in Eq. 4.9 can be evaluated. It is to be noted that the calculations are only made for real wave numbers ($|k_{x|R_0}| <= k_{L1}$).

Our simulation is configured to excite S_0 in a 1-mm thick steel plate immersed in water. The different curves are illustrated in Fig. 4.5. Part a) shows the phase velocity dispersion curves while part b) shows the attenuation (k''_x). On the black circle, S_0 has the following properties: ($V_{ph} = 3.975\ km/s$, $f = 2.599\ MHz$, $k''_x = 0.146\ Np/mm$ and the incident angle in the water corresponds to $\theta = 22.17°$. The Gaussian beam width for a half amplitude is $\sigma = 20\ mm$ and the incident field is shown in dotted line in part c) of the figure. The response of the plate to the spatially bounded beam is also traced in part c) of the figure in solid line. The results are in accordance with the theory and clearly indicate the three main effects caused by a bounded beam which are: the typical shift, the minimum in the reflected beam and the trailing zone which becomes weaker and weaker (this is a decaying function). Part d) shows the logarithm of the reflected field and the value of the slope is also indicated. This slope, which represents the spatial attenuation with reference to the coordinate system of the receiver, does not correspond to the modal attenuation. As a matter of fact, the modal attenuation refers to the guided waves attenuation along the plate. Then with a simple projection on the plate axis we obtain $k''_x = 0.1577 * cos(22.17) = 0.146\ Np/mm$ which exactly equals the predicted attenuation labelled on part b) of Fig. 4.5.

4.5 Transient bounded beam

In this section we study the general case where both time and space are bounded. As explained in section 4.2 the field reflected by a plate can be evaluated at any time and at any position in the receiver plane as long as the incident field is known both in time and in space. As the numerical calculations are done in the frequency space as well as in the wavenumber space, the reflected field is the result of a double inverse Fourier transform. The two limit cases being already presented in the two previous sections, we intend to study the link that may experimentally exist between these two ways of solving the guided wave problem. For a fixed incident angle and for a given temporal signal, it is possible to look at the reflected field in the receiver plane at any position over the length of study. This can be in either of the three zones described in section 4.4 that is the specular

reflection, the null intensity zone or the spatially exponentially decreasing zone. Then, for each position, the time signal can be evaluated and inversely the reflected field can be obtained at any time. However, the modal analysis takes place in the frequency domain and the most appropriated curves to describe the differences between the two methods are the phase velocity dispersion curves. As a consequence, the frequency domain being more suitable for comparisons with dispersion curves, we restrict our analysis to the space and to the frequency domains. This method, faster because it only requires a single inverse Fourier transform, allows us to study the frequency spectrum at any position in the receiver plane for a fixed angle of incidence or inversely the reflected field can be obtained at any frequency. The reflected field is then defined by:

$$\varphi(x, y = y_0, \omega) = \frac{1}{2\pi} \int_{-\infty}^{+\infty} E(\omega) A(k_x) R(\omega, k_x) e^{i(\omega t - k_x x)} dk_x \tag{4.12}$$

The aim being to look at the reflected field spectrum over a wide range of frequencies (from 0 to 10 MHz/mm), we decide to use a delta function in time ($e(t) = \delta(t - t_0)$) in order to excite all the frequencies with the same power. It is however important to understand that this formulation is experimentally unrealistic. As a matter of fact, in most studies the working frequency of the transducers is chosen in such a way that it corresponds to the mode we want to excite which avoids the necessity to do any signal processing that might be time consuming and sometimes very difficult to implement. In order to get nearer to the reality, the length of study is then going to be frequency dependent. In such a way, the wavelength remains constant at any frequency. From an experimental point of view this is equivalent to changing the transducer in order to excite high frequency modes rather than low frequency modes and that is what is done during an experiment! Low frequencies require large spatial lengths of study (large wavelength) whereas high frequencies require smaller lengths of study (small wavelength).

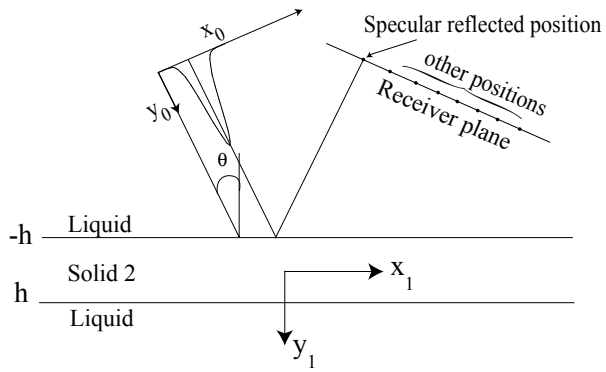

Figure 4.6: Experimental configuration showing the different positions at which the frequency spectrum is collected.

In this context, we then first study the case of a 1-mm thick steel plate immersed in

water. The incident signal is set up in such a way that its frequency spectrum varies from 0 to 11.11 MHz. The incident beam is a Gaussian function whose width σ is 20 mm at half amplitude. The incident angle varies from 8.627° which corresponds to a phase velocity of 10 m/ms to 90° for 1.5 m/ms. For each angle of incidence, we store the frequency spectrum at different positions along the receiver plane (see Fig. 4.6). The results are presented in Fig. 4.7.

Each image represents the simulated modulus of the reflected field as a function of frequency for different angles of incidence or phase velocities at a fixed position away from the specular reflected ray. The dark regions refer to high amplitudes whereas the light regions refer to low amplitudes and the color normalisation has been done according to both the maximum and the minimum of the whole data contained in all eight plots . The first image (a) describes the reflected field characteristics at the specular reflection whereas the last image (h) describes the reflected field properties far away from the specular reflected field. The different positions, for a frequency of 1 MHz, respectively correspond to 0 mm for part a) (this is the geometrical specular reflected ray), 10, 20, 30, 40, 50, 60 mm for parts b), c), d), e), f), g) and 100 mm for part h).

As expected, part a) illustrates well the modal properties of the plate also characterized by zeroes or minima (white color) in the specular reflected field. Then, when one moves away from the specular reflected field, minima start transforming into maxima and maxima start transforming into minima but they still describe the same modal properties: the shape of the dispersion curves, although described in some cases by minima and in other cases by maxima do not change at all. They are neither shifted nor distorted.

Moreover, at the longitudinal bulk velocity of steel all the symmetric modes have an attenuation which is almost zero: they cannot be excited because of the weak coupling between the plate and the water [6]. As a consequence, while the modes are described by minima in the whole picture of part a) for example, they are however described by maxima at or near c_L. The same behaviour of course occurs in all other cases where the amplitudes near this velocity are inverted from the amplitude of the other modes.

In the last image (part h), that is when the field is calculated at the furthest distance from the source, only a few parts of the modes remain visible. In order to understand why, the phase velocity dispersion curves calculated in real frequency and complex slowness with the corresponding attenuation are presented in Fig. 4.8 (we are far from the source and so the resolution in complex frequency is not appropriate). The attenuation is shown on the top of the figure and is also included in the thickness of the different lines. Thick lines correspond to low attenuation whereas thin lines correspond to high attenuation. As expected, the only remaining modes in part h) of Fig. 4.7 correspond to modes with low attenuation. This is of course physically understandable since we are looking at the reflected field far away from the source. Because the modes propagated and leaked all their energy into the fluid they cannot be detected. On the other hand, the modes with low

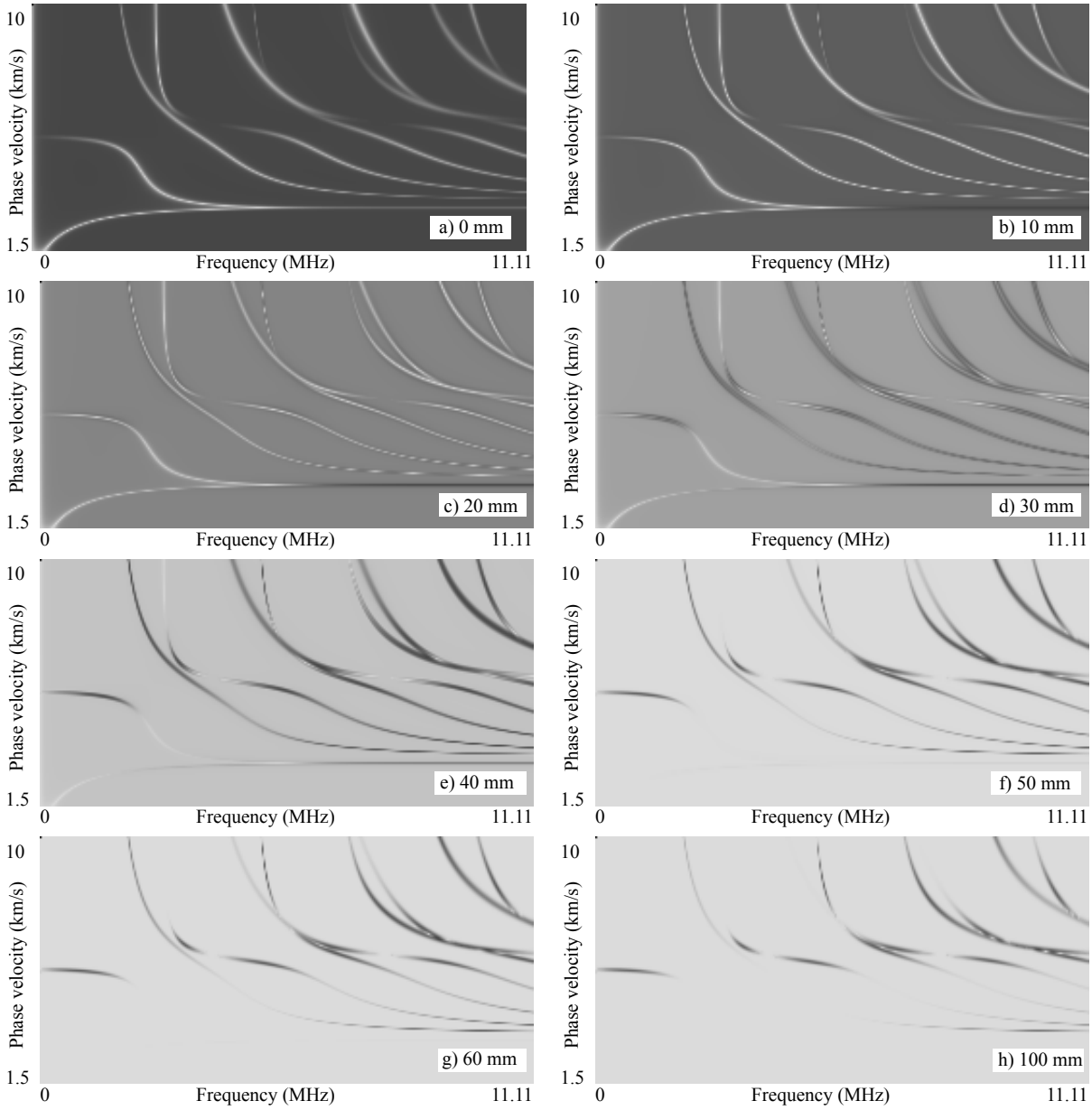

Figure 4.7: Dispersion curves-like images showing the modulus of the reflected field at different positions on the receiver plane. Plate is 1-mm thick immersed in water and the incident beam is bounded spatially.

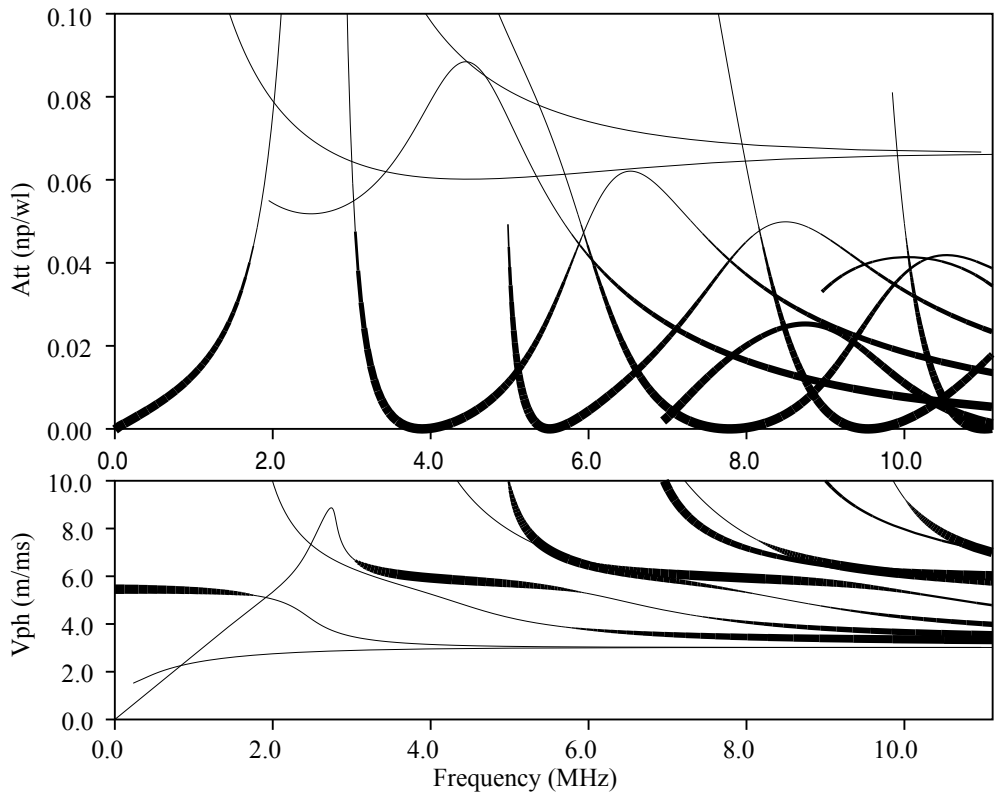

Figure 4.8: Dispersion curves calculated in real frequency and complex slowness for a 1-mm thick steel plate immersed in water. Top is attenuation ($\omega S''_x$) and bottom is phase velocity ($1/S'_x$) both versus the frequency. To aid comparison, the lines are plotted with thicknesses which is inversely proportional to attenuation.

attenuation propagate over longer distances and are still detectable even far away from the specular reflected field.

At this point, it is interesting to cite the work achieved by Lobkis *et al.* since 1996. They presented an approximated but highly accurate analysis for the reflection of bounded acoustic beams from fluid loaded structures demonstrating the relationship between the plane wave reflection coefficient and the transducer voltage [41]. They showed that the correspondence of the reflection coefficient zeroes, in both angle and frequency, with the observed minima depends critically on the experimental geometry, especially the lateral transducer placement. In their paper, they also demonstrated that minima in the reflected field could become maxima depending on the position of the receiver. To validate their work, they also did experiments in order to characterize an anisotropic plate immersed in water [39, 40]. Our results are then in accordance with their theory.

Let us now study a case where the dispersion curves calculated in complex frequency and real slowness and the dispersion curves calculated in real frequency and complex slowness present much more differences, especially for S_0 and A_1. The studied material is now a

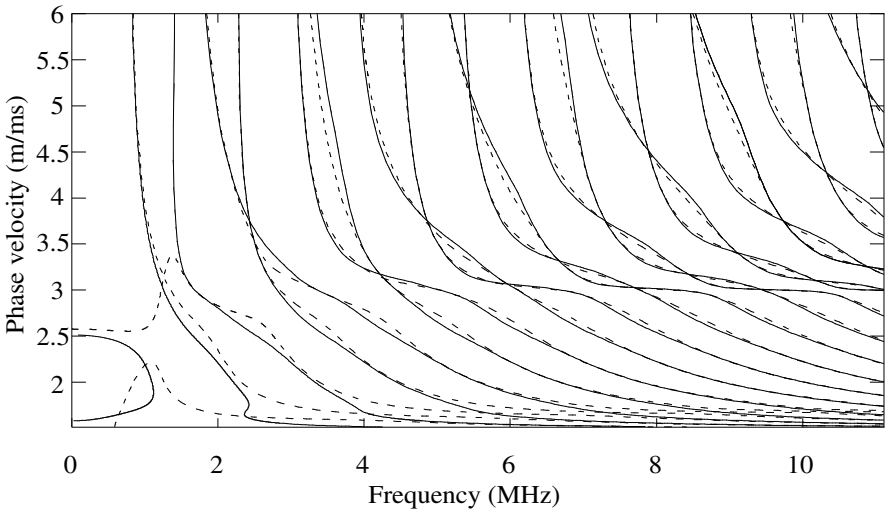

Figure 4.9: Dispersion curves calculated in real frequency and complex slowness (dashed lines) and in complex frequency and real slowness (solid lines) for a 1-mm thick anisotropic plate immersed in water.

highly anisotropic material whose density is $\rho = 1.578\ g/cm^3$ and whose elasticity tensor matrix expressed in the coordinates (**x**,**y**,**z**) is in (GPa):

$$\begin{pmatrix} 13.92 & 6.92 & 6.44 & & & \\ 6.92 & 13.92 & 6.44 & & 0 & \\ 6.44 & 6.44 & 100.73 & & & \\ & & & 7.07 & & \\ & 0 & & & 7.07 & \\ & & & & & 3.5 \end{pmatrix}. \tag{4.13}$$

The study is made for an azimuthal angle of 0°, which corresponds to a propagation plane in the coordinate system (**x**,**y**). The plate is 1-mm thick and still immersed in water. The dispersion curves are presented in Fig. 4.9. Solid lines stand for solutions in complex frequency and real slowness whereas dashed lines correspond to solutions in real frequency and complex slowness. Although the curves seem to correlate quite well for high phase velocities as shown in Fig. 4.10, strong differences appear for low phase velocities near the longitudinal bulk velocity of the water. As in the previous example, the reflected field modulus is displayed for several angles of incidence over a range of frequencies at several positions along the receiver plane. Parts a), b), c), d), e) and f) correspond respectively to the following distances from the specular reflected field: 0, 10, 20, 30, 40 and 50 mm. Again, the dispersion curve-like images really describe the dispersion curves calculated in complex frequency and real slowness as shown in part a) where the dispersion curves from Fig. 4.9 are directly compared with the reflected field modulus in the specular reflection. Far from the source, there only exist modes with very low attenuation (attenuation not shown for simplicity).

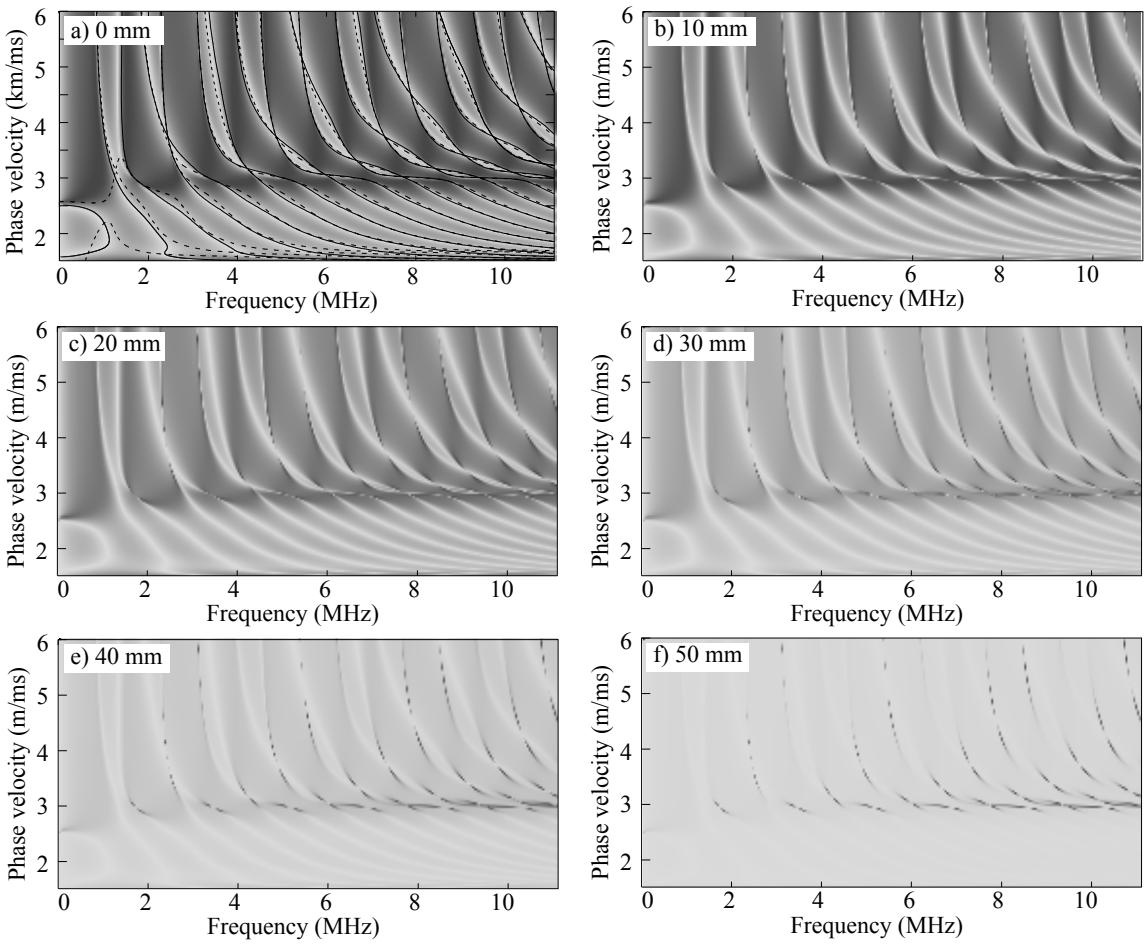

Figure 4.10: Reflected field modulus at different positions along the receiver plane for a 1-mm thick highly anisotropic plate immersed in water. Part a) also shows the dispersion curves (solid and dashed lines).

4.6 Conclusion

The response of a plate to a spatially and temporally bounded beam has been numerically studied. The results for the simpler cases where only one or other of the two different spaces is bounded have been analysed. In both configurations the modal properties of the plate are linked to the zeroes of the plane wave reflection coefficient and the attenuation of the modes can be evaluated in time or in space. However, when the two spaces are bounded, the results clearly depend on the position of the receiver. Placed in the specular reflected field, zeroes in the reflected field correspond to solutions calculated in complex frequency and real slowness. Far away from the source the modal properties of the plate are no longer described by zeroes but by maxima and they are still in accordance with the two sets of dispersion curves. Moreover, the only remaining parts in the far field correspond to modes with very low spatial or temporal attenuation. As a conclusion, complex frequency and real slowness dispersion curves appear always to fit the zeroes of the plane wave reflection coefficient. On the other hand, real frequency and complex slowness so-

lutions only agree with the zeroes of the plane wave reflection coefficient for modes with very low attenuation. In that case their phase velocity dispersion curves also correspond to those for complex frequency and real slowness, although the attenuations are of course different. Then the two kinds of mode may still exist even far from the source.

In most non destructive testing applications using guided waves, if the phase velocity remains an important parameter to distinguish a mode from another at a fixed frequency, the group velocity is also of key importance. However, this parameter is only valid and usable for non viscoelastic isotropic plates when the modes are not attenuated. In the next chapter the calculation of guided waves energy velocity is presented for different configurations of lossless or viscoelastic plates immersed in a fluid or in vacuum.

Chapter 5

Guided waves energy velocity in absorbing and non-absorbing plates

5.1 Introduction

The motivations which drove us to study the energy velocity concept instead of the group velocity arose because of the discontinuities and the unacceptable values (greater than the longitudinal bulk velocity of the material) obtained when calculating the group velocity of attenuative guided waves propagating within an isotropic plate immersed in a fluid. In fact, we will show that the group velocity definition is only valid in the non attenuating cases when the wavenumber is real and can be substantially in error when the waves are attenuative. This anomaly motivated us to perform a strict derivation for the energy velocity in attenuating harmonic waves ($\omega'' = 0$) and then compare the results with the simple group velocity expression.

A great deal of work has already been published concerning group velocity and energy velocity. In 1951, Broer [12] considered when and why the rate of energy propagation of waves, in a one dimensional conservative system without dissipation, equals the group velocity. Using the method of stationary phase he demonstrated that everywhere in the wave system the energy is propagated with the group velocity corresponding to the local wavenumber. Biot [7], in 1957, showed that there is a rigorous identity between the group velocity and the velocity of energy transport in non-homogeneous media with or without anomalous dispersion. After a survey of the theory of group velocity for one-dimensional and three-dimensional, isotropic and anisotropic, homogeneous and inhomogeneous, conservative and dissipative, linear and non-linear systems exhibiting wave propagation under free and forced motion condition from Lighthill [38], Hayes [30] showed in 1977 in a simpler way that the energy flux velocity vector for a single infinite train of elliptically polarised harmonic small amplitude plane waves propagating in a homogeneous conservative, dispersive system is equal to the group velocity. Then it was in 1979 that Hayes and Musgrave

[31] explained that the equivalence between group velocity and energy velocity does not hold true in general for inhomogeneous waves. This was confirmed for example by Poirée [66] in 1984, who demonstrated that the energy velocity of the spatially dispersive plane evanescent wave solution of the linear acoustic equation in a perfect fluid is equal to the phase velocity instead of the group velocity. It was also shown by Borejko [8] in 1987 and by Mainardy [48] who postulated that when the energy is not conserved, the identification of energy velocity with the kinetic concept of group velocity is not valid. Finally, Deschamps, Poirée and Poncelet [22] showed that the energy velocity of complex harmonic plane waves, characterized by a complex wave vector and a complex frequency, may be interpreted as the phase velocity in the direction of the real part of the slowness bivector.

This chapter examines the calculation of the energy velocity in guided waves by integrating the energy velocity vectors through the depth of the plate and over a temporal cycle, as set out for example by Auld [4]. Results using this approach, which is general in its applicability to guided waves, are then obtained for three specific guided wave cases and compared to the group velocity solutions. First the Lamb waves in a non-absorbing isotropic plate in vacuum are studied in order to demonstrate the agreement, in this lossless case, of the energy velocity with the group velocity. Then a non-absorbing isotropic plate immersed in water is studied, revealing the departure of the energy velocity solutions from the group velocities. Finally an absorbing plate in vacuum is studied, again showing separate energy velocity and group velocity solutions. Experimental results for one of the modes in the absorbing plate are also shown, confirming that a wave packet does indeed travel at the predicted energy velocity.

5.2 Guided wave problem

We consider an infinite plane parallel absorbing plate of thickness 2h, density ρ_2, longitudinal velocity ${}^*C_{L2}$ and shear velocity ${}^*C_{T2}$ (where ${}^*C$ is defined in Eq. 2.12) immersed in a fluid whose density is ρ_1 and longitudinal bulk velocity is C_{L1}. The simpler examples of an absorbing (or not) plate in vacuum (or not) will easily be deduced from this general case by annulling the viscoelastic constants in the solid as well as the waves amplitude in the liquid for vacuum.

Starting from the linear system of equations, obtained by the continuity of the normal displacements and of the stresses on each interface, the characteristic equation is obtained by equating the determinant of this system to zero. The well known dispersion equation of the symmetric Lamb wave function is for example given by [27]:

$$Cs(\omega, {}^*k_x) = (\omega^2 - 2\,{}^*C_T^2\,{}^*k_x^2)^2 \cot({}^*ph) + 4\,{}^*C_T^4\,{}^*k_x^2\,{}^*p\,{}^*q \cot({}^*qh) + i\,{}^*\tau = 0 \qquad (5.1)$$

with

$$^*\tau = \frac{\rho_1 \, ^*p}{\rho_2 \, ^*m} \tag{5.2}$$

where all the quantities are defined in Eq. 3.8.

The dispersion equation of the anti-symmetric Lamb wave function is obtained by changing the cotangents into tangents and by taking $^*\tau = -\,^*\tau$.

Let us now consider the real part of the displacements in the plate at a given y_0 position given by Eq. (3.17), denoted by u_x and u_y. They can be expressed as follows

$$\begin{cases} u_x = f' \cos(\phi) - f'' \sin(\phi) \\ u_y = g' \cos(\phi) - g'' \sin(\phi) \end{cases} \tag{5.3}$$

where f' and g' stand for the real part of u_x and u_y respectively, f'' and g'' for their imaginary parts and ϕ for the common phase term $(\omega t - k_x^{'} x)$. The amplitude decay term $(e^{-k_x^{''}})$, being common to u_x and u_y, has voluntarily been omitted. After several manipulations of Eq. (5.3) it can be shown easily that any Lamb wave displacements describe an ellipse whose large axis is rotated by an angle ψ from the reference (O, x, y) to (O, x_1, y_1) as presented in Fig.5.1. In fact, the displacements of the four partial waves which constitute a Lamb wave, and their superposition to form the Lamb wave, are all elliptical.

Figure 5.1: Lamb wave displacement over a time period where y_0 describes the position over the thickness of the plate.

The angle of the axis of the ellipse is such that:

$$\tan(\psi) = \frac{g''}{f''} = -\frac{f'}{g'} \tag{5.4}$$

It is clear from this equation that for the general case when ${}^*k_x$ is complex, i.e., f', f'', g', g'' are not null, $\tan(\psi)$ is neither zero nor infinite. Moreover, the simple case of a non absorbing plate in vacuum ($\alpha_{L,T} = 0$, f''=0 and g'=0) is the only example for which ψ is always $\pi/2$. In that case the axes of the ellipse, for each different y position inside the plate, are collinear to the plate axes.

5.3 Non absorbing plate in vacuum

Here we consider the particular case of Lamb waves when there is no attenuation. This is included here to confirm the agreement of the group velocity and energy velocity in such cases, the simpler case of SH waves propagating in a non viscoelastic plate in vacuum being presented in Ref. [4].

Now, since $\alpha_{L,T} = 0$ and ${}^*\tau = 0$, the non standing but propagating solutions of the symmetric and anti-symmetric Lamb wave dispersion equations given by Eq. (5.1) are real (${}^*k_x = k_x$).

5.3.1 Group velocity

This is the velocity of a modulated wave which is constructed by taking two waves with slightly different values of ω and k_x [4]. The propagation velocity of the carrier is the phase velocity defined by:

$$V_\phi = \frac{\omega}{k_x} \tag{5.5}$$

and the propagation velocity of the envelope is the group velocity:

$$V_g = \frac{\partial \omega}{\partial k_x} \tag{5.6}$$

With this definition, any dispersion relation linking the frequency ω and the wavenumber k_x is suitable to calculate the group velocity. Thus the symmetric Lamb function given in Eq. (5.1) is considered and, as $dCs(\omega, k_x) = 0$, therefore the group velocity can be expressed as:

$$V_g = -\frac{\partial Cs(\omega, k_x)\,/\partial k_x}{\partial Cs(\omega, k_x)\,/\partial \omega} \tag{5.7}$$

Then, expanding this gives:

$$V_g = \frac{k_x c_L^2}{\omega}\left[\frac{A}{B}\right] \tag{5.8}$$

with:

$$\begin{aligned} A = &-8pqc_T^2(\omega^2 - 2c_T^2k_x^2)\cot(ph) - 4c_T^4[k_x^2(p^2+q^2) - 2p^2q^2]\cot(qh) \\ &+hq\left(\frac{(\omega^2-2c_T^2k_x^2)^2}{\sin^2(ph)} + \frac{4c_T^4k_x^2p^2}{\sin^2(qh)}\right) \end{aligned} \tag{5.9}$$

and

$$\begin{aligned} B = &-4pqc_L^2(\omega^2 - 2c_T^2k_x^2)\cot(ph) - 4c_T^4k_x^2(c_L^2p^2 + c_T^2q^2)\cot(qh) \\ &+hq\left(\frac{(\omega^2-2c_T^2k_x^2)^2}{\sin^2(ph)} + \frac{4c_T^2c_L^2k_x^2p^2}{\sin^2(qh)}\right) \end{aligned} \tag{5.10}$$

5.3.2 Energy velocity

The energy velocity vector is defined at a given y position in the plate by [4]:

$$\mathbf{V_e}(y) = \frac{\langle \mathbf{P} \rangle}{\langle E \rangle} \tag{5.11}$$

where $\langle(.)\rangle$ denotes the time average over one period:

$$\langle(.)\rangle = \frac{1}{T}\int_0^T (.)dt \tag{5.12}$$

and where $\mathbf{P}$ stands for the Poynting vector and E for the total energy in the system (potential and kinetic). Those quantities are real and defined as follows:

$$\mathbf{P} = -\overline{\overline{\sigma}}\dot{\mathbf{u}} \tag{5.13}$$

and

$$E = \frac{1}{2}\rho\dot{\mathbf{u}}\cdot\dot{\mathbf{u}} + \frac{1}{2}\lambda\theta^2 + \mu\overline{\overline{\varepsilon}} : \overline{\overline{\varepsilon}} \tag{5.14}$$

where $\dot{\mathbf{u}}$ is the particle velocity vector, λ and μ are the Lamé coefficients, $\overline{\overline{\sigma}}$ and $\overline{\overline{\varepsilon}}$ are the stress and the strain tensor respectively, and $\theta = \varepsilon_{11} + \varepsilon_{22} + \varepsilon_{33}$ is the dilatation. In the calculation of $\mathbf{P}$ and E all the different quantities have been calculated using the real part of the displacements given in Eq. (3.17).

However, as we are dealing with Lamb waves, that is waves confined within a plate, our interest is in the energy velocity flux in the whole plate. This requires additionally an integral through the thickness of the plate and is defined by [1]:

$$\tilde{\mathbf{V}}_{\mathbf{e}} = \frac{\langle\langle\mathbf{P}\rangle\rangle}{\langle\langle E\rangle\rangle} \tag{5.15}$$

where $\langle\langle(.)\rangle\rangle$ denotes an average over a time period as well as over the thickness of the plate:

$$\langle\langle(.)\rangle\rangle = \frac{1}{2h}\int_{-h}^{h}\langle(.)\rangle dy \tag{5.16}$$

After long and non trivial calculations, it is found that, when $V_\phi > c_L$ (that is p and q are purely real), the component of the Poynting vector at any location following the $\mathbf{y}$ direction is always null and the component of the flux in the whole plate following the $\mathbf{x}$ direction is:

$$\begin{aligned}\langle\langle P_x\rangle\rangle = \tfrac{\rho\omega^3 k_x \sin^2(qh)\sin^2(ph)}{q}\Big\{ &-4c_T^2p^2(\omega^3 - 3c_T^2q^2)\cot(qh) + \\ &\tfrac{p}{q}(\omega^2 - 2c_T^2q^2)(\omega^2 - 2c_T^2q^2 + 8c_T^2p^2)\cot(ph) + \\ &hq\left(\tfrac{(\omega^2-2c_T^2k_x^2)^2}{\sin^2(ph)} + \tfrac{4c_T^4k_x^2p^2}{\sin^2(qh)}\right)\Big\}\end{aligned} \tag{5.17}$$

Also:

$$\langle\langle E\rangle\rangle = \frac{\rho\omega^4\sin^2(qh)\sin^2(ph)}{qc_L^2}\Bigg\{ - \frac{4c_T^2p^2(\omega^3-c_T^2q^2)(\omega^2-3c_T^2q^2)}{(\omega^2-c_T^2q^2+c_T^2p^2)}\cot(qh)+$$

$$\frac{q(\omega^2-c_T^2q^2)(\omega^2-2c_T^2q^2)(\omega^2-c_T^2q^2+8c_T^2p^2)}{p(\omega^2-c_T^2q^2+c_T^2p^2)}\cot(ph)+ \tag{5.18}$$

$$hq\left(\frac{(\omega^2-2c_T^2k_x^2)^2}{\sin^2(ph)} + \frac{4c_T^2c_L^2k_x^2p^2}{\sin^2(qh)}\right)\Bigg\}$$

The energy velocity vector, expanded to its direction components, is thus:

$$\tilde{\mathbf{V}}_{\mathbf{e}} = \begin{pmatrix} V_e \\ 0 \end{pmatrix} \tag{5.19}$$

Making use again of the abbreviations A and B of Eq. (5.9) and (5.10), it is found that:

$$V_e = \frac{k_x c_L^2}{\omega B}\left(A + \frac{q}{p}Cs\right) \tag{5.20}$$

But by definition [Eq. (5.1)], $Cs = 0$, so by comparing Eq. (5.20) with Eq. (5.8), it follows that $V_e = V_g$.

The situations when $c_T < V_\phi < c_L$ and $V_\phi < c_T$ have of course been explored too. They also lead by the same process of analysis to the equality between energy and group velocities but for brevity they are not presented. The only alteration in the algebra is that hyperbolic functions appear in place of the trigonometric functions because p and/or q become purely imaginary. The same demonstration can be made for the anti-symmetric Lamb modes.

5.4 Non absorbing plate in a fluid

Let us now study the non absorbing plate immersed in a fluid for which the equality between the group velocity and the energy velocity is known not to hold true. In this configuration, solutions of symmetric and anti-symmetric Lamb functions are now complex, which means that the x-wave-number becomes a complex quantity. The imaginary part of the wave-number describes the attenuation of the guided wave due to leakage of energy by radiation into the fluid.

If a calculation of the group velocity is now attempted according to Eq. (5.6, 5.7), it becomes necessary to consider the complex wave-number, so Cs must be derived with

respect to $^*k_x$. This would be possible mathematically, but it no longer makes physical sense.

Consideration of the energy velocity calculation also leads to difficulty, in this case not by a physical constraint but by algebraic complication. The relations given by Eq. (5.17) and (5.18) would now have to contain complex wave-numbers (neither purely real nor purely imaginary), and so would be a linear combination of trigonometric and hyperbolic functions. It was decided realistically therefore that an analytical result for the energy velocity vectors was unworkable, and so numerical computations were undertaken instead.

Figure 5.2 shows some computed dispersion curves for a 1 mm thick aluminium plate, in vacuum (dotted lines) or immersed in water (solid lines). Part (a) shows the phase velocity, indicating very little difference between the curves for the vacuum case and the immersed case. Part (b) shows the attenuation of the immersed case, expressed in Nepers/m; of course the attenuation of the vacuum case is zero. The properties of the materials are: $c_L = 6.37\ m/ms$, $c_T = 3.1\ m/ms$, $\rho = 2.8\ g/cm^3$ for the aluminium and $c_L = 1.5\ m/ms$, $\rho = 1\ g/cm^3$ for the water.

An obvious difference between the vacuum and immersion cases is with the mode S_1. In the immersion case this mode exhibits a cut-off in phase velocity which has already been examined by Lenoir, Duclos et al. [37] for example. This behaviour is accompanied by an increase of attenuation up to 4000 Np/m as the frequency tends to zero (for clarity, not shown in part (b) of Fig. 5.2. This very high attenuation reduces the phase velocity of S_1 instead of its rise to infinity as for a plate in vacuum. Such cut-offs are also observed if the problem is solved not in real frequency and complex slowness but in complex frequency and real slowness [24, 69]. In that case, again, the imaginary part of the frequency tends to infinity and cut-offs in frequency instead of phase velocity appear for the modes commonly labelled A_0 and S_0, confirming the idea that the high attenuation leads to cut-off either in frequency or in phase velocity. We will consider now some more detailed results for this mode, with the aim of studying the influence of the fluid loading.

5.4.1 Energy velocity vectors comparison

Since we know that the imaginary part of the wave-number indicates the leakage of energy into the fluid, we should expect the energy velocity vectors to show some component in the direction normal to the plate. This is of course in contrast with the plate in vacuum for which it was shown earlier that the component in the normal direction is zero. We have calculated the energy velocity vectors at four different frequencies (10, 8, 6, 4 MHz), marked by filled circles in Fig. 5.2. The vectors, defined by Eq. (5.11), are shown over a range of different y positions in Fig. 5.3. The plots on the left hand side of the figure are for the aluminium plate in vacuum and on the right hand side for the aluminium plate immersed in water. In the vertical direction each plot represents one of the four chosen

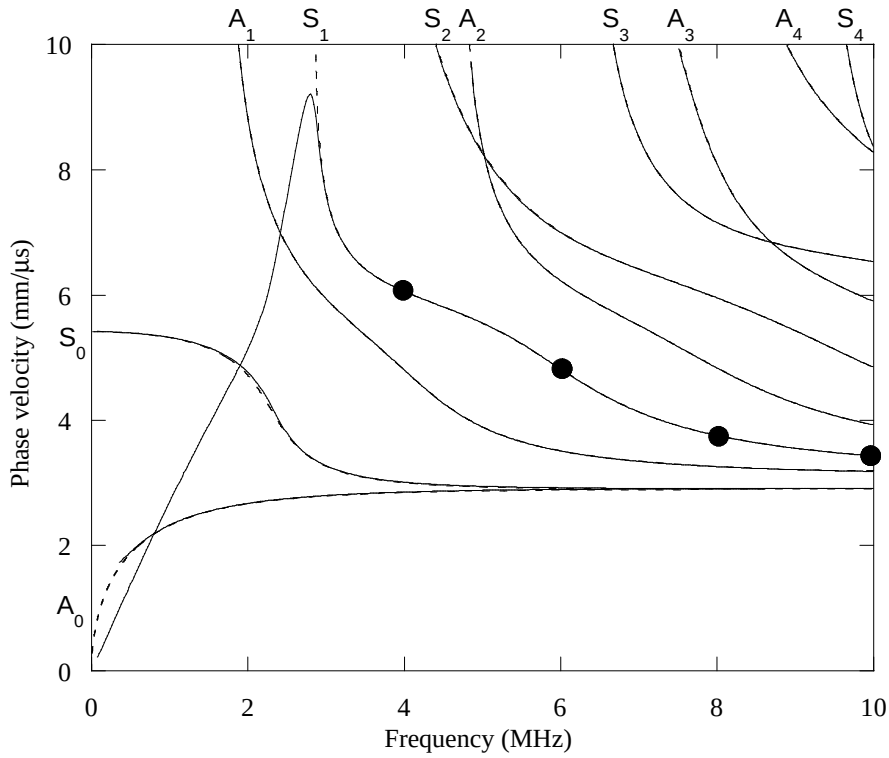

(a)

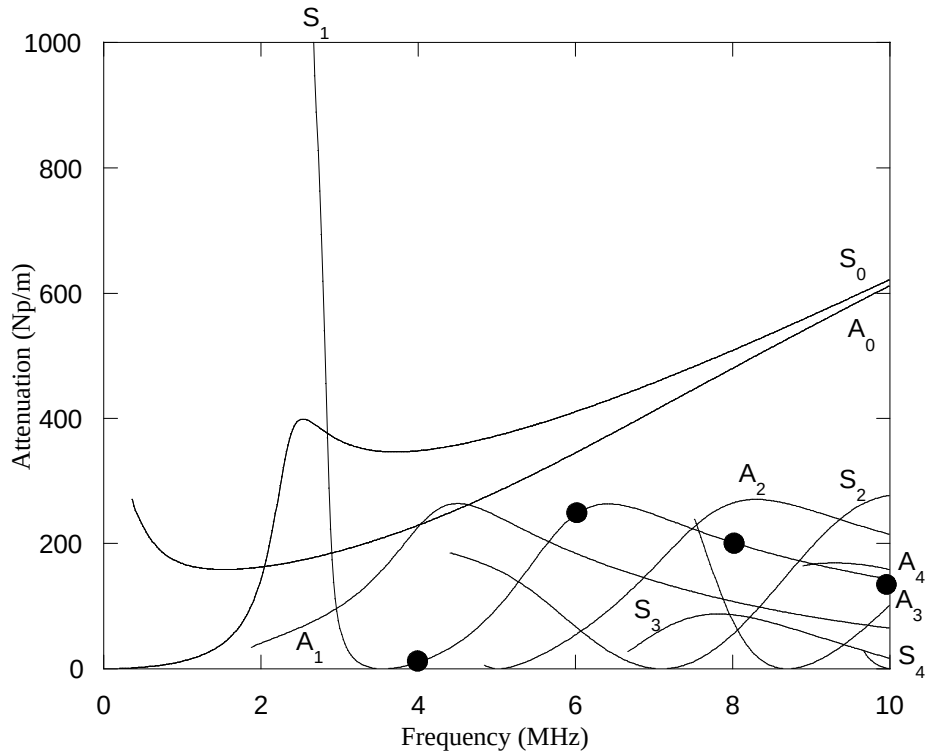

(b)

Figure 5.2: Dispersion curves comparison between a 1 mm thick aluminum plate in vacuum (- - -) and in water (—). Part a) Phase velocity ($\omega/k_x^{'}$) and part b) attenuation ($k_x^{''}$ for the leaky case) both versus the frequency. Black circles show the different positions for the calculation of the energy velocity vectors presented in Fig. 5.3

locations on the dispersion curve. In each plot the top and bottom of the plate are identified by dotted lines and the energy velocity vectors are shown as solid lines. The vectors have directions and lengths according to their actual directions and amplitudes. The amplitude scale is arbitrarily normalised to the maximum in each plot.

Let us first consider the left column of Fig. 5.3. As explained in section 5.3, the solutions of Lamb wave functions being real for the case in vacuum, the energy velocity vectors only have a component along the **x** direction : $\langle\langle P_y \rangle\rangle$ is always null. However, regardless of the direction of the global propagation of energy along the plate, it is permissible according to the derivation that locally an individual vector may lie in either the positive or the negative **x** direction. It is interesting to see that in fact vectors with negative **x** directions are actually predicted at the 4 MHz and 6 MHz locations when clearly the global energy direction is positive. There are also circumstances when the global energy propagation, that is the sum of these vectors, is in the negative direction. For example this occurs for the S1 mode when the phase velocity is greater than 11.44 mm/ms in the so-called backward propagating or negative group velocity region. For example this has experimentally been measured by Wolf, Ngoc et al. [80]. The energy velocity vectors for one position on the curve in this case are presented in Fig. 5.4.

This raises the interesting observation that energy can travel in the negative direction even though the mode is modelled by the superposition of four partial plane waves (two longitudinal and two shear) whose wavenumber projections on the **x** direction are positive. Clearly it is necessary to be very careful when dealing with the energy in waves, and issues of the superposition of waves. Lamb waves exist because of constructive or destructive interference between those partial waves. Therefore, what is seen is a consequence of those interferences but does not express the exact contribution of each phenomenon. In fact, we acknowledge that this is not really understood yet.

In contrast, the leaky case generally exhibits energy velocity components on the **y**-direction. It is important to note that, in this second example, the orientations of the energy velocity vectors are a consequence of the nature of k_x which has become a complex quantity. As for the elliptical displacements presented in section 5.2, an angle of rotation function of the y position in the plate is observable and the energy seems to move towards the fluid. However, there is no evidence that these angles correspond to the ellipse angles. The global shape of the energy velocity vectors has been conserved and as in vacuum some components are oriented toward the negative **x** direction. We also see that the extent to which the vectors point in the **y** direction corresponds broadly to the strength of the leakage. For example, at 4 MHz, the attenuation (the imaginary part of $^*k_x$), is almost null, and correspondingly the components of the energy velocity vectors along the **y** axis are rather insignificant compared to the components along the **x** axis, and the vectors in general closely resemble those for the plate in vacuum.

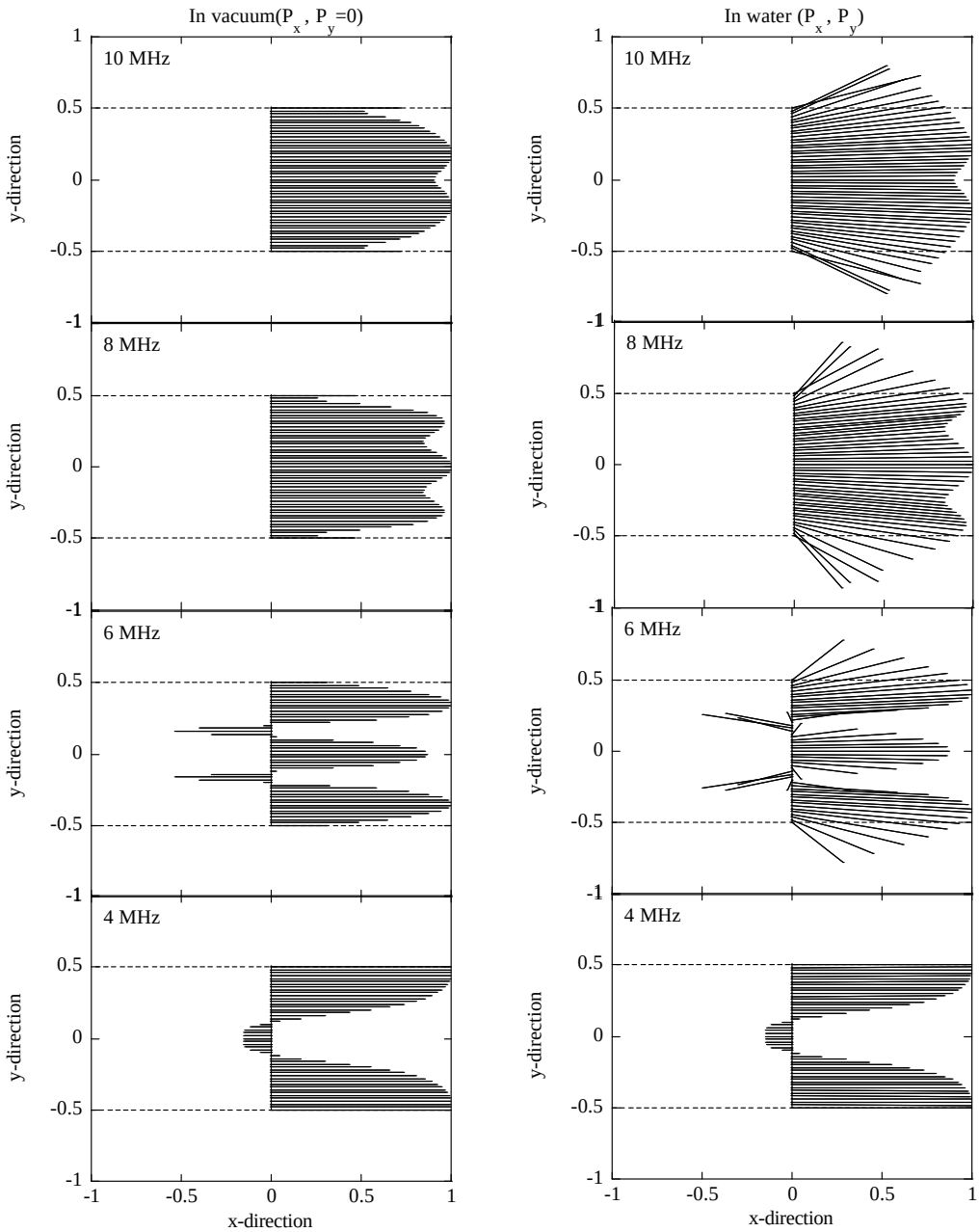

Figure 5.3: Local energy velocity vectors comparison between the aluminum plate in vacuum (left) and in water (right) calculated at different y-position for different frequencies labeled • in Fig.5.2.

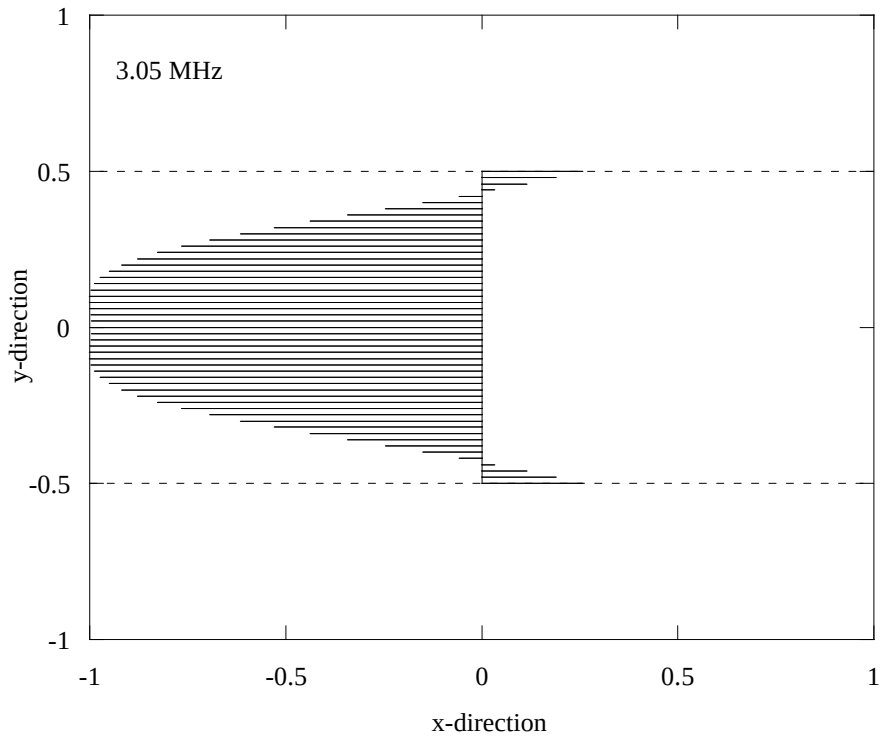

Figure 5.4: Local energy velocity vectors for the mode S_1 corresponding to a negative group velocity and to a negative global energy velocity.

5.4.2 Energy velocity and group velocity comparison

The energy velocity concept instead of the group velocity has been studied because of the discontinuities and the unacceptable values obtained when calculating the group velocity of attenuative guided waves. One simple, but obviously approximate, approach in such cases is to use the definition: $V_g = \frac{\partial \omega}{\partial Re(^* k_x)}$. This expression is of course correct in the limit of reducing attenuation. Fig. 5.5(a) shows the predicted group velocity for the S1 mode for the aluminium plate immersed in water, made using this expression. The discontinuities which arise at around 3 MHz down to 0 MHz correspond to the location on Fig. 5.2 where the phase velocity is decreasing back to zero, a region of the curve where the attenuation is extremely large. They are in fact due to infinite slopes when representing the solutions on a graph of frequency versus real wave-number, these slopes being a genuine feature of this curve.

Fig. 5.5(b) shows the energy velocity prediction calculated numerically using Eq. (5.15). It shows that the energy velocity and the group velocity are in good agreement in the region where the attenuation is low but not where the attenuation is high. In the high attenuation region the energy velocity curve is smooth and does not present any unacceptable values such as excursions above the longitudinal bulk velocity of the material. We can also observe that it converges towards zero as the frequency decreases and the attenuation

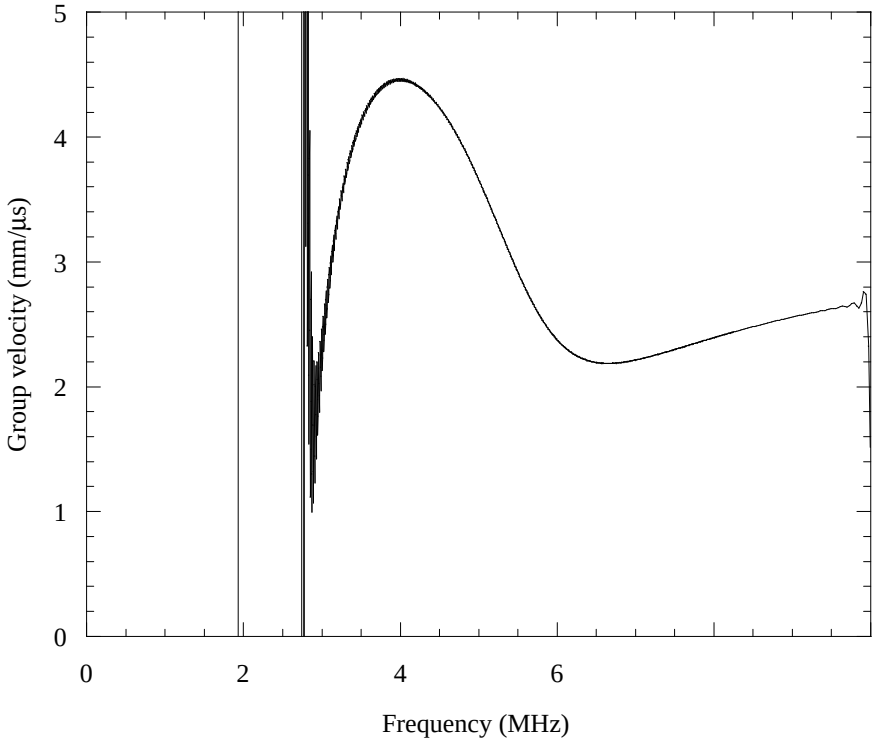

(a)

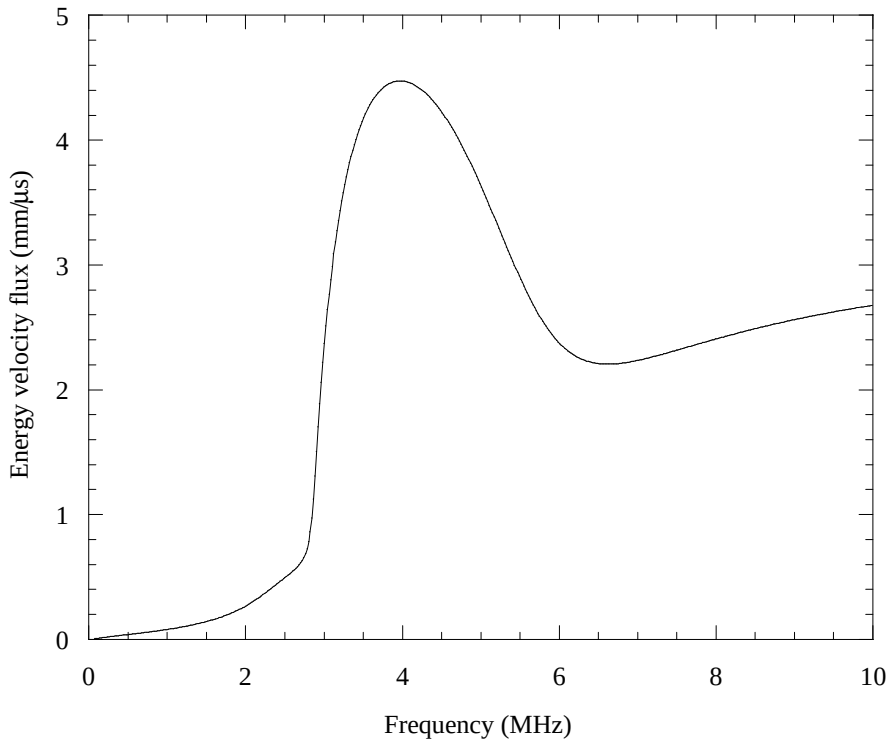

(b)

Figure 5.5: (a) Group velocity for S_1, (b) Modulus of the energy velocity flux $\tilde{\mathbf{V}}_{\mathbf{e}}$ for S_1.

increases.

5.5 Absorbing plate in vacuum

We now consider another attenuative system, but in this case the attenuation is due to material damping rather than leakage. The system is a 12.7mm thick plastic plate in vacuum. The plastic is a High Performance PolyEthylene (HPPE). This particular material was chosen because it has been fully studied by Chan [14, 15] who measured the following properties: $c_L = 2.344\ mm/ms$, $\alpha_L = 0.055\ Np/wl$, $c_T = 0.953\ mm/ms$, $\alpha_T = 0.286\ Np/wl$, $\rho = 953\ kg/m^3$. His dispersion curves, some of which are reproduced here in Fig. 5.6, were calculated using a general purpose model developed by Lowe [42] and Pavlakovic, Lowe et al. [59].

5.5.1 Theoretical curves

The modes, shown in Fig. 5.6, are divided into two categories. The first, called shear modes, have phase velocities which tend towards the shear bulk velocity of HPPE at high frequency (solid lines) and the second, called longitudinal modes, have phase velocities which tends towards the longitudinal bulk velocity of HPPE (dotted lines). It is interesting to see in this example too that cut-offs in phase velocity occur, in this case for nearly all of the modes. Again these correspond to locations where the attenuation is very large (for clarity, not shown in Figure 6(b)). The modes which have a lower attenuation correspond in fact to the longitudinal modes, all of the shear modes having an attenuation higher than that of S_0 and A_0 (oblique lower line in Fig. 5.6(b)).

5.5.2 Energy velocity vectors comparison

In this section we calculate the local energy velocity vectors $\mathbf{V_e}(y)$ at different depths through the thickness of the HPPE plate and compare them with the hypothetical vectors for the same plate if the damping was not present. This should be a fundamentally different study than was performed earlier for the immersed plate because in the present case the energy is lost within the plate and there can be no radiation from the surfaces of the plate.

The mode chosen to do the comparison is S_3. This mode, which has been studied in detail by Chan [15], has relatively low attenuation and so was identified as being the most amenable for practical work. We will present some experimental results using it in section 5.6. Fig. 5.7 shows a comparison between the dispersion curve of S_3 in HPPE (solid line) and some of the modes for the same plate but without any material damping (dotted lines). As explained by Chan, when material damping is absent plateauing regions

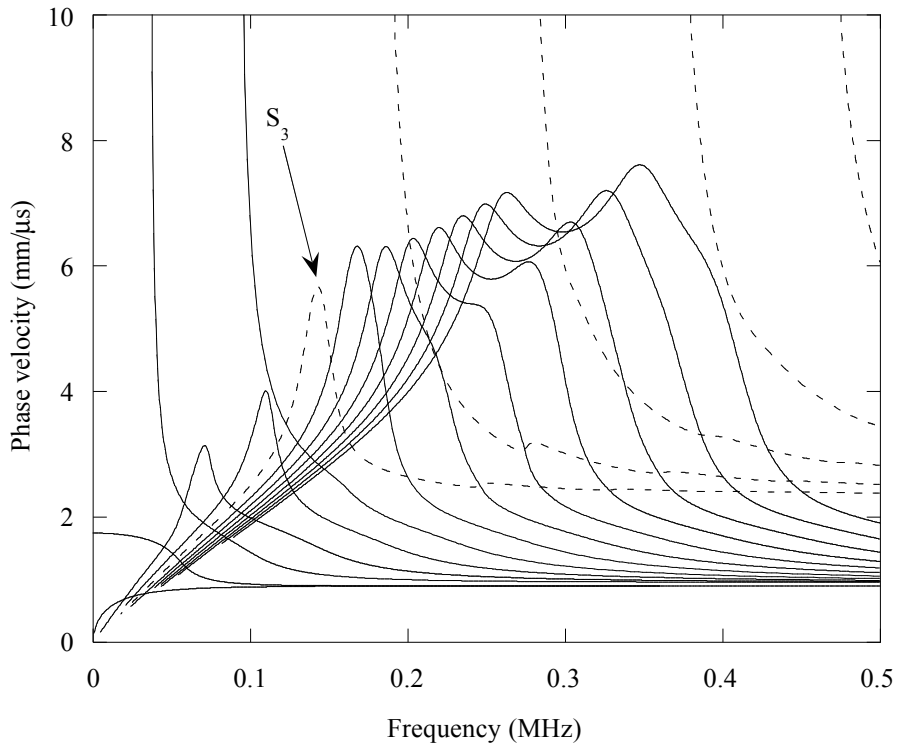

(a)

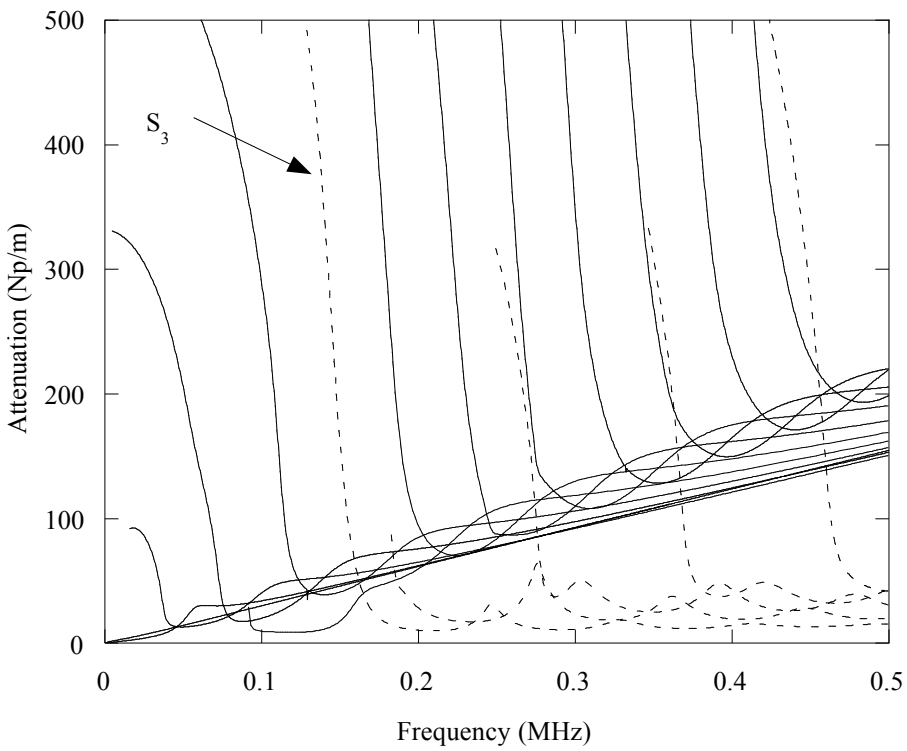

(b)

Figure 5.6: Dispersion curves for a 12.7-mm thick HPPE plate in vacuum [14, 15]. Part a) shows the phase velocity and part b) shows the attenuation both versus the frequency.

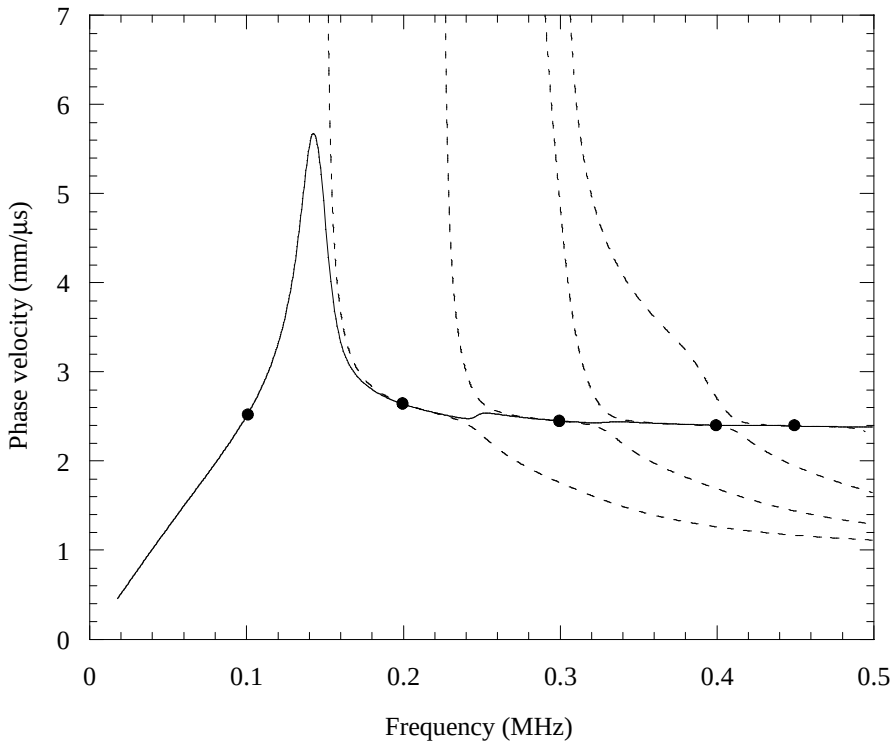

Figure 5.7: Comparison between S_3 dispersion curve (solid line) in HPPE plate and dispersion curves for same plate without material damping (dotted lines).

exist. By joining these regions together, it is possible to visualise a new set of dispersion curves which tend towards the longitudinal bulk velocity of HPPE and these represent the curves when the damping is included. In fact, S_3, like all the other longitudinal modes, can be understood to be a result of these regroupings between several different modes, in this case the four dotted curves in the figure.

Energy vector plots for 5 locations on the dispersion curves are shown in Fig. 5.8. The locations are identified by filled circles in Fig. 5.7. The arrangement for the plot follows that which was explained in the earlier comparison in section 5.4.1. The left hand side shows the vector plots for the HPPE without material damping and the right hand side shows them for the HPPE with material damping. At 0.1 MHz there is no equivalent mode in the undamped case and so no plot can be shown on the left hand side for this frequency. Although the mode S3 results from an association of four different modes, the comparison between the energy velocity vectors for the two configurations looks close, with the exception perhaps at 0.4 MHz where some of the energy has negative components for the HPPE without material damping but not for the HPPE with material damping. However, the most interesting feature of this study is evident at 0.1 MHz. Here, where the attenuation is relatively large, it can be seen that some of the vectors have components in the **y** direction, despite the fact that the plate is in vacuum and there is no leakage. But the vectors at the surfaces of the plate are parallel to the **x**-direction and so there is only

internal transfer of energy. Closer examination at other frequencies shows that non-zero y components exist also at higher frequencies but are very small.

5.6 Experiments

Finally, we present some results from an experimental study which was performed in order to validate the energy velocity calculations. There is a fundamental difficulty in designing a suitable experiment because the energy velocity and the group velocity differ significantly only when the attenuation is relatively large, in which case the waves decay rapidly as they propagate. The S_3 mode in the HPPE plate presents an interesting possibility because there are some locations where the group velocity rises while the energy velocity falls, yet the attenuation is generally not excessive. Fig. 5.9 shows the predicted group and global (using integral expression presented in Eq. 5.15) energy velocities of the S3 mode in solid and dotted lines respectively; Fig. 5.10 shows the phase velocity. The sharp rise of the group velocity at 0.25 MHz is typical of the singularity associated with an infinite slope of the wave-number, as discussed earlier. The regions where the group and energy velocities differ most are also, as expected, the regions where the attenuation is highest.

The experiments were conducted using two wide band contact transducers (Panametrics), one at each end of a HPPE plate, in a through-transmission arrangement. The transducers were clamped to the ends of the plate with their axes aligned with the centre line of the plate. Extensional motion of the faces of the transducers thus coupled directly with the in-plane extensional motion of the S3 mode. A narrow band signal consisting of 50 cycles at a chosen frequency in a Hanning window was applied to the emitter, using a Wavemaker Duet (Macro Design Ltd) signal generator. The received signal was captured on a digital oscilloscope (LeCroy 9400), 300 averages taken, and stored on a PC. The measurement was repeated for a range of frequencies and for two different lengths of plate.

The global energy velocity and the phase velocity were calculated separately at each test frequency. The energy velocity was calculated by overlaying the envelopes of the received wave packets for the two different lengths of plate, and measuring the difference between their arrival times. Of course this was only possible when the shape of the wave packet remained consistent so that an accurate overlay was possible. The signal was sufficiently narrow band that in fact the envelope retained a reasonable shape at most frequencies, but there remain some gaps in the results, principally at the locations where the attenuation was high and the signals were correspondingly weak and distorted. The phase velocity was calculated in a similar manner, but comparing instead the arrival times of the wave cycles within the envelope. This required particular care in order to ensure that the correct wave cycle was compared; several additional measurements using intermediate propagation distances were used to confirm this.

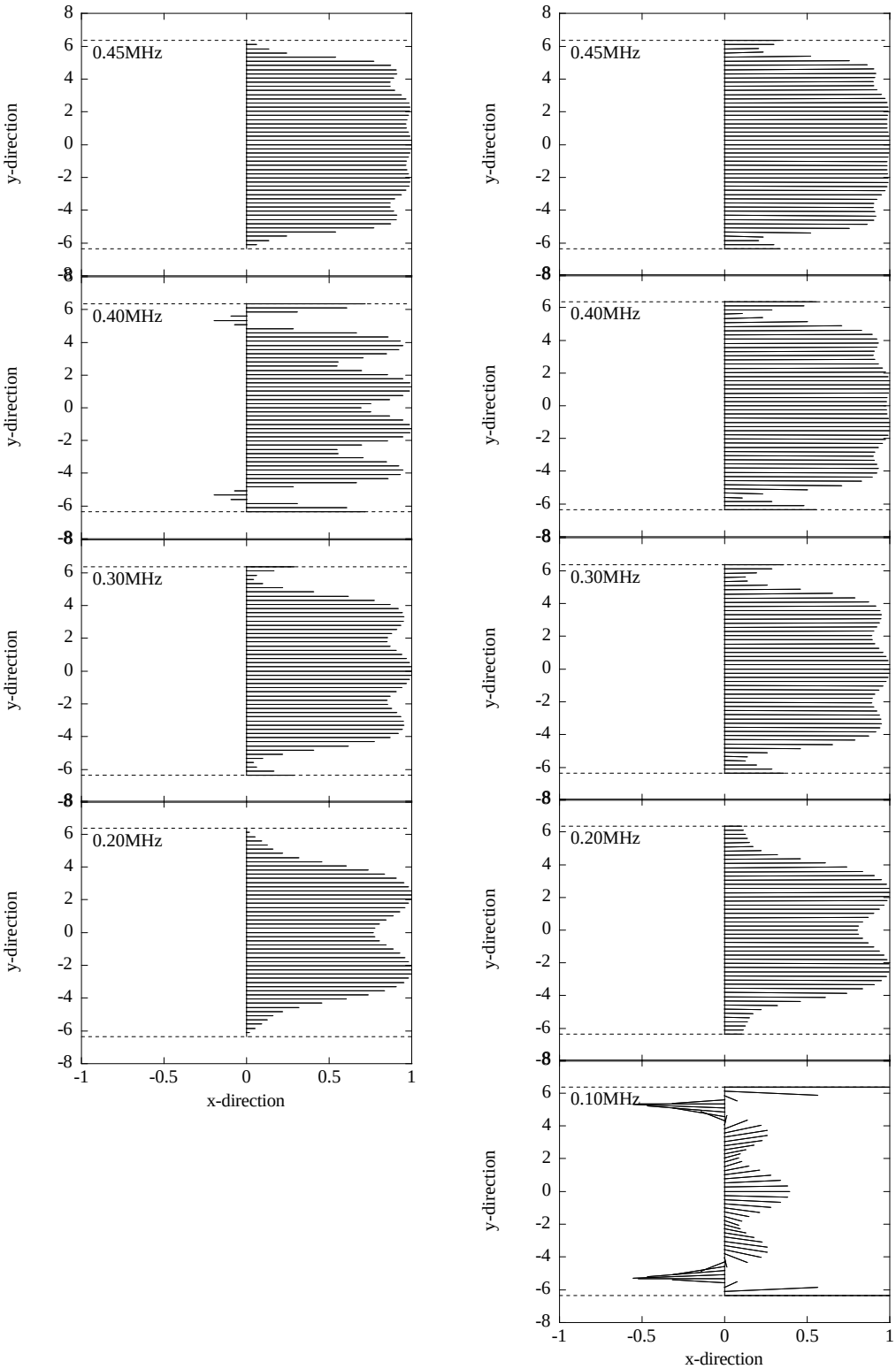

Figure 5.8: Energy velocity vectors comparison between HPPE plate without material damping (left) and with material damping (right) calculated at different **y**-positions.

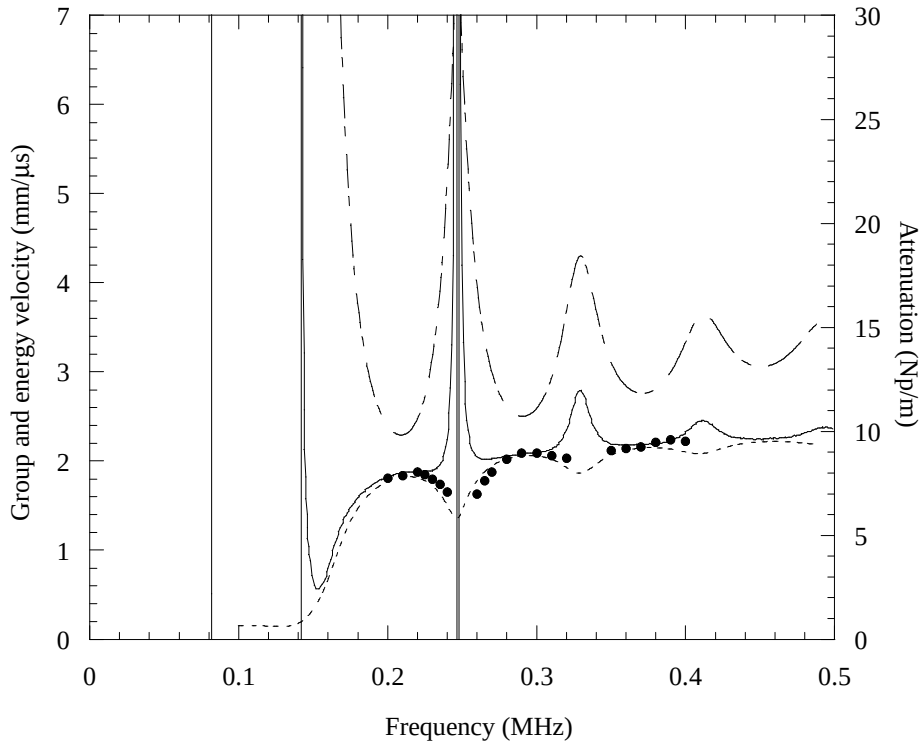

Figure 5.9: Comparison between group velocity (solid line), global energy velocity (dotted line (- - -))and experimental measurements (•) for the mode S_3. The attenuation is represented with a dashed line(— - —).

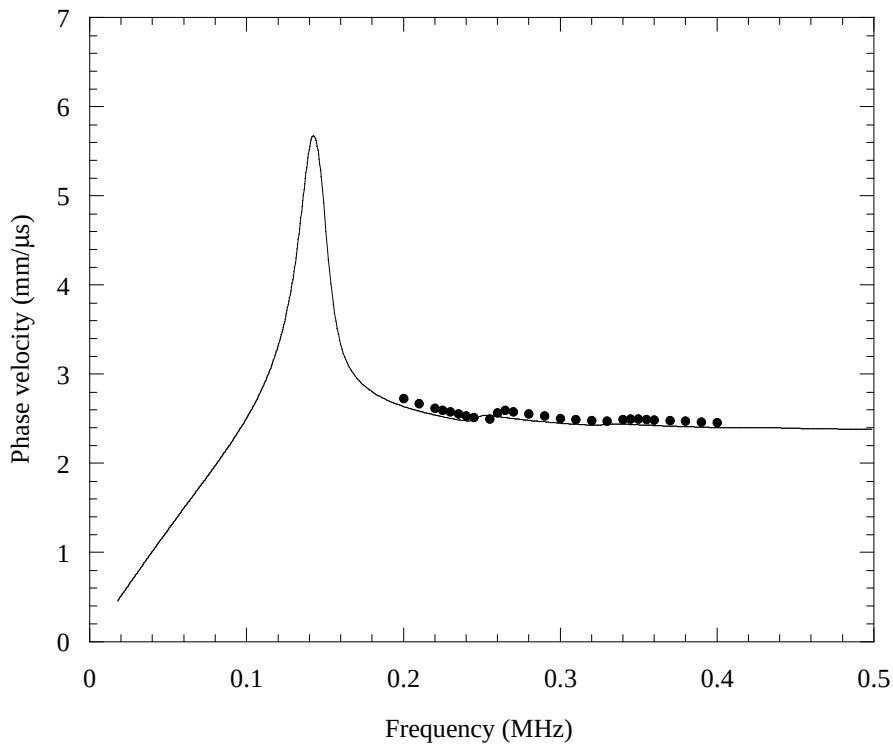

Figure 5.10: Comparison between the phase velocity (—) and experimental measurements (•) for the mode S_3.

The results are shown by filled circles in Fig. 5.9 and 5.10. The experimental measurements can be seen to agree very well with the global energy velocity prediction. The good agreement between experiment and prediction of the phase velocities, in Fig. 5.10, serves also to confirm that the measurements of the S_3 mode were obtained correctly.

5.7 Conclusions

The energy velocity of guided waves in flat plates has been calculated from the Poynting vector functions. In the case of the lossless Lamb modes in a vacuum-bounded non-absorbing plate, the energy velocity integral has been shown analytically to equate to the group velocity. In the cases of a non-absorbing plate immersed in water and of an absorbing plate in vacuum it has been shown numerically that the energy velocity can differ substantially from the group velocity, especially at locations on the dispersion curves where the attenuation is high. In such cases the group velocity can show discontinuities and unbelievably high values, but such features are not evident with the energy velocity. An experimental study of the S_3 mode in an absorbing plate has demonstrated good agreement of the velocity of a wave packet with the predicted energy velocity at such locations where there is divergence from the group velocity. The energy velocity should therefore be preferred as the correct measure of velocity when predicting the propagation of wave packets of attenuative modes. However, the group velocity is very much quicker to calculate and is likely to be acceptably accurate unless the attenuation is strong.

The Poynting vectors within the plate have also been plotted for these cases and demonstrate some interesting phenomena. In the lossless plate the vectors never have components in the direction normal to the direction of propagation; however the vectors in some locations in the plate can sometimes point in the opposite direction to the those at other locations. In the immersed plate the vectors give clear evidence of the leakage of energy into the fluid, while in the absorbing plate the vectors indicate transfers of energy across parts of the plate but of course not across the surface boundaries.

Still in the context of harmonic attenuated guided waves, if energy velocity or group velocity are important concepts in order to describe mode properties, it is of key importance to know how those modes can be excited. Usual immersed plate approaches try to match the frequency as well as the slowness of the mode. However, in such configurations, modes are characterized by a third parameter, which is described by its attenuation: modes leak energy into the water as they propagate along the plate. In the next chapter we experimentally study the excitation of modes with a source that takes into account the exponential decrease of the mode and we compare the results with a source which does not.

Chapter 6

Lamb waves excitation with IDTs

As explained in the previous chapters, guided waves can be used to test very large structures that can be monitored by transducers at only one or two fixed locations. The problems of course arise when the geometry of the structure is complicated and when the experimental setup needs to be properly adapted each time. For example, it is very troublesome to arrange water immersion coupling for a structure like an aircraft wing. Thus, if transducers are permanently attached or even integrated to the structure, then with the appropriate telemetry and information processing, continuous monitoring of the structure becomes possible. This research field concerning "smart material" has already received a lot of considerations. For example, P. Wilcox *et al.* studied Lamb wave inspection of large structures using Inter-Digital Transducers (IDTs) [79] which are low profile and can be designed to have a minimal impact on both the appearance and mechanical performance of the structure to which they are attached. The aim of this chapter is not to present the whole theory concerning the modelling of IDTs, which can be found in Ref. [78], but just to recall the most important features of these transducers and to look at some experimental results which have been obtained conjointly within the laboratory while these transducers were under investigation.

The challenge in developing a smart structure based inspection system was to design permanently attached sensors which would send a particular Lamb mode or modes along the structure in controlled directions and to receive the resulting signals at the same transducer and/or other receivers. Single mode generation can be achieved by carefully controlling the frequency and wavenumber bandwidth of the excitation. The frequency bandwidth can readily be limited by employing windowed tone burst excitation signals [3] while the wavenumber bandwidth is controlled by the transducer geometry. The most commonly used transducers for the excitation and the reception of Lamb waves are angled piezoelectric transducers in which the wavenumber bandwidth is determined by the size of the transducer and its angle to the structure surface [3]. As these standard transducers are bulky and are unlikely to be suitable for incorporation into a structure, an alternative is to deposit an "interdigital" electrode pattern on a piezoelectric substrate, the spacing between

the electrodes being appropriate for the excitation of the desired mode in the substrate. This was then achieved with piezoelectric polymer films such as PVDF (polyvinylidene fluoride) which are relatively cheap and very flexible allowing a permanent attachment even on curved structures. Interdigital transducers are described in details in Ref. [52]. They in fact consist of a layer of PVDF bonded to the structure under test. A flexible printed circuit board (PCB) is bonded on the top of the PVDF, copper side down, the PVDF being excited by a voltage difference between the PCB and the structure. The PCB is printed with two interleaved sets of comb shaped electrodes. The finger spacing of the combs defines the wavelength of the transducer and the individual finger widths are used to provide a spatial window effect (Hanning, square, ...) over the region on which the transducer is bonded (see bottom of Fig. 6.1).

As explained in the previous chapters, guided waves can attenuate either in time $({}^*\omega, S)$ or in space $(\omega, {}^*S)$. In this chapter we focus our attention on harmonic attenuated guided waves with real frequency and complex slowness. It is well known that in vacuum, guided mode excitation can be achieved by controlling the frequency and the wavenumber (or slowness). However, as long as the plate is immersed in water, the slowness becomes a complex quantity. In this case, chapter 4 showed that guided waves could also be excited if the frequency and the angle of incidence (or real part of the slowness) match the dispersion curves. However, modes are now characterized by three parameters which are the frequency, the real part of the slowness (S') and the imaginary part of the slowness (S''). Although mode attenuation (or S'') is important in order to know if guided waves can propagate over a long distance, the aim of this chapter is then to look at S'' as a potential parameter for the excitation or the selection of a specific mode. In order to do so, the next sections describe two different experiments using an interdigital transducer, whose fingers are all disconnected from each other in order to be able to match S'', bonded on an aluminium plate.

As a preliminary approach, the plate is studied in vacuum. The aim is to check that the interdigital transducer has been properly both designed and bonded to the plate in order to excite A_0 in a region where this mode is not dispersive. The fingers being all independent, this approach also allows us to quantitatively analyse separately each finger pair behaviour. Then, the plate is immersed in a water tank. Although the frequency spectrum can be reduced with a large number of cycles, the wavenumber spectrum regarding the number of connected finger pairs is studied. Finally, a specific mode is excited with two different types of input. The first input consists of a square input where all the fingers are excited with the same amount of energy (ω and S' only are taken into account). This model is the most commonly used because the fingers are usually all interconnected. Secondly, the mode is excited with an exponentially decreasing spatial source corresponding to its spatial predicted attenuation (ω, S' and S'' are taken into account). The amplitude of the received signal in the two configurations is then discussed.

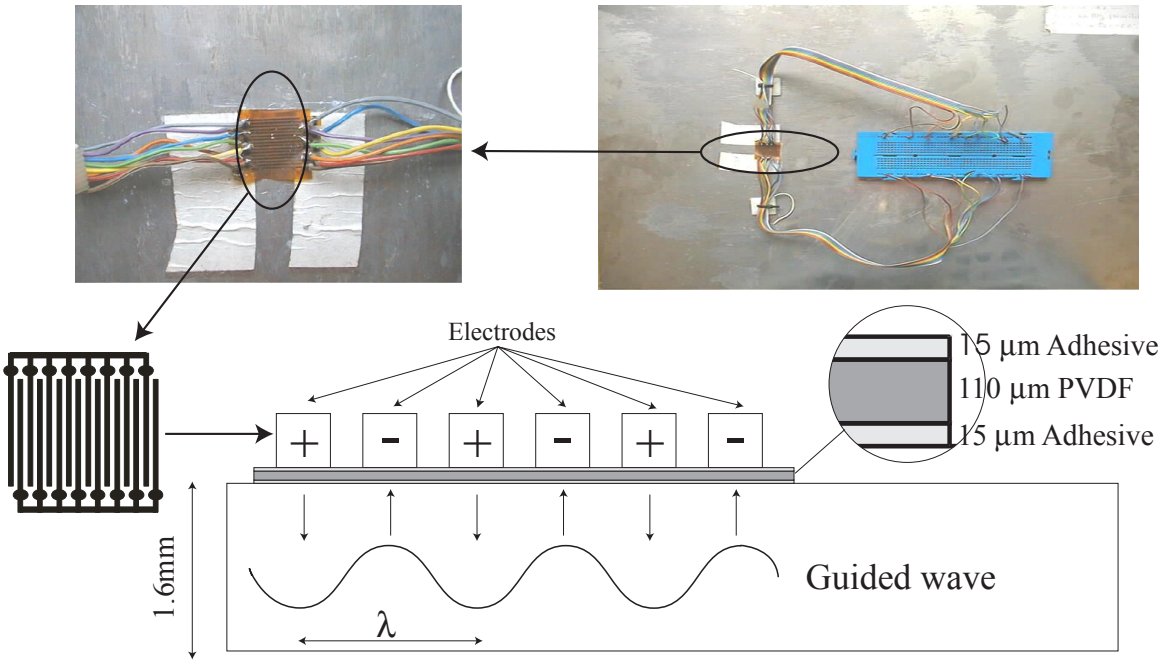

Figure 6.1: Schematic diagram showing a typical ITD bonded to plate.

6.1 Plate in vacuum

In this experiment, all the fingers are disconnected. A thin wire being soldered on each finger allows us to connect or disconnect any finger or finger pair from a prototype board directly connected to the generator. As a consequence, the electric signal can go through one, a pair or all the fingers at the same time. As the aim is to finally create an exponential decrease in space, to experimentally take into account the attenuation of the mode, by changing the amount of electric energy in the fingers, we then first want to study each finger pair separately in order to know how they behave. Moreover, it is important to make sure that our transducer is well designed to excite A_0.

The plate is a 1.6-mm thick aluminium plate whose longitudinal and shear bulk velocities respectively correspond to: $c_L = 6.487\ m/ms$ and $c_T = 3.076\ m/ms$. The density was assumed to be 2.7 g/cm^3 as usual for aluminium and the velocities were measured using longitudinal and shear contact transducers. The plate and the IDTs are shown in Fig. 6.1 and 6.2. The fingers are periodically excited by positive and negative charges (mechanically equivalent to normal forces) resulting in the excitation of a guided wave within the plate whose wavelength is determined by the spacing between the fingers ($1.87 \pm 0.3\ mm$ here). It is to be noted that the fingers can also be apodised [52] or even radial [79]. However, in our case the fingers are identical size and all independent. The experimental setup when the plate is in vacuum is shown in Fig. 6.2. The different pairs of fingers are labelled with the following letters also corresponding their respective colors: R (red), O (orange), Y (yellow), G (green), B (blue), P (purple), Gr (grey). Moreover, as a convention, the grey

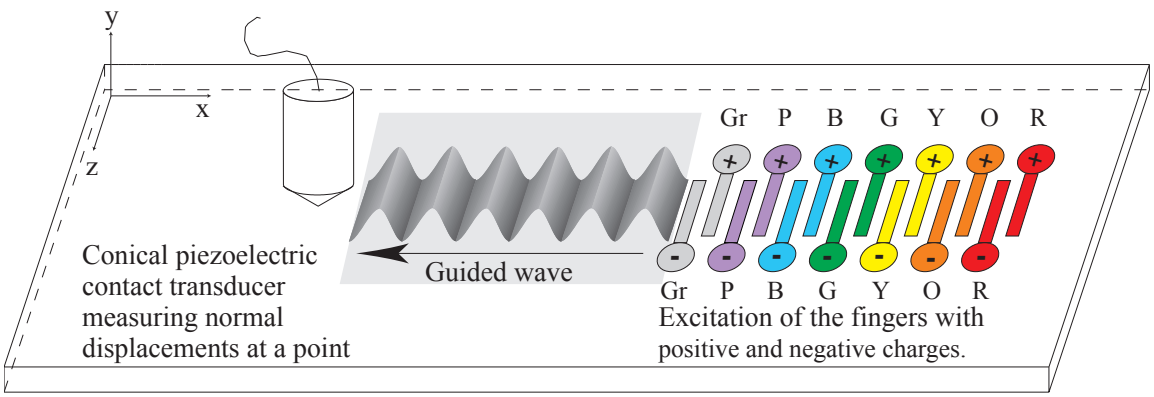

Figure 6.2: Experimental setup for the aluminium plate in vacuum.

pair will always be the nearest from the receiver and the red pair the furthest.

The phase velocity dispersion curves for the 1.6-mm thick aluminium plate in vacuum are shown in part a) of Fig 6.3 and part b) shows the corresponding group velocity. The oblique middle line in part a) shows the constant wavelength at which the IDT has been designed ($\lambda = 1.87\ mm$) and the two others refer to wavelengths with an error of $\pm 0.3\ mm$. For a central frequency of 1.265 MHz with a 20 cycles tone burst modified by a Hanning window, the mode which is most likely to be excited is A_0 (dark grey zone in the figure). At this frequency, the mode is non dispersive and then the shape of the signal should not be distorted after a propagation over a long distance.

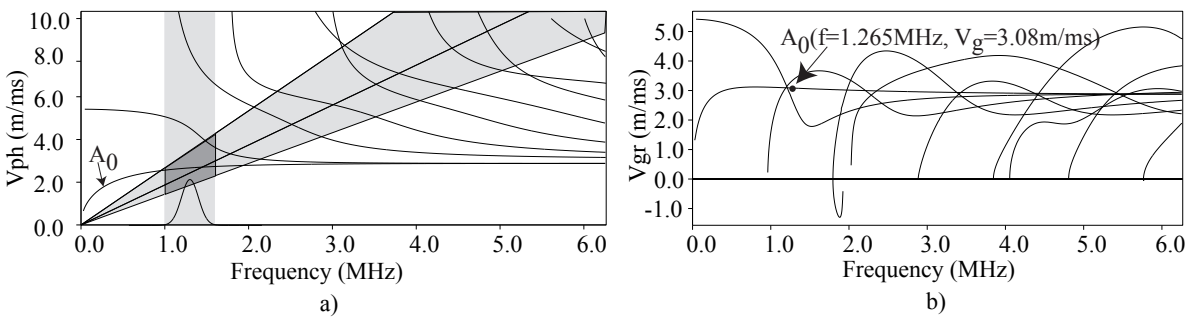

Figure 6.3: Dispersion curves for a 1.6-mm thick aluminium plate in vacuum. Part a) shows phase velocity and part b) shows group velocity, both plotted versus frequency.

For a given electric voltage on the Wavemaker Duet (Macro Design Ltd) signal generator, we look at the signals 70 cm away from the grey pair of electrodes. The receiver is a conical piezoelectric transducer working as a point receiver and designed in Imperial College [25]. The position of the receiver being fixed, each pair of electrodes was excited one by one and the received signals were captured on a digital oscilloscope (Lecroy 9400), 10 averages taken and stored on a PC. The results are shown in Fig. 6.4. The left and the right hand sides of the figure show the received signals coming from each pair of electrodes while the signals in the bottom part show, on the left, the received signal when all the fingers are connected, and on the right, the superposition of the signals of each pair of

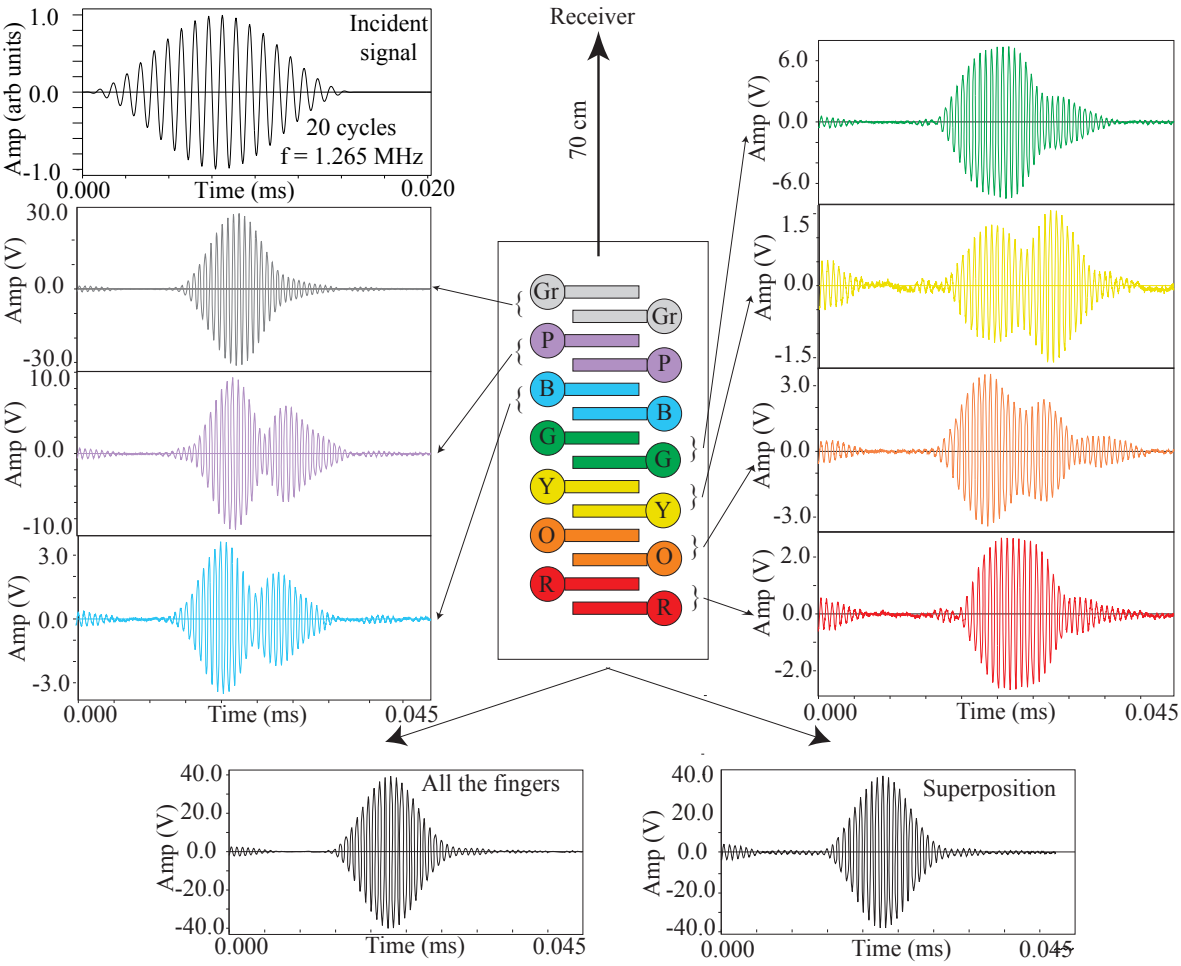

Figure 6.4: Received signals after a propagation of 70 cm along the aluminium plate. Left and right hand side show signals for individual pair, bottom shows the superposition of all those signals as well as the signal obtained when all the fingers are connected.

fingers. As a first conclusion, it is obvious that the signal, obtained with the superposition principle, and the signal, received when all the fingers are connected at the same time, are identical. As a consequence, the experimentation with a spatial exponential decrease of the electric energy within the fingers is possible. However, as a second conclusion, it is noteworthy that although multi-reflections occur between the different fingers, inducing a loss of amplitude in the received signal (also due to the adhesive), this loss is not geometrical! For example, the green pair of electrodes (G) has a voltage up to 6V when the blue (B), which is nearer from the receiver, has a voltage up to 3V. The wave excited by the blue pair (B) has a smaller distance to travel within the adhesive than the green (G) and the voltage should therefore have been higher. The same phenomenon also occurs for the yellow pair (Y) for example. These differences can be explained in two manners. First, the adhesive thickness which is under each finger pair may not be the same, resulting in a higher amplitude loss. Moreover, we also have to take into account that a finger or even a finger pair can be very badly bonded to the plate resulting in a very weak coupling and then again in an amplitude loss. Finally, the wave packet arrives after a propagation of

70 cm at a time $t \simeq 0.0228\ ms$. Then the velocity of the envelope, or group velocity, is $V_g = 0.07/0.0228 = 3.07\ m/ms$ which is very near the predicted group velocity of A_0 labelled on Fig. 6.3.

Although the fingers do not have the same behaviour for a given input of energy, A_0 has been excited properly and a great care will have to be taken concerning the voltage amplitude for the calculation of the correct spatial exponential decrease presented in the following section.

6.2 Plate in water

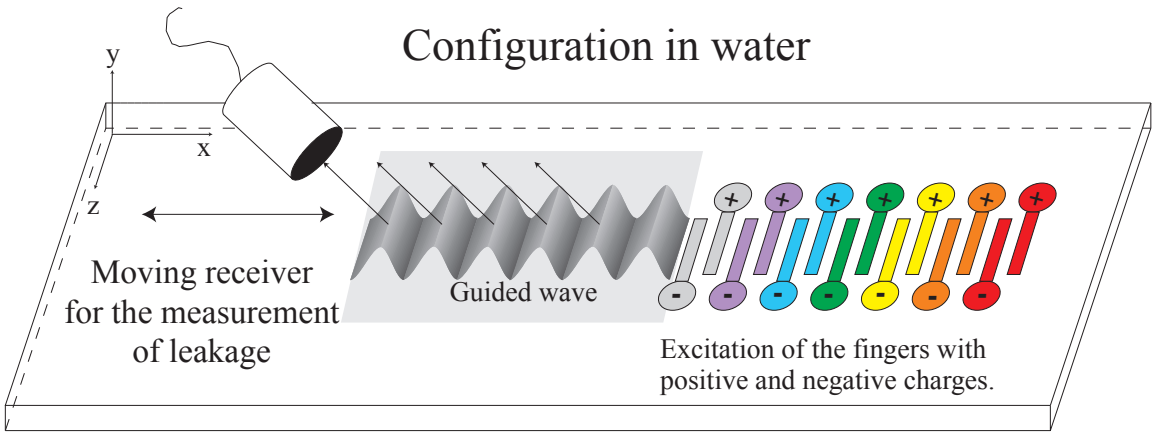

Figure 6.5: Experimental setup for the aluminium plate in water.

In this section we study the same plate as in the previous section but which is now immersed in water (Fig. 6.5). The experiments were conducted using a 5 MHz broad band immersion transducer (KB-AEROTECH) as a receiver. The dispersion curves for the plate in water are presented in Fig. 6.6. Although all the modes that belong to the dark grey region can potentially be excited if they are not too attenuated and if the frequency is well adapted, we decided to focus our attention on A_2 because its attenuation is the smallest. The corresponding incident angle is $\theta = 13.14°$ and the frequency is $f = 3.476\ MHz$. It is to be noted that A_0 could not be studied because of its very high attenuation.

In the frequency domain, a large number of cycles reduces the frequency spectrum. This is of course important in order to be selective regarding the mode one chooses to excite. However, can the number of fingers reduce the wavenumber spectrum? To answer this question, we perform several linear scans over 50 mm and sample the signals every 0.1 mm, each time disconnecting one pair of electrodes. The temporal signals stored for each position of the receiver are then processed using a two dimensional fast Fourier transform [2], giving the frequency versus wavenumber plots presented in Fig. 6.7. The results are also projected as contour lines on the theoretical dispersion curves. Part a) shows the results when all the fingers are connected and parts b), c), d), e), f) and g) show

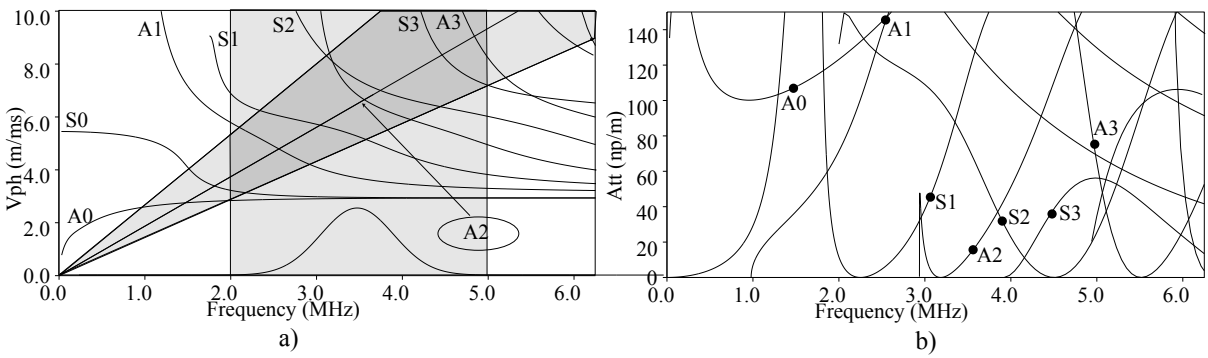

Figure 6.6: Dispersion curves for a 1.6-mm thick aluminium plate immersed in water. Part a) shows phase velocity and part b) shows attenuation, both plotted versus frequency.

the results when the following pairs [O, Y, G, P, B, Gr], [Y, G, P, B, Gr], [G, P, B, Gr], [P, B, Gr], [B, Gr] and [Gr] are respectively connected.

In all situations, S_1, A_2 and S_2 are excited. A_2 has the highest amplitude and S_1 the lowest as predicted by the dispersion curves of Fig. 6.6. However, the number of excited fingers does not seem to play a very important role. As a matter of fact, the wavenumber spectrum does not really expand as and when the different pairs of electrodes are disconnected. This can be understood if we consider the high amplitude loss due to the propagation in the adhesive: the further the fingers are from the receiver, the greater the propagation distance within the adhesive is. As a conclusion, the contribution of the fingers that are far from the receiver is very weak and the number of connected fingers cannot really reduce the wavenumber spectrum. Moreover, as the same amount of energy has been sent through the different pairs of fingers and as the amplitude of the received signals is higher when all the fingers are connected, we can then postulate that even if the wavenumber spectrum is not reduced, a certain number of fingers is however necessary in order to be mode selective. This is evident in part g) where more of the unwanted A_3 mode is excited than when all the fingers are connected.

As a final experiment, we now focus our attention on the attenuation of A_2. At 3.476 MHz, the attenuation of A_2 is 20.89 Np/m which means that if the amplitude is 1 at $x = x_0$ then after propagating 1 meter the amplitude will be $e^{-20.89} = 0.846e^{-9}$ and in order to be very mode selective, the signal now contains 100 cycles.

For a given voltage fixed at 1.5 V in the red pair of fingers, the theoretical voltages are presented in table 6.1 for both the rectangular and the exponential excitation.

However, we have to remember that pairs of electrodes do not have the same behaviour because of the damping in the adhesive. We therefore have to correct the theoretical voltages with respect to the measured loss due to the adhesive. In order to calculate it, we excite each pair of fingers in turn with an initial input of 1.5 V, moving the receiver by the correct number of wavelengths in order that the distance of propagation along the plate

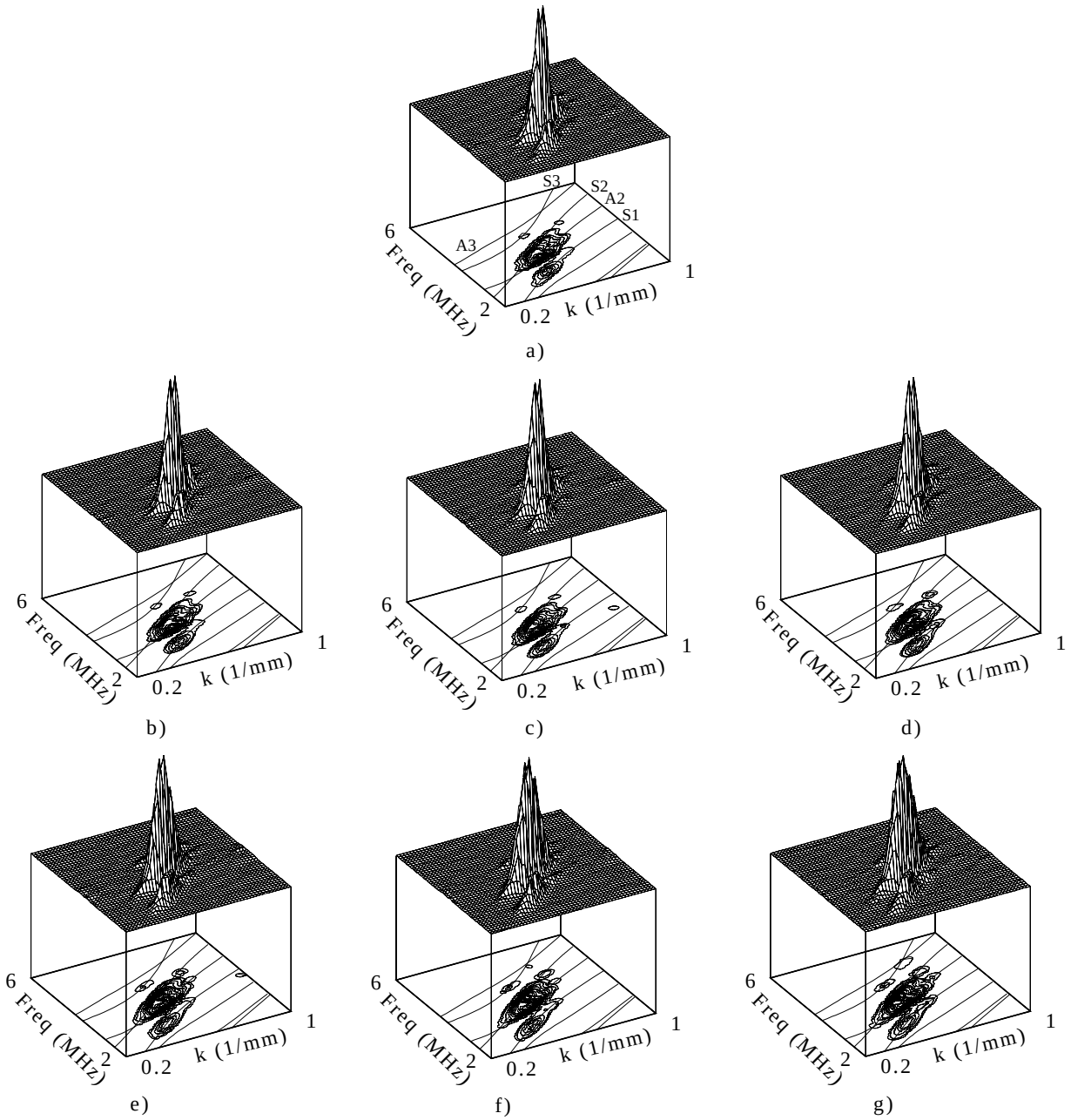

Figure 6.7: Comparison between the two dimensional FFT plots and the dispersion curves calculated for a 1.6-mm thick aluminium plate immersed in water. a) all finger pairs are connected, b) all but R, c) all but R and O, d) all but R, O and Y, e) all but R, O, Y and G, f) all but R, O, Y, G and P g) R, O, Y, G, P and B. All those letters being defined in Fig. 6.2

	red	orange	yellow	green	blue	purple	grey
exponential	1.5	1.44	1.39	1.33	1.28	1.23	1.19
rectangular	1.5	1.5	1.5	1.5	1.5	1.5	1.5

Table 6.1: Theoretical voltages for each pair of electrodes for both an exponential and a rectangular spatial input.

stays the same for each pair of electrode (the size of the transducer is small compared to the distance propagated along the plate). The setup is described in Fig. 6.8. This simple model does not of course take into account other phenomena that could also occur at the same time and we assume that the reverberation between the fingers does not affect the voltage. They should therefore be the same for both the exponential and the rectangular excitation.

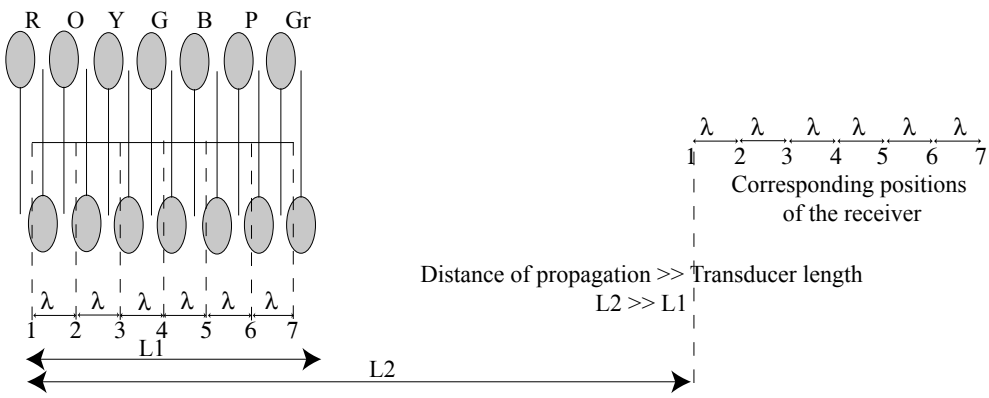

Figure 6.8: Setup for the measurement of loss in the adhesive.

The maximum of each received signal at the locations numbered from 1 to 7 in Fig. 6.8, calculated in the frequency domain after a Fourier transform, is measured and shown in table 6.2 for a constant input of 3 V. As the distance travelled along the plate is the same for each pair of electrodes, and as only A_2 is excited (with very narrow bandwidth), the difference between the amplitudes gives us the percentage loss within the adhesive. The attenuation coefficient of the adhesive (α) can be estimated from the factor required to equalize the voltage contributions from each of the finger pairs to that of the grey pair, taking account of the path length through the adhesive. This coefficient is also expressed in table 6.2.

	red	orange	yellow	green	blue	purple	grey
Amplitude	1961.29	2127.53	1670.49	2779.34	1155.41	2318.69	3160.75
α	1.611	1.486	1.892	1.137	2.736	1.363	1

Table 6.2: Maximum amplitudes (arbitrary units) within the Fourier transform spectrum of each received signal at 3.476 MHz.

Finally, table 6.3 shows the correct voltages to be applied in order to excite either an exponential or a rectangular field, the aim being to have 1.5 V on the grey pair when the excitation is rectangular.

	red	orange	yellow	green	blue	purple	grey
Rectangular	2.42	2.23	2.84	1.71	4.1	2.04	1.5
Exponential	2.42	2.15	2.65	1.54	3.56	1.71	1.24

Table 6.3: Corrected voltages for both the rectangular and the exponential profiles in order to excite A_2.

We now have all the parameters in order to perform our two experiments. For each voltage presented in table 6.3 we sample the signals, use the principle of superposition and measure the amplitude of the peak, in the frequency domain, of the resulting spectrum. When the source is rectangular, the maximum amplitude corresponds (in arbitrary units) to $R_{rectangular} = 1.1811$, and when the source is exponential to $R_{exponential} = 1.1509$. Although $R_{exponential}$ is lower than $R_{rectangular}$ we have to take into account the total amount of energy that has been sent. As a matter of fact, the energy sent when the source is exponential is lower than when it is rectangular as shown in Fig. 6.9.

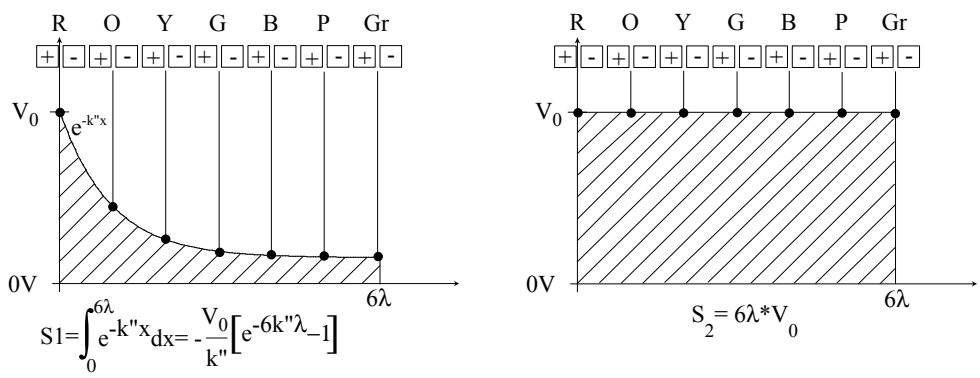

Figure 6.9: Energy distribution when the source is rectangular or exponential.

The surface for an exponential input is defined by:

$$S_{Exponential} = V_0 \int_0^{6\lambda} e^{-k''x} dx = \frac{V_0}{k''} \left[e^{-6\lambda k''} - 1 \right], \tag{6.1}$$

whereas it corresponds to:

$$S_{Rectangular} = 6\lambda V_0, \tag{6.2}$$

for a rectangular input. In our experiment, the initial input is $V_0 = 1.5\ V$ and the different surfaces respectively correspond to $S_{Exponential} = 15.003\ V.mm$ and $S_{Rectangular} =$

16.83 $V.mm$. As a consequence, if we had used the same amount of energy for the exponential input as for the rectangular, the amplitude of the peak for the exponential input would have been: $\tilde{R}_{Exponential} = 1.291$ which corresponds to an increase of amplitude of 9.3% compared to the amplitude of the peak when the source is rectangular. Hence, the amplitude of the response is greater when the experimental setup takes into account the imaginary part of the slowness than when it does not.

In order to confirm this result we now focus our attention on S_1. Although this mode has a greater attenuation (53.44 Np/m at 2.98 MHz), it can however be well separated from the other modes with a very narrow frequency bandwidth as shown in Fig. 6.6. The correct voltages are given in table 6.4 below:

	Input type	red	orange	yellow	green	blue	purple	grey
Theoretical	Rectangular	3	3	3	3	3	3	3
	Exponential	3	2.71	2.46	2.22	2.01	1.82	1.65
Corrected	Rectangular	4.83	4.46	5.68	3.41	8.21	4.09	3
	Exponential	4.83	4.03	4.65	2.52	5.5	2.48	1.65

Table 6.4: Theoretical and corrected voltages for both the rectangular and the exponential profiles in order to excite S_1.

In this case, the different surfaces respectively correspond to $S_{Exponential} = 25.32\ V/mm$ and $S_{Rectangular} = 33.66\ V/mm$ and the amplitudes to $R_{rectangular} = 6.24$ and $R_{exponential} = 5.77$. Again, if we had used the same amount of energy for the exponential input as for the rectangular, the amplitude of the peak for the exponential input would have been: $\tilde{R}_{Exponential} = 7.67$ which corresponds to an increase of amplitude of 22.93% compared to the amplitude of the peak when the source is rectangular. In this case, the amplitude gain is greater because the attenuation of the mode is higher. This can be understood if we consider that if the attenuation is low then the inputs are almost rectangular: the length of the transducer is too small to take into account the exponential decrease. However, when the attenuation is higher, the small length of the transducer allows a better modelling of the exponential decrease.

6.3 Conclusion

In contrast to the modes which propagate in lossless plates surrounded by vacuum and which are characterized by a frequency and a slowness, both real, modes which propagate in immersed lossless plates leak energy into the surrounding medium. The leakage is modelled by a complex slowness whose imaginary part corresponds to the attenuation during the propagation along the plate. Usual experiments only take into account two of the mode properties in order to excite them: the frequency and the real part of the slowness. In this chapter we set up our experiment in such way that it takes into account all three properties

of the mode; that is the frequency, the real part of the slowness and also the imaginary part of the slowness.

To do so, we used an interdigital transducer bonded on an aluminium plate and whose fingers were physically independent. This condition was necessary in order to be able to apply an exponential decrease in space. Although it is true that increasing the number of cycles reduces the frequency spectrum, increasing the number of finger pairs does not reduce the wavenumber spectrum. This is explained by the high loss of amplitude during the propagation within the adhesive which damps the signals. However a certain number of pairs seems to be necessary in order to be more mode selective. Finally, we demonstrated that for the same energy contribution, the received signal amplitude was higher when the input took into account the attenuation of the mode than when it was rectangular. Then, if mode selection requires narrow frequency bandwidth as well as a narrow wavenumber bandwidth in order to match the phase velocity dispersion curves, this also requires the adequate exponential spatial field to match the imaginary part of the mode.

Chapter 7

Conclusion

The structure of transient heterogeneous plane waves has been studied as part of the acoustic propagation in infinite isotropic media. Those waves are characterized by amplitudes which can decrease exponentially both in time and in space. If the complex wavenumber bivector $^*\mathbf{K}$ is well suited to describe harmonic heterogeneous plane waves with real frequency, it turns out that it is not well suited to describe, in a satisfactory way, the behaviour of transient heterogeneous plane waves with complex frequency. As a matter of fact, this bivector, containing both spatial and temporal information, does not allow a good quantification of each of these contributions. As a consequence, the complex slowness bivector $^*\mathbf{S}$ has been introduced in order to describe the spatial properties of these waves, the complex frequency being directly linked to the temporal properties.

Then, the modes of an isotropic plate embedded in an infinite isotropic medium have been studied and the corresponding symmetric and anti-symmetric Lamb wave functions have been analytically calculated. While only a small difference existed, in the case of an immersed plate in water, between these two sets of dispersion curves, the dispersion curves for the solid embedded in solid are now completely different. In the framework of the coincidence angle principle which postulates that dispersion curves are linked to the zeroes of the plane wave reflection coefficient, when the impedance of the different media are different, the response problem for the solid/solid/solid configuration has also been considered. The longitudinal and the shear plane wave reflection coefficients have been calculated and compared with the two sets of dispersion curves. Although no correspondence exists between the plane wave reflection coefficient zeroes and the dispersion curves for complex slowness, those calculated in complex frequency and real slowness describe perfectly the plane wave reflection coefficient zeroes in regions where their imaginary parts are zero. Thus, plane wave reflection coefficient zeroes do not properly describe the structure of harmonic inhomogeneous plate modes $(\omega, ^* S)$ for media which have similar impedance. On the other hand, they seem to better describe the structure of transient homogeneous plate modes $(^*\omega, S)$. As a conclusion, although modal properties with the complex slowness approach could not be studied anymore using plane wave reflection coefficient zeroes

when the impedance of the surrounding medium is very similar to that of the plate, the complex frequency approach seems to enable a model that is still consistent.

In order to confirm those statements, we therefore studied the response of an isotropic plate embedded in an infinite isotropic medium, for an incident wave that was supposed to be plane and infinite in space but bounded in time: in these conditions the hypothesis of real slowness is verified. For a fixed angle of incidence directly linked to the slowness with the Snell-Descartes laws, the incident temporal signal is modelled by a long sine wave modulated by a square function whose frequency corresponds to the real part of the frequency of the mode we decided to excite. The temporal response of the plate is then characterized by two transients which appear at the beginning and at the end of the steady state and by a zone with zero amplitude. In fact, the transient parts are increasing or decreasing exponential functions directly linked to the imaginary part of the frequency of the selected mode. Moreover, the zone with zero intensity corresponds to the infinite plane wave reflection coefficient: the incident plane wave is infinite (our first assumption) and the steady state only contains a single frequency. As a conclusion, the plane wave reflection coefficient zeroes are clearly directly linked to the transient homogeneous plate modes.

In a second approach, we studied the response of an isotropic plate immersed in water for an incident plane wave which is harmonic but bounded in space. The incident field is modelled by a Gaussian function whose width is directly linked to the spatial aperture of the transducer. For a fixed angle of incidence and a fixed frequency both corresponding to the selected plate mode properties, the plate response is a deformed Gaussian field. This field is characterized by a zone with zero amplitude but especially by a spatial exponential decrease corresponding to the imaginary part of the slowness of the mode. Again, the reflection coefficient properties are linked to the free modes of the plate.

The two extreme cases having been presented we finally looked at the general case where both time and space are bounded. For several angles of incidence, the spectrum of the temporal part of the reflected field has been studied at different positions along its spatial part. This enabled us to build a cartography of the properties of the plate response at a location where the reflection is known as “specular” but also at locations much further away. Dispersion curves with complex frequency are again in perfect agreement with the zeroes of the reflected field when we look for them in the specular reflection. However, as and when we move further away, zeroes transform into maxima and maxima transform into zeroes. These maxima then describe dispersion curves with complex frequency but also with complex slowness and their intensities are directly linked to the spatial attenuation of the modes. In this study, we confirmed that experimental results clearly depend on the position of the receiver. In the specularly reflected zone, zeroes of the reflected field correspond to the dispersion curves with complex frequency (in this zone there is no spatial discontinuities and the slowness is real). Far from this zone, there are no more zeroes but maxima which correspond this time to the two types of dispersion curves (with complex

slowness but also with complex frequency) and whose intensities depend on the imaginary parts of the modes.

Both the frequency and the slowness are useful parameters to describe accurately the properties of plate modes, however we showed that group velocity, widely used experimentally as a first approximation to describe the velocity of the wave packets, could lead to some errors. As a matter of fact, its definition is only valid when modes are not attenuated. On the other hand, we showed that a calculation of energy velocity could be substituted satisfactorily. This velocity, based on the integration of the Poynting vector as well as on the integration of the total energy of plate modes over a time period and over the thickness of the plate, is rigorously equal to the group velocity when the modes are not attenuated but describes perfectly the velocity of the wave packets when there is attenuation. As a matter of fact, experimental results conducted on a highly viscoelastic plate in vacuum showed a very good correlation between the energy velocity and the measurement of the wave packet velocities in regions where modes were highly attenuated.

Finally, experimental results using interdigital transducers have been presented for an aluminium plate in vacuum and immersed in water. The fingers being independent, a quantitative analysis proved that if the number of cycles can reduce the frequency spectrum of a temporal signal, in return the number of fingers does not allow a reduction in the spatial spectrum relative to the wavenumber. This feature is the result of the high attenuation within the adhesive used to bond the IDT to the plate. Moreover, we showed that in addition to the (frequency, real part of the slowness), the spatial form of the input played an important role too. As a matter of fact, the account of the imaginary part of the slowness, corresponding to an exponentially decreasing energy distribution in space regarding the different finger pairs, lead the response to have a greater amplitude than when the source is rectangular.As a conclusion, we demonstrated that an experimental setup which takes into account all three properties of a mode results in a received signal which has a greater amplitude than an experimental setup which does not.

Although Lamb wave functions have extensively been studied for many years, this thesis, which is an extension of Dr Poncelet's thesis [68], also confirms that the simple fact to change the way of solving such equations results in solutions whose characteristics are completely different. While harmonic attenuated guided waves decay in space, transient homogeneous guided waves decay in time. As a consequence, the complexity which exists in modelling mechanics problems has been clearly illustrated since these two solutions exist physically and in fact depend on the experimental setup. Moreover, as in the case of an isotropic plate immersed in water we also showed that a mode with negative attenuation in time could also exist when the geometry is more complicated. Finally, we solved the limitations to using group velocity as a description of wave systems in attenuating materials by integrating energy velocity. These fundamental concepts helped us to have a better understanding about guided waves in general and in fact have been included as new options in the general purpose model "Disperse" [59] (an interactive program for generating

dispersion curves) developed by B. Pavlakovic and M. J. S. Lowe in the non destructive testing laboratory of Imperial College.

La structure des ondes planes hétérogènes transitoires a été étudiée dans le cadre de la propagation acoustique dans des milieux isotropes infinis. Ces ondes sont caractérisées par des amplitudes qui décroissent exponentiellement à la fois en espace et en temps. Si le bivecteur complexe nombre d'onde $^*\mathbf{K}$ *est bien adapté pour décrire les ondes planes harmoniques hétérogènes où la fréquence est réelle, il s'avère qu'il ne l'est pas pour décrire, de manière satisfaisante, le comportement des ondes planes hétérogènes transitoires où la fréquence est complexe . En effet, ce bivecteur, contenant les informations à la fois spatiales et temporelles, ne permet pas de quantifier le poids de l'une ou l'autre de ces contributions. En conséquence, le bivecteur complexe lenteur* $^*\mathbf{S}$ *a été introduit pour décrire le caractère spatial de ces ondes, la fréquence complexe étant directement liée au caractère temporel.*

Ensuite, les modes propres d'une plaque isotrope prise en sandwich dans un solide isotrope infini ont été étudiés et les fonctions symétriques et anti-symétriques de Lamb correspondantes calculées analytiquement. Alors qu'une faible différence existait, dans le cas d'une plaque immergée, entre une résolution en fréquence complexe et lenteur réelle et une résolution en fréquence réelle et lenteur complexe, les courbes de dispersion sont maintenant complètement différentes. Dans le cadre du principe de coïncidence angulaire qui postule que les courbes de dispersion sont liées aux zéros du coefficient de réflexion en ondes planes, lorsque les impédances des milieux sont différentes, le problème en réponse pour la configuration solide/solide/solide a donc lui aussi été considéré. Les coefficients de reflexion longitudinaux et transverses ont été calculés et comparés aux courbes de dispersion en fréquence complexe et aux courbes de dispersion en lenteur complexe. Alors qu'aucune correspondance n'existe entre les zéros des coefficients de reflexion et les courbes de dispersion en lenteur complexe, celles calculées en fréquence complexe et lenteur réelle décrivent cependant parfaitement les zéros des coefficients de réflexion dans des zones où leurs parties imaginaires sont nulles. Ainsi, les zéros des coefficients ne décrivent pas correctement la structure des modes de plaques harmoniques inhomogènes $(\omega, ^*S)$ *lorsque les impédances des milieux sont très proches les unes des autres. D'un autre côté ils semblent décrire la structure des modes de plaques homogènes transitoires* $(^*\omega, S)$*. En conclusion, alors que les propriétés des modes de plaques ne pouvaient plus être étudiées avec une approche en lenteur complexe en utilisant les zéros du coefficient de réflexion lorsque l'impédance du milieu environnant est très similaire de celle de la plaque, l'approche en fréquence complexe semble permettre une modélisation plus consistante.*

Afin de confirmer ces dires, nous avons donc étudié la réponse d'un plaque isotrope prise en sandwich dans un milieu infini isotrope pour une onde incidente supposée plane et infinie en espace mais bornée dans le temps: dans ces conditions l'hypothèse de lenteur réelle est vérifiée. Pour un angle d'incidence fixé et directement lié à la lenteur par les lois de Snell-Descartes, le signal temporel incident est modélisé par un long train de sinusoïdes modulé par une fonction porte dont la fréquence correspond à la partie réelle de la fréquence du mode que nous avons choisie d'exciter. La réponse temporelle de la plaque est alors caractérisée par deux transitoires qui apparaissent au début et à la fin du régime forcé et par une zone d'amplitude nulle. En fait, les transitoires sont des exponentielles croissantes ou

décroissantes directement liées à la partie imaginaire de la fréquence du mode sélectionné. De plus, la zone d'intensité nulle correspond au module du coefficient de réflexion pour une onde plane incidente harmonique infinie: l'onde incidente est par hypothèse infinie et le régime forcé ne contient qu'une seule fréquence. En conclusion, les zeros du coefficient de réflexion sont bien directement liés aux modes propres de plaques homogènes transitoires.

Dans un deuxième temps, nous avons étudié la réponse d'une plaque isotrope immergée dans l'eau pour une onde plane incidente harmonique mais bornée en espace. Le champ incident est modélisé par une fonction Gaussienne dont la largeur est directement liée à l'ouverture spatiale du traducteur. Pour un angle d'incidence et une fréquence fixés correspondant aux propriétés du mode de plaque sélectionné, la réponse de la plaque est alors un champ Gaussien déformé. Ce champ est caractérisé par une zone d'amplitude nulle mais surtout par une décroissance spatiale correspondant à la partie imaginaire de la lenteur du mode. De nouveau, les propriétés du coefficient de réflexion sont liées aux modes propres de plaques.

Les deux cas extrèmes ayant été présentés, nous nous sommes finalement intéressés au cas général où le temps et l'espace sont tout les deux bornés. Pour plusieurs angles d'incidence, le spectre de la partie temporelle du champ réfléchi a été étudié à différentes positions le long de la partie spatiale de ce même champ. Ceci nous a alors permis de construire une cartographie des propriétés de la réponse de la plaque à l'intérieur même de la réflexion dîte spéculaire ainsi qu'à des endroits beaucoup plus éloignés. Les courbes de dispersion en fréquence complexe sont de nouveau en parfait accord avec les zéros du champ réfléchi lorsque nous le regardons dans la partie spéculaire. Cependant, au fur et à mesure que nous nous en éloignons, les zéros se transforment en maxima, et les maxima en zéros. Ces maximas décrivent alors les courbes de dispersion en lenteur complexe et leurs intensités sont directement liées à l'atténuation spatiale des modes. Dans cette étude, nous avons confirmé que les résultats expérimentaux dépendent clairement de la position du récepteur. Dans la zone de réflexion spéculaire, les zéros du champ réfléchi correspondent aux courbes de dispersion en fréquence complexe (dans cette zone il n'y a pas de discontinuité spatiale et la lenteur est réelle). Loin de cette zone, il n'y a plus de zéros mais des maxima qui correspondent cette fois-ci aux deux types de courbes de dispersion (en lenteur complexe mais aussi en fréquence complexe) dont les intensités dépendent des parties imaginaires des modes.

Si la fréquence et la lenteur sont des paramètres utiles pour décrire les propriétés des modes de plaques, nous avons montré que la notion de vitesse de groupe, très utilisée expérimentalement en première approximation pour décrire la vitesse des paquets d'ondes, pouvait conduire à certaines erreures. En effet, sa définition n'est valide que lorsque les modes ne sont pas atténués. Dans le cas contraire, nous avons montré que la vitesse de l'énergie pouvait lui être substituée. Cette vitesse, basée sur l'intégration du vecteur de Poynting et de l'énergie totale des ondes de plaques sur une période ainsi que sur l'épaisseur de la plaque, est rigoureusement égale à la vitesse de groupe lorsque les modes

ne sont pas atténués mais décrit parfaitement la vitesse des paquets des modes lorsqu'il y a de l'atténuation. En effet, des résultats expérimentaux conduits sur une plaque de type PVC fortement viscoélastique dans le vide ont montré une trés bonne corrélation entre la vitesse de l'énergie théorique et la mesure de la vitesse des paquets des ondes à des endroits où les modes étaient très atténués.

Pour finir, des résultats expérimentaux utilisant des traducteurs inter-digitaux ont été présentés pour une plaque d'aluminium dans le vide puis immergée dans de l'eau. Les doigts étant tous indépendants, une analyse quantitative a prouvé que si le nombre de cycles permet de réduire le spectre fréquentiel d'un signal temporel, en revanche le nombre de doigts ne permet pas quant à lui de réduire le spectre spatial relatif au nombre d'onde. Ceci est le résultat d'une grande atténuation dans l'adhésif utilisée pour coller le traducteur à la plaque. De plus, nous avons montré qu'en plus du couple (fréquence, partie réelle de la lenteur), la forme spatiale de la sollicitation jouait aussi un rôle important. En effet, la prise en compte de la partie imaginaire de la lenteur, correspondant à un apport d'énergie exponentiellement décroissant en espace au niveau des différentes paires de doigts, a entrainé une réponse de plus forte amplitude que lorsque la source était rectangulaire. En conclusion, nous avons démontré qu'une configuration expérimentale, qui prennait en compte les trois propriétés d'un mode, entraînait un augmentation de l'amplitude du signal reçu plutôt qu'une configuration qui n'en prennait en compte que deux.

Bien que les fonctions de Lamb aient été étudiées de manière extensive depuis un grand nombre d'années, cette thèse, qui est une extension de la thèse d'Olivier Poncelet [68], confirme que le simple fait de changer la manière de résoudre de telles équations peut nous conduire à des solutions dont les caractéristiques sont complètement différentes. Alors que les ondes guidées harmoniques et atténuées décroissent exponentiellement en espace, les ondes guidées transitoires et homogènes décroissent en temps. En conséquence, la complexité qui existe lors de la modélisation de problèmes mécaniques a clairement été illustrée puisque ces deux solutions existent physiquement et qu'elles dépendent en fait de la configuration expérimentale. De plus, comme dans le cas de la plate isotrope immergée dans l'eau, nous avons montré qu'un mode possédant une atténuation négative en temps pouvait aussi exister pour des géométries plus compliquées. Enfin nous avons comblé le manque d'exactitude de la vitesse de groupe en introduisant la vitesse de l'énergie. Ces concepts fondamentaux nous ont aidé dans la compréhension des ondes guidées en général et ont, en fait, été introduits, en tant que nouvelles options, dans le logiciel "Disperse" [59] (un programme interactif pour générer des courbes de dispersion) développé par B. Pavlakovic et M. J. S. Lowe dans le laboratoire de contrôle non destructif de l'Imperial College.

Chapter 8

Bibliography

Bibliography

[1] J.D. Achenbach. *Wave propagation in elastic solids.* North-Holland, Amsterdam, 1973.

[2] D. Alleyne and P. Cawley. A two-dimensional fourier transform method for the measurement of propagating multimode signals. *Journal of the Acoustical Society of America*, 89:1159–1168, 1991.

[3] D.N. Alleyne and P. Cawley. Optimization of lamb wave inspection techniques. *NDT and E International*, 25:11–22, 1992.

[4] B.A. Auld. *Acoustic Fields and Waves in Solids*, volume 1. Krieger Publishing Company Malabar, Florida, 1990.

[5] H. L. Bertoni and T. Tamir. Unified theory of rayleigh-angle phenomena for acoustic beams at liquid-solid interfaces. *Applied Physics*, 2:157–172, 1973.

[6] M. Billy de and I. Molinero. On the nonobservence of nonspecular bounded beam reflection effects on lamb waves. *Journal of the Acoustical Society of America*, 83(4):1249–1254, 1988.

[7] M.A. Biot. General theorems on the equivalence of group velocity and energy transport. *Physical review*, 105(4):1129–1137, 1957.

[8] P. Borejko. Inhomogeneous plane waves in a constrained elastic body. *Quart. J. Mech. Appl. Math.*, 40:70–87, 1987.

[9] M. Breazeale, L. Adler, and G. Scott. Interaction of ultrasonic waves incident at the raleigh angle onto a liquid-solid interface. *Journal of Applied Physics*, 48:530–537, 1977.

[10] M.A. Breazeale, L. Adler, and L. Flax. Reflection of a gaussian ultrasonic beam from a liquid-solid interface. *Journal of the Acoustical Society of America*, 56:866–873, 1974.

[11] L.M. Brekhovskikh. *Waves in layered media.* Academic Press, New York, 1960.

[12] L. J. F Broer. On the propagation of energy in linear conservative waves. *Journal of Applied Science Research*, A(2):329–344, 1951.

[13] P. Cawley and M.J.S. Lowe. The applicability of plate wave techniques for the inspection of adhesive and diffusion bonded joints. *Journal of Non-destructive Evaluation*, 13:185–199, 1994.

[14] C.W. Chan and P. Cawley. The existence of low loss modes in highly attenuative viscoelastic media. In D.O. Thompson and D.E. Chimenti, editors, *Review of Progress in Quantitative NDE*, volume 15(A), pages 193–200. Plenum Press, New York, 1996.

[15] C.W. Chan and P. Cawley. Lamb waves in highly attenuative plastic plates. *Journal of the Acoustical Society of America*, 104(2):874–881, 1998.

[16] P. Chevée and M. Deschamps. Non-specular effects of reflection and transmission at an immersed viscoelastic-anisotropic layer. *Ultrasonics International*, 1991.

[17] D.E. Chimenti and A.H. Nayfeh. Anomalous ultrasonic dispersion in fluid-coupled fibrous composite plates. *Applied Physics Letters*, 49:492, 1986.

[18] D.E. Chimenti and S.I. Rokhlin. Relationship between leaky lamb modes and reflection coefficient zeros for a fluid-coupled elastic layer. *Journal of the Acoustical Society of America*, 88:1603–1611, 1990.

[19] J. M. Claeys and O. Leroy. Reflection and transmission of bounded sound beam on half-spaces and through plates. *Journal of the Acoustical Society of America*, 72(2):585–590, 1982.

[20] P. Delestre, J. Izbicki, G. Maze, and J. Ripoche. Excitation acoustique impulsionnelle d'une plaque élastique immergée: application à l'isolement des résonances. *Acoustica*, 61:83–85, 1986.

[21] M. Deschamps and P. Chevée. Reflection and transmission of a transient bounded beam by a dispersive and orthotropic plate. *Acta Acustica*, 1:3–14, 1993.

[22] M. Deschamps, B. Poirée, and O. Poncelet. Energy velocity of complex harmonic plane waves in viscous fluids. *Wave Motion*, 25:51–60, 1997.

[23] M. Deschamps and O. Poncelet. Plate waves with complex frequency and total transmission. In *Proceedings of Ulrasonics World Congress*. Yokohama, 1997.

[24] M. Deschamps and O. Poncelet. Transient lamb waves: Comparison between theory and experiment. *Journal of the Acoustical Society of America*, 107(6):3120–3129, 2000.

[25] M.J. Evans, J. R. Webster, and P. Cawley. Design of a self-calibrating simulated acoustic emission source. *Ultrasonics*, 37:589–594, 2000.

[26] R. Fiorito and H. Überall. Resonance theory of acoustic reflection and transmission through a fluid layer. *Journal of the Acoustical Society of America*, 65(1):1857–1866, 1979.

[27] R. Fiorito, W. Madigosky, and H. Überall. Resonance theory of acoustic waves interacting with an elastic plate. *Journal of the Acoustical Society of America*, 66(6):1857–1866, 1979.

[28] R. Fiorito, W. Madigosky, and H. Überall. Theory of ultrasonic resonances in a viscoelastic layer. *Journal of the Acoustical Society of America*, 77(2):489–498, 1985.

[29] K.F. Graff. *Wave Motion in Elastic Solids*. Dover Publicaitons inc., New York, 1973.

[30] M. Hayes. A note on group velocity. *Proc. Roy. Soc. London A*, 354:533–535, 1977.

[31] M. Hayes and M.J.P. Musgrave. On energy flux and group velocity. *Wave motion*, 1:75–82, 1979.

[32] J. Izbicki, G. Maze, and J. Ripoche. Diffusion acoustique par des tubes immergés dans l'eau: nouvelles résonances observées en basse fréquence. *Acoustica*, pages 137–139, 1986.

[33] J. L. Izbicki, G. Maze, and J. Ripoche. Etude de la réémission libre d'une plaque résonnante. *Acustica*, 55:27–29, 1984.

[34] T. Kundu. On the nonspecular reflection of bounded acoustic beams. *Journal of the Acoustical Society of America*, 83:18–24, 1988.

[35] T. Kundu, A.K. Mal, and R.D. Weglein. Calculation of the acoustic material signature of a layered solid. *Journal of the Acoustical Society of America*, 77:353–361, 1985.

[36] H. Lamb. On waves in an elastic plate. In *Proceedings of the Royal Society*, volume 93 PT Series A, pages 114–128. London, 1917.

[37] O. Lenoir, J. Duclos, J.M. Conoir, and J.L. Izbicki. Study of lamb waves based upon the frequency and angular derivatives of the phase of the reflection coefficient. *Journal of the Acoustical Society of America*, 94:330–343, 1993.

[38] M.J. Lighthill. Group velocity. *J. Inst. Maths Applics*, 1:1–28, 1965.

[39] O.I. Lobkis and D.E. Chimenti. Three-dimensional transducer voltage in anisotropic materials characterization. *Journal of the Acoustical Society of America*, 106(1):36–45, 1999.

[40] O.I. Lobkis, D.E. Chimenti, and H. Zhang. In-plane elastic property characterization in composite plates. *Journal of the Acoustical Society of America*, 107(4):1852–1858, 2000.

[41] O.I. Lobkis, A. Safaeinili, and D.E. Chimenti. Precision ultrasonic reflection studies in fluid-coupled plates. *Journal of the Acoustical Society of America*, 99:2727–2736, 1996.

[42] M. Lowe. Matrix techniques for modeling ultrasonic waves in mutilayered media. *IEEE Transactions on Ultrasonics, Ferroelectrics and Frequency control*, 42:525–542, 1995.

[43] M. Lowe and P. Cawley. The detection of a brittle layer at the bondline in diffusion bonded titanium. In D.O. Thompson and D.E. Chimenti, editors, *Review of Progress in Quantitative NDE*, pages 1653–1659. Plenum Press, New York, 1993.

[44] M. Lowe and P. Cawley. Comparison of reflection coefficient minima with dispersion curves for ultrasonic waves in embedded layers. In D.O. Thompson and D.E. Chimenti, editors, *Review of Progress in Quantitative NDE*, pages 1505–1512. Plenum Press, New York, 1996.

[45] M.J.S. Lowe and P. Cawley. Comparison of the modal properties of a stiff layer embedded in a solid medium with the minima of the plane-wave reflection coefficient. *Journal of the Acoustical Society of America*, 97:1625–1637, 1995.

[46] M.J.S. Lowe and P. Cawley. The influence of the modal properties of a stiff layer embedded in a solid medium on the field generated in the layer by a finite-sized transducer. *Journal of the Acoustical Society of America*, 97:1638–1649, 1995.

[47] W. Madigodsky and R. Fiorito. Modal resonance analysis of acoustic transmission and reflection losses in viscoelastic plates. *Journal of the American Society of America*, 65(5):1105–1114, 1979.

[48] F. Mainardi. Energy velocity for hyperbolic dispersive waves. *Wave motion*, 9:201–208, 1987.

[49] G. Maze, J. Izbicki, and J. Ripoche. Resonances of plates and cylinders: guided waves. *Journal of the American Society of America*, 77(4):1352–1357, 1985.

[50] G. Maze, J. Izbicki, and J. Ripoche. Transient acoustic scattering from layers and plates. *Journal of the Acoustical Society of America*, 80(1):295–301, 1986.

[51] G. Maze and J. Ripoche. Visualization of acoustic scattering by elastic cylinders at low ka. *Journal of the Acoustical Society of America*, 73(1):41–43, 1983.

[52] R.S.C. Monkhouse, P.D. Wilcox, and P. Cawley. Flexible interdigital pvdf lamb wave transducers for the development of smart structures. In D.O. Thompson and D.E. Chimenti, editors, *Annual review of progress in quantitative NDE*, volume 16. Plenum Press, New York, 1996.

[53] A.H. Nayfeh and D.E. Chimenti. Reflection of finite acoustic beams from loaded and stiffened half-spaces. *Journal of the Acoustical Society of America*, 75:1360–1368, 1984.

[54] A.H. Nayfeh and D.E. Chimenti. Propagation of guided waves in fluid-coupled plates of fibre-reinforced composite. *Journal of the Acoustical Society of America*, 83(5):1736–1743, 1988.

[55] A.H. Nayfeh and D.E. Chimenti. Ultrasonic wave reflection from liquid-coupled orthotropic plates with application to fibrous composites. *Journal of Applied Mechanics*, 55:863–870, 1988.

[56] W. Neubauer. Ultrasonic reflection of a bounded beam at rayleigh and critical angles for a plane liquid-solid interface. *Journal of Applied Physics*, 44 No 1:48–55, 1973.

[57] K.W. Ng, T.D.K. Ngoc, J. A. McClure, and W. G. Mayer. Nonspecular transmission effects for ultrasonic beams incident on a solid plate in a liquid. *Acustica*, 48:168–173, 1981.

[58] K.W. Ng, T.D.K. Ngoi, I. Molinero, and d.M. Billy. Measurement of the profile of an ultrasonic beam non-specularly reflected from a solid plate. *Ultrasonics*, 26:44–46, 1988.

[59] B.N. Pavlakovic, M.J.S. Lowe, D.N. Alleyne, and P. Cawley. Disperse: A general purpose program for creating dispersion curves. In D.O. Thompson and D.E. Chimenti, editors, *Review of Progress in Quantitative NDE*, volume 16, pages 185–192. Plenum Press, New York, 1997.

[60] R.A. Phinney. Leaking modes in the crystal waveguide. *Journal of Geophysical Research*, 66:1445–1469, 1961.

[61] T.P. Pialucha. *The reflection coefficient from interface layers in NDT of adhesive joints*. PhD thesis, University of London, 1992.

[62] L.E. Pitts, T. Plona, and W. Mayer. Theoretical similarities of rayleigh and lamb modes of vibration. *Journal of the Acoustical Society of America*, 60:374–377, 1976.

[63] L.E. Pitts, T. J. Plona, and W. G. Mayer. Theory of nonspecular reflection effects for an ultrasonic beam incident on a solid plate in a liquid. *IEEE Trans. Sonics and Ultrasonics*, SU-24 No 2:101–109, 1977.

[64] T. Plona, M. Behravesh, and W. Mayer. Rayleigh and lamb waves at liquid-solid boundaries. *Ultrasonics*, pages 171–174, 1975.

[65] T.J. Plona, L.E. Pitts, and W.G. Mayer. Ultrasonic bounded beam reflection and transmission effects at a liquid/solid-plate/liquid interface. *Journal of the Acoustical Society of America*, 59:1324–1328, 1976.

[66] B. Poirée. Vitesse de propagation de l'énergie de l'onde plane évanescente acoustique. *Revue du cethedec ondes et signal*, 79:103–111, 1984.

[67] B. Poirée. Les ondes planes évanescentes dans les fluides parfaits et les solides élastiques. *Journal Acoustique*, 2:205–216, 1989.

[68] O. Poncelet. *Ondes planes hétérogènes à fréquence complexe: modes propres de plaques immergées*. PhD thesis, Université de Bordeaux 1, 1996.

[69] O. Poncelet and M. Deschamps. Lamb waves generated by complex harmonic inhomogeneous plane wave. *Journal of the Acoustical Society of America*, 102:292–300, 1997.

[70] J. Ripoche, G. Maze, and J. Izbicki. New research in non-destructive testing: resonance acoustic spectroscopy. In *Ultrasonics International*, 1985.

[71] J. Ripoche, G. Maze, and J.-F. Izbicki. A new acoustic spectroscopy: resonance spectroscopy by the MIIR. *Journal of Non-destructive Evaluation*, 5(2):69–79, 1985.

[72] J.H. Rosenbaum. The long-time response of a layered elastic medium to explosive sound. *Journal of Geophysical Research*, 65:1577–1613, 1960.

[73] M. Rousseau and Ph. Gatignol. Asymptotic analysis of non specular effects for the reflection and the transmission of a gaussian acoustic beam incident on a solid plate. *Journal of the Acoustical Society of America*, 80(1):325–332, 1986.

[74] D. Royer and E. Dieulesaint. *Ondes élastiques dans les solides*, volume 1. Masson, Paris, 1996.

[75] R. Thompson, F. Margetan, J. Rose, and N. Batra. Effects of interstitial oxygen on the ultrasonic properties of titanium alloys. In D.O. Thompson and D.E. Chimenti, editors, *Review of Progress in Quantitative NDE*, volume 11, pages 1725–1731. Plenum Press, New York, 1992.

[76] K. Van den Abeele and O. Leroy. Complex harmonic wave scattering as the framework for investigation of bounded beam reflection and transmission at plane interfaces and its importance in the study of vibrational modes. *Journal of the Acoustical Society of America*, 93(1):308–323, 1993.

[77] K. Van den Abeele and O. Leroy. On the influence of frequency and width of and ultrasonic bounded beam in the investigation of materials: study in terms of heterogeneous plane waves. *Journal of the Acoustical Society of America*, 93(5):2688–2699, 1993.

[78] P. D. Wilcox. *Lamb wave inspection of large structures using permanently attached transducers*. PhD thesis, Department of Mechanical Engineering, Imperial College, 1998.

[79] P.D. Wilcox, M. Castaings, R.S.C. Monkhouse, P. Cawley, and M.J.S. Lowe. The use of huygens'principle to model the acoustic field from interdigital lamb wave transducers. In D.O. Thompson and D.E. Chimenti, editors, *Annual review of progress in quantitative NDE*, volume 17A, pages 915–922. Plenum Press, New York, 1998.

[80] J. Wolf, T. Ngoc, R. Kille, and W. Mayer. Investigation of lamb waves having a negative group velocity. *Journal of the Acoustical Society of America*, 83:122–126, 1988.

[81] D. Worlton. Experimental confirmation of lamb waves at megacycle frequencies. *Journal of Applied Physics*, 32:967–971, 1961.

[82] J. Wu and Z. Zhu. The propagation of lamb waves in a plate bordered with layers of a liquid. *Journal of the Acoustical Society of America*, 91:861–867, 1992.

Guided plate waves: temporal and spatial approach

Symmetric and antisymmetric Lamb modes propagating within a solid layer either embedded in an infinite medium or immersed in a fluid are presented. Alternative theoretical analyses of such modes are performed, first in terms of the usual approach of harmonic heterogeneous plane waves (ω,$^*S$) and then in terms of transient homogeneous plane waves ($^*\omega$,S). A large difference between dispersion curves for these two kinds of waves is shown. The minima and the zeroes of the plane wave reflection coefficients are calculated and are compared with the dispersion curves. It is found that they do not match with the dispersion curves for complex slowness, but they do agree quite well with the dispersion curves for complex frequency. In order to confirm those results, the response of a plate to a spatially and temporally bounded beam is studied at different positions along the receiver plane. Placed in the specular reflected field, zeroes in the reflected field correspond to solutions calculated in complex frequency and real slowness. Far away from the source the modal properties of the plate are no longer described by zeroes but by maxima and they are still in accordance with the two sets of dispersion curves (very low spatial or temporal attenuation). On the other hand, the energy velocity of guided waves in flat plates has been calculated from the Poynting vector functions. In the case of the lossless Lamb modes in a vacuum-bounded non-absorbing plate, the energy velocity integral has been shown analytically to equate to the group velocity. In the cases of a non-absorbing plate immersed in water and of an absorbing plate in vacuum it has been shown numerically that the energy velocity can differ substantially from the group velocity, especially at locations on the dispersion curves where the attenuation is high. An experimental study of the S_3 mode in an absorbing plate has demonstrated good agreement of the velocity of a wave packet with the predicted energy velocity at such locations where there is divergence from the group velocity.

Keywords: heterogeneous plane waves; complex frequency; bounded beam; reflection coefficient; Lamb wave energy velocity; interdigital transducers.

Ondes de plaques guidées : approche temporelle et spatiale

Les modes de Lamb symétriques et antisymétriques se propageant dans un solide pris en sandwich dans un milieu infini ou immergé dans un fluide sont étudiés. Deux analyses théoriques sont alternativement effectuées, tout d'abord en terme d'ondes planes harmoniques hétérogènes (ω,$^*S$) puis en terme d'ondes planes homogènes transitoires ($^*\omega$,S). Une grande différence entre les courbes de dispersion pour ces deux types d'ondes est observée. Les minima et les zéros des coefficients de réflexion en ondes planes sont ensuite calculés et comparés aux courbes de dispersion. Alors qu'ils ne correspondent pas aux courbes de dispersion calculées en lenteur complexe, ils semblent correspondre assez bien à celles calculées en fréquence complexe. Afin de confirmer ces résultats, la réponse d'une plaque soumise à un faisceau borné en temps et en espace est étudiée différentes positions le long du plan du récepteur. Dans la partie spéculaire du champ réfléchi, les zéros du coefficient de réflexion correspondent aux solutions en fréquence complexe et lenteur réelle. Loin de la source, les propriétés des modes de plaques ne sont plus décrites par des zéros mais par des maxima qui correspondent aux deux types de courbes de dispersion (atténuation spatiale ou temporelle très faible). D'un autre côté, la vitesse de l'énergie des ondes guidées est calculée à partir de la notion du vecteur de Poynting. Dans le cas de modes de Lamb non atténués dans une plaque non absorbante dans le vide, la formulation intégrale de la vitesse de l'énergie est analytiquement égale à la vitesse de groupe. Dans le cas d'une plaque non absorbante immergée dans un fluide ou d'une plaque absorbante dans le vide, nous montrons numériquement que la vitesse de l'énergie peut être substantiellement différente de la vitesse de groupe, spécialement à des endroits où l'atténuation est élevée. Une étude expérimentale du mode S_3 dans une plaque absorbante démontre une bonne corrélation entre la vitesse du paquet d'ondes et la vitesse de l'énergie à des endroits où il y avait divergence avec la vitesse de groupe.

Mots clés : ondes planes hétérogènes; fréquence complexe; faisceau borné; coefficient de réflexion; vitesse de l'énergie des ondes de Lamb; traducteurs interdigitaux.